Surface and Interface Sciences of Li-ion Batteries

-Research Progress in Electrode–Electrolyte Interface-

Taketoshi Minato[a,*] and Takeshi Abe[b]

[a]*Office of Society-Academia Collaboration for Innovation, Kyoto University, Katsura, Nishikyo, Kyoto 615-8510, Japan*

[b]*Graduate School of Global Environmental Studies, Kyoto University, Katsura, Nishikyo, Kyoto 615-8510, Japan*

*Corresponding author: Taketoshi Minato

Email: minato.taketoshi.5x@kyoto-u.ac.jp

Abstract

The application potential of Li-ion batteries is growing as demand increases in different fields at various stages in energy systems, in addition to their conventional role as power sources for portable devices. In particular, applications in electric vehicles and renewable energy storage are increasing for Li-ion batteries. For these applications, improvements in battery performance are necessary. The Li-ion battery produces and stores electric power from the electrochemical redox reactions between the electrode materials. The interface between the electrodes and electrolyte strongly affects the battery performance because the charge transfer causing the electrode redox reaction begins at this interface. Understanding of the surface structure, electronic structure, and chemical reactions at the electrode–electrolyte interface is necessary to improve battery performance. However, the interface is located between the electrode and electrolyte materials, hindering the experimental analysis of the interface; thus, the physical properties and chemical processes have remained poorly understood until recently. Investigations of the physical properties and chemical processes at the interface have been performed using advanced surface science techniques. In this review, current knowledge and future research prospects regarding the electrode–electrolyte interface are described for the further development of Li-ion batteries.

Keywords

Lithium -ion battery, Surface Structure, Electronic Structure, Electrode-Electrolyte Interface

Abbreviations

ABF	Annular Bright Field
AFM	Atomic Force Microscopy
AM	Amplitude Modulation
EC	Ethylene Carbonate
CVD	Chemical Vapor Deposition
DEC	Diethyl Carbonate
DFT-MD	Density Functional Theory-Molecular Dynamics
DMC	Dimethyl Carbonate
DME	Dimethoxyethane
DMSO	Dimethyl Sulfoxide
DOS	Density of States
DR-XAS	Depth Resolved X-ray Absorption Spectroscopy
EDX	Energy Dispersive X-ray
EELS	Electron Energy Loss Spectroscopy
EIS	Electrochemical Impedance Spectroscopy
EMC	Ethyl Methyl Carbonate

ESD	Electrostatic Spray Deposition
FEC	Fluoroethylene Carbonate
FM	Frequency Modulation
GC	Gas Chromatography
HAADF	High-Angle Annular Dark-Field
HAX-PES	Hard X-ray Photoelectron Spectroscopy
HOPG	Highly Oriented Pyrolytic Graphite
HREELS	High Resolution Electron Energy Loss Spectroscopy
IR	Infrared
LEED	Low Energy Electron Diffraction
LLT	$La_{0.55}L_{i0.35}TiO_3$
MD	Molecular Dynamics
MS	Mass Spectroscopy
NR	Neutron Reflectivity
PE	Polyethylene
PEO	Polyethylene Oxide
PES	Photoelectron Spectroscopy
PLD	Pulsed Laser Deposition

PM-FTIR	Polarization-modulation Fourier-transform infrared
PP	Polypropylene
PVdF	Polyvinylidene Difluoride
RF	Radio Frequency
SEI	Solid Electrolyte Interphase
SEIRA	Surface Enhanced Infrared Absorption
SEM	Scanning Electron Microscopy
SERS	Surface Enhanced Raman Scattering
SFG	Sum Frequency Generation
SOC	State of Charge
SLD	Scattering Length Density
STEM	Scanning Transmission Electron Microscopy
STM	Scanning Tunneling Microscopy
STO	$SrTiO_3$
STS	Scanning Tunneling Spectroscopy
TEM	Transmission Electron Microscopy
TERS	Tip Enhanced Raman Scattering
TRF-XAS	Total-reflection Fluorescence X-ray Absorption Spectroscopy

UHV	Ultra High Vacuum
VC	Vinylene carbonate
WKB	Wentzel-Kramers-Brillouin
XPS	X-ray Photoelectron Spectroscopy
XRD	X-ray Diffraction
XRR	X-ray Reflectivity

1. Introduction

Concerns regarding environmental pollution and the depletion of energy sources in our life are increasing. The most realistic and feasible strategy to solve these problems is the enhancement of the efficiency of energy use. Energy usage at a specific time and place by generating electricity using a rechargeable battery is one suitable method for improving efficiency. Currently, Li-ion batteries are the most common type of rechargeable batteries, with widespread use in portable electronic devices. Recently, the application of Li-ion batteries has expanded to electric vehicles, factories, and renewable energy storage [1-4]. To meet the demands of these new applications, Li-ion batteries require improvements in capacity, cycling, and high-rate performance. To improve battery performance, the interface between the electrodes and electrolyte must be both thoroughly understood and controllable. In this review, current knowledge and future research prospects regarding the electrode–electrolyte interface in Li-ion batteries are summarized.

The first Pb–acid rechargeable battery was invented in 1859 by Gaston Plante; the development of nickel–cadmium and nickel–hydrogen batteries followed, and finally led to rechargeable batteries using Li [1-4]. The high specific capacity (3860 A·h/g) of Li suggested its use as an electrode material; Li–TiS_2 and Li–MoS_2 batteries are examples of Li-ion battery systems. However, the low recharging performances and safety issues of Li negative electrodes induced the replacement of Li-negative electrodes with intercalated materials. In lithiated carbon (typically

graphite), the charge–discharge reaction in an appropriate organic electrolyte forms a stable surface film known as the solid electrolyte interphase (SEI) on the electrode [5]. The applicability of $LiCoO_2$ in positive electrode material was discovered by Goodenough *et al*. in 1980 [6]. Current Li-ion batteries use graphite negative electrodes and lithiated-metal layered compounds, typically $LiCoO_2$, as positive electrodes, in which the Li insertion and extraction processes occur during the charge and discharge reactions, respectively. In 1991, Li-ion batteries were commercialized by SONY for use in small electric devices because they offered high energy densities [7]. At present, Li-ion batteries are indispensable power sources for portable electronic devices in modern life [1-4, 9].

Modern industrial Li-ion batteries are typically composed of the following components (Fig. 1):

A. A current collector for the negative electrode

B. A composite negative electrode

C. A separator to prevent direct contact between the negative and positive electrodes immersed in an organic electrolyte

D. A composite positive electrode

E. A current collector for the positive electrode

Typically, Cu is used for A. B is prepared by mixing the active material with a binder. Carbon materials and F-containing resins like polyvinylidene difluoride (PVdF) are typically used as the

active and binder materials, respectively. When active materials with low electron conductivity are used, the conductive material, i.e. acetylene black is mixed with the composite electrode. For C, polyethylene (PE) or polypropylene (PP) microporous membranes are used as separators. The separator is immersed by the electrolyte, typically a Li salt such as $LiPF_6$, is dissolved in a carbonate-based organic solvent, often a mixture of ethylene carbonate (EC) and dimethyl carbonate (DMC), diethyl carbonate (DEC), or ethyl methyl carbonate (EMC). Small amounts of additives such as vinylene carbonate (VC) are also dissolved in the electrolyte to improve the battery performance. For D, a mixture of the active material, binder, and conductive materials is prepared (Fig. 2) [8]. Layered metal oxides like $LiCoO_2$ and PVdF are typical active and binder materials, respectively. To improve the electron conductivity, carbon materials like acetylene black are used as the conductive material. For E, Al foil is typically used, with the composite positive electrode pasted onto the metallic current collector. During the charge–discharge reaction in a Li-ion battery, Li ions and electrons move by diffusion between the active materials in the negative and positive electrodes.

During the charging and discharging of a Li-ion battery, Li ions move between the positive and negative electrodes. Here, it is assumed that Li ions initially occupy the positive electrode (Fig. 3). To begin the discharging reaction, a lower electrochemical potential is applied to the positive electrode. To compensate for the difference in electrochemical potential between the positive and negative electrodes, an electric double layer forms at the electrolyte side of the electrode–electrolyte

interface. In this electric double layer, charge transfer and the solvation of Li ions occurs [10-11]. At the interface of the negative electrode, desolvation proceeds, while a space charge layer forms at the electrode side that distorts the crystal and local structures of the electrode [1-4, 12, 13]. In addition, the electrolyte often decomposes to form an interface layer [1-5, 10, 11, 14]. These physical properties and chemical reactions at the interface strongly influence the performance; i.e., the capacity, cyclic properties, and high-rate behaviors, of Li-ion batteries. However, the interface is buried within the electrode and electrolyte, which hinders its analysis. Electrochemical studies have provided important information regarding the interface, but much remains unknown.

In this review, the current understanding of the surface structures and electronic structures for typical electrode materials is summarized because these properties are the most fundamental in affecting the interfacial phenomena. In addition, the chemical reactions occurring at the electrode–electrolyte interface are described. These are useful in further understanding of the interface and in improving the performance of Li-ion batteries.

2. Preparation and growth of samples for experimental studies surface and interface study

Composite electrodes are used in industrial Li-ion batteries; these have complex structures because of their components (Fig. 2). The extraction of surface and interface properties from the active materials within such composite electrodes is difficult. In order to study the surface and

interface properties, model electrodes can be useful. In this section, several methods used to prepare model electrodes and investigate surface and interface phenomena are described.

2.1. Thin films

The most popular method used to investigate interface phenomena in Li-ion batteries is the use of thin-film samples of the active materials. Thermal vapor deposition, radio-frequency (RF) sputtering, RF magnetron sputtering, chemical vapor deposition (CVD), electrostatic spray deposition (ESD), sol-gel methods, and pulsed laser deposition (PLD) can be used to prepare thin-film samples [14, 15]. RF sputtering and RF magnetron sputtering are the most convenient ways to prepare thin films; however, obtaining flat samples using these methods is difficult, as they produce thin films of polycrystalline particles. Among the above preparation methods, PLD is the most precise technique for preparing thin-film samples; epitaxial $LiCoO_2$(104)/ $SrRuO_3$(100)/Nb–$SrTiO_3$(100) is shown as an example in Fig. 4 [16]. PLD can induce epitaxial film growth on a crystalline substrate, meaning that this technique can prepare sufficiently high-quality samples [15-17]. However, determining the conditions necessary to prepare high-quality, highly crystalline, and flat thin films of the required composition is difficult, and doing so for compounds containing several elements is especially difficult. In addition, because the technique is so refined, obtaining thicker films requires long processing times.

2.2. Single crystals

The most ideal form in which to study the interface or surface properties of an electrode material is the bulk (millimeter-sized) single crystal. Single crystals are traditionally used in surface science work; they offer the best opportunities to precisely characterize details of the materials [18, 19]. However, the preparation of single-crystal electrode materials is difficult. For the typical active materials of Li-ion batteries, only highly oriented pyrolytic graphite (HOPG) [20], Li_xCoO_2 (Fig. 5) [21], and Li_xFePO_4 [22, 23] have been prepared as bulk single crystals for studying their interface and surface properties. Small-size (micrometer-scale) single crystals have been reported for $LiMn_2O_4$ and Li_2MnO_3 [24-27], but a detailed study requires further developments in preparing millimeter-scale single crystals. Single-crystalline $Li_4Ti_5O_{12}$ was successfully prepared by inserting Li into single-crystalline TiO_2 by calcining TiO_2 with a Li compound [28].

2.3. Others

Experiments using composite electrodes can also be used to study interface phenomena. By using scanning electron microscopy (SEM) or transmission electron microscopy (TEM), the interface can be directly observed, even with composite electrodes. As described above, composite electrodes are used in industrial Li-ion batteries; thus, the results are easily adapted for industrial

batteries.

3. Analytical methods

3.1. Surface and interface structure

To study the surface structure of an electrode, surface X-ray diffraction can be used [29]. In this method, high-flux X-rays irradiate the sample surface at an incident angle of less than the critical angle for the total reflection. The penetration depth of the X-ray is limited to several nanometers [30]. The diffraction therefore reflects the crystalline structure in the surface region of the several nanometers of the material. This method can be also used for the interface with the electrolyte.

Reflectivity measurements of X-rays and neutrons can be used to study the composition, roughness, and thickness of components at interfaces [31-36]. These measurements are performed by measuring the intensity of an X-ray or neutron beam reflection from the sample surface or interface after irradiation at a very small incident angle. Both X-ray reflectivity (XRR) and neutron reflectivity (NR) measurements can be used to analyze the composition, roughness, and thickness of a sample. XRR has advantageous signal intensity relative to NR, which is important for the detailed analysis of the reflectivity pattern. However, NR is highly sensitive to light elements, and the electrolytes of Li-ion batteries generally comprise the light elements of C, O, H, P, and F. Therefore,

NR has advantages in analyzing Li-ion battery systems. Because most materials have refractive indices $n < 1$, a neutron ray incident at an angle below the critical angle upon a flat sample experiences total optical reflection at the surface. The reflectivity intensity decreases in proportion to $\mathbf{q}^{-4}$, where $\mathbf{q}$ is the scattering vector. For an incident angle exceeding the critical angle, the incident neutron beam is divided into reflected and transmitted beams. The transmitted beam also divides into reflected and transmitted beams at each interface (Fig. 6). The waves from each reflected neutron beam are added and their relative phases cause interference oscillations, or Kiessig fringes. These oscillations reflect the scattering lengths and thicknesses of the material. The reflectivity of the neutron $R(\mathbf{q})$ is expressed by the following equation:

$$R(\mathbf{q}) = R_F(\mathbf{q}) \exp(-\mathbf{q}^2\sigma^2) \quad (1)$$

where $R_F(\mathbf{q})$ and σ are the Frenckel reflection at a perfectly flat interface and the standard deviation of the composition distribution at the interface. Thus, the neutron reflectivity reflects the composition, thickness, and roughness of the interfaces.

Microscopic techniques can directly show surface and interface structures at the molecular or atomic level. TEM and electron diffraction are widely used to analyze surface and interface structures [23, 37]. With the recent development of scanning transmission electron microscopy (STEM) based on spherical aberration correction techniques, the positions, elements, and local electronic structures of each atomic column can be analyzed [38]. Although the concept of spherical

aberration correction was proposed long ago, electron lenses using spherical aberration correction techniques were first achieved in Germany in the 1990s [39]. The resolution of TEM imaging continued to improve with the refinement of spherical aberration correction techniques [40]. Today, resolutions of < 0.05 nm can be achieved [41]. The direct observation of transition metals in active electrode materials by high-angle annular dark-field scanning transmission electron microscopy (HAADF-STEM) and the analysis of local electronic structures by STEM-electron energy loss spectroscopy (EELS) have been reported [42]. In addition, the observation of light elements such as Li, O, and H can be achieved by annular bright-field (ABF) STEM [43, 44]. TEM can be used to observe the surface structures of electrodes in cross-sectional imaging.

Scanning probe microscopic techniques are often used for direct observations of surface and interface structures. The first scanning probe microscopy technique, scanning tunneling microscopy (STM), was developed by Binning and Rorher [45, 46]. The STM experimental system firstly reported by Binning *et al*. [45] is shown in Fig. 7. In STM, a bias voltage is applied between a sharp metallic probe tip and the conductive sample. By moving the tip toward the sample surface, a tunneling current is detected before contact is established. The tunneling current I is very sensitive to the tip–sample distance s. While maintaining a constant tunneling current I, the tip scans the sample surface. The trajectory of the tip during the scan reflects the surface structure and electronic structure with atomic resolution.

Here, the theoretical background of the dependence of the sensitivity of the tunneling current *I* on the tip–sample distance s is explained [46, 47]. With the assumption of no-inelasticity, the tunneling current *I* is expressed as:

$$\mathrm{I} \propto \int_0^{eV} \rho_s(E)\rho_t(-eV+E)T(E,eV)dE \quad \text{---(2)}$$

where *e*, *V*, $\rho_s(E)$, $\rho_t(E)$, and $T(E, eV)$ are the electron charge, applied bias voltage, the densities of states (DOS) at the surface of the sample and at the probe tip at the energy *E*, and the tunneling probability of an electron of energy *E* to another site, respectively (Fig. 8). Using the Wentzel–Kramers–Brillouin (WKB) approximation, $T(E, eV)$ is expressed by

$$T(E,eV) = \exp\left(-\frac{4\pi s\sqrt{2m}}{h}\sqrt{(\Phi(z)+\frac{eV}{2}-E)}\right) \quad \text{---(3)}$$

where *s*, *m*, *h*, and $\Phi(z)$ are the tip–sample distance, electron mass, Planck constant, and the work function at position *z*. From equations (2) and (3), with the approximation of (A) a flat tip–sample potential Φ and (B) constant values for $\rho_s(E)$ and $\rho_t(E)$, the tunneling current *I* is expressed by

$$\mathrm{I} \cong \mathrm{f(V)}\exp\left(-2\mathrm{s}\sqrt{\frac{4m\pi}{h}(\Phi-\frac{e|V|}{2})}\right) \qquad (4)$$

where $f(x)$ is a function that is almost constant with changes in *V*. Equation (4) indicates that the tunneling current *I* changes exponentially with the tip–sample distance *s*, providing the high resolution of STM imaging. STM can be operated in vacuum, ambient atmospheres, and liquids [47, 48]. In addition, spectroscopic measurements based on STM can be used to study the electronic [47-52], vibrational [53-55], and spin structures [56-58], as well as the chemical reaction dynamics, of

single molecules [59-65].

Based on the principles of operation, STM is applicable only to conductive samples. Atomic force microscopy (AFM) uses a cantilever probe similar to that in STM; however, AFM can be used to image insulators. In STM, the tunneling current is used to monitor the tip–sample distance. In AFM, the forces generated between the cantilever tip and the sample are used to control the tip–sample distance. These forces F_{ts} include both long- and short-range contributions. In the long range (typically exceeding 10 nm), the van der Waals, electrostatic, and magnetic forces have large contributions in vacuum, while electric double-layer forces have large contributions on the long-range interactions in liquids [66]. In the short range (typically less than 1 nm), chemical forces and Pauli repulsive forces are typically prevalent in vacuum. In liquid, solvation forces would have large contributions in the short range as well as van der Walls, electrostatic and magnetic forces. Other forces (such as chemical and Pauli repulsive forces) would also have contributions in the short range. For high-resolution imaging by AFM, the short-range forces are exploited.

Early AFM operation was performed in a static mode, in which the tip maintained contact with the sample surface under a constant force. This method was simple, but damage to the sample surface was unavoidable. Later, dynamic modes in which the cantilever oscillation was developed to solve the problem of surface damage. In the dynamic-mode AFM, the mode can be controlled by amplitude modulation (AM) or frequency modulation (FM); the amplitude and frequency are both

affected by the forces between the tip and sample. In AM mode, the amplitude of the cantilever oscillation is used as the feedback signal and is maintained at a constant value. The tip periodically makes contact with the sample surface; however, the force of the contact is much smaller than that in the static mode. In 1991, Albrechit *et al*. reported an application of the FM mode that improved the time scale of the change in frequency of the cantilever [67]. The application of FM mode AFM dramatically improved the imaging resolution to the atomic level [68]. AFM operation in FM-mode (FM-AFM) can be performed in vacuum, but was not used in liquids because of the extreme reduction of the *Q* factor of oscillation by hydrodynamic interactions with the cantilever. Yamada *et al*. developed a system using small amplitude and large noise reduction in the cantilever deflection sensor that permitted FM-AFM operation in liquids (Fig. 9) [69-71]. True atomic resolution in liquid was first achieved in imaging muscovite mica in water [69]. FM-AFM in liquid has the unique ability of imaging the density distribution of molecules in the liquid phase around solid–liquid interfaces by detecting frequency shifts as the probe moves relative to the interface [71].

3.2. Electronic structure

To study the electronic structure of solid surfaces, photoelectron spectroscopy (PES) is widely used in surface science as well as in battery research [72-74]. In Li-ion batteries, interface layers are often formed during the charge and discharge reaction processes on the electrodes by the

decomposition of the electrolyte. The interface layer is generally thick, typically measuring more than several tens of nanometers in scale [14, 74, 75], thus blocking the escape of photoelectrons from the electrode materials and impeding analysis of the interface electronic structure beneath the surface. To overcome this problem, hard X-ray photoelectron spectroscopy (HAX-PES) using synchrotron X-rays is used to analyze electronic structures beneath interface layers. By using high-energy X-rays, the escape depth of the photoelectrons is increased. For example, the escape depth of a photoelectron of 1.5 keV is estimated to be ~3 nm for carbon materials; however, this is increased to ~50 nm for a photoelectrons of 8.0 keV. The use of HAX-PES is spreading for battery systems [72, 74]. In addition, ambient-PES could potentially be used to study the electronic structure at the interface [76-78]. However, no work has yet reported such an analysis for a battery system.

In addition to PES, total-reflectancion fluorescence X-ray absorption spectroscopy (TRF-XAS) (Fig. 10) is used to study the electronic structure of surfaces of electrodes [13, 79-82]. With the X-ray introduced at the angle of total reflectance, the fluorescence is limited to that from the surface region of the top several nanometers of the electrode [79]. By applying this technique, an electronic structure of the electrode can be analyzed during the charging and discharging processes.

STM and scanning tunneling spectroscopy (STS) can also be used to directly show the atomic-scale surface electronic structures of electrodes. From equation (3) with the approximation of the flat potential Φ between the tip and sample, the differential of equation (2) with respect to the potential

is expressed as:

$$\frac{dI}{dV} = e\rho_s(E)\rho_t(0)\exp\left(-\frac{4\pi s\sqrt{2m}}{h}\sqrt{(\Phi + \frac{eV}{2} - E)}\right) s \qquad \text{--- (5)}$$

If the applied bias V is sufficiently low, equation (6) changes to

$$\frac{dI}{dV} = e\rho_s(E)\rho_t(0)\exp\left(-\frac{4\pi s\sqrt{2m}}{h}\sqrt{\Phi}\right) s \text{ --- (6)}$$

The derived equation (6) shows that *dI/dV* reflects $\rho_s(E)$. Thus, the DOS at the surface can be determined by measuring *dI/dV*.

3.3. Vibrational structure

To analyze the reaction mechanisms occurring at the surface and interface, vibrational techniques are useful. Infrared (IR), Raman, and sum frequency generation (SFG) spectroscopy have been reported for use in analyzing electrode interfaces in Li-ion batteries. IR and Raman spectroscopy are complementary methods. *In situ* polarization-modulation Fourier-transform IR (PM-FTIR) [83], surface-enhanced IR absorption (SEIRA) [84, 85], surface-enhanced Raman scattering (SERS) [86, 87], and tip-enhanced Raman scattering (TERS) [88] are advanced IR and Raman spectroscopic techniques used to investigate interfacial phenomena. While these techniques are useful, few reports on their use with battery systems have been published. SFG spectroscopy (Fig. 11) is an interface-selective vibrational spectroscopy method, ideal for investigating interface reactions [89-91].

3.4. Theoretical methods

In addition to experiments, theoretical methods can be used to investigate the surface and interface properties of Li-ion battery materials. Much of the interfacial character remains unknown through experimental analysis because of technical problems in existing measurement systems. First principles calculations are widely used to investigate the surface, electronic, vibrational, and spin structures at the surfaces and interfaces of battery materials. The combination of experimental results and first principles calculations can permit the deep interpretation of the experimental results [92, 93]. With knowledge from first principles calculations and predictions, classical molecular dynamics (MD) calculations can be used to understand the atomic natures of interface reactions in large-scale systems. In MD calculations, constructions of precise interatomic potentials should be used; however, such construction in complex systems is generally very difficult. Recently, density functional theory–molecular dynamics (DFT-MD) calculations have been applied to investigate the interface reactions in Li-ion batteries [94].

3.5. Other analytical methods

While publications have not yet been reported, other traditional surface science techniques could be used to analyze the interfaces in rechargeable batteries. Low-energy electron diffraction

(LEED) [95] could be used to analyze the surface structure, while high-resolution electron energy loss spectroscopy (HREELS) [96] could be used to study vibrational structures. However, these methods are disadvantageous in using electron beams. The electrode materials in rechargeable batteries have often low electronic conductivity and become negatively charged under electron beam irradiation. Thus, the application of these techniques is generally difficult. Measurements using ionic [97] and He [98] scattering could also provide useful information regarding the surface structures of battery systems.

4. Surface structures of electrode materials

Understanding the surface structures of electrode materials is necessary to understand the interfacial phenomena. Here, current knowledge regarding the surface structures of some electrode materials for Li-ion battery is described. $LiCoO_2$, $LiFePO_4$, $LiMn_2O_4$, carbon, $Li_4Ti_5O_{12}$, and $LiTi_2O_4$ are selected because they are common in Li-ion batteries and investigations of their surface and electronic structures are reported.

4.1. Positive electrode materials

4.1.1. Li_xCoO_2

$LiCoO_2$ [6] is one of the most widely used materials for positive electrode in Li-ion batteries.

The crystal structure of $LiCoO_2$ is layered rock salt in the $R\bar{3}m$ space group (Fig.12). The surface structure of $LiCoO_2$ has been theoretically predicted by first-principles calculations by several groups. Kramar *et al*. investigated multiple low-index surfaces of $LiCoO_2$ [99]. The (001) and (104) (= (0001) and $(10\bar{1}4)$, respectively, in the Miller–Bravais indices used in Fig. 13) surfaces were stable within a wide range of O chemical potentials, with relative surface stabilities depending on the atmosphere. In oxidizing atmospheres, the prevalence of (001) surfaces was higher than that of (104), while in reducing atmospheres it was opposite.

$LiCoO_2$ surfaces were experimentally prepared by PLD techniques [13, 16, 79]; however, their atomic structures was not investigated. A clean Li_xCoO_2 (001) surface can be prepared by the cleavage of a single crystal of Li_xCoO_2; by this procedure the surface structures are clearly observable by STM [21]. After cleavage, a clear hexagonal structure was observed at the sample voltage bias (V_s) of −1.0 V (Fig. 14) due to Li ions on the Li_xCoO_2(001) surface. As the tip approached the sample surface, noisier images were obtained, as shown in Fig. 15. The noise arose from the high mobility of Li ions on the surface. After removing the Li ions from the (001) surface, the CoO_2 layer in Li_xCoO_2 was observed with high resolution (Fig. 16). From the comparison with the surface DOS calculated by first principles calculations, it was concluded that the protrusions in the STM images obtained under positive sample bias were caused by O ions near the Co^{4+}, produced by the removal of Li ions. No significant reconstructions were observed on this surface.

$LiCoO_2$(104) is one of the most attractive surfaces for structure studies because the (104) surface is nearly parallel to the direction of Li diffusion in bulk $LiCoO_2$ [99]. $LiCoO_2$(104) can be prepared by the epitaxial growth of thin films on $SrTiO_3$ (STO) substrates [16, 31]. However, atomically flat surfaces cannot be obtained through this method. Thus, the atomic nature of the $LiCoO_2$(104) surface structure is incompletely understood. Theoretical analysis of the (104) surface structure is also incomplete; future work remains necessary to determine the precise surface structure of this material.

4.1.2. $LiFePO_4$

Olivine-type $LiFePO_4$ belongs to the orthorhombic space group *Pnma* (Fig. 17) and shows better cyclic performance relative to $LiCoO_2$ as a positive electrode in Li-ion batteries [100]. In addition, the price of Fe is relatively low among the metals used in Li-ion battery electrode materials. In early research, the surface structure of $LiFePO_4$ was mainly investigated by theoretical calculations [101, 102]. The (010) surface of $LiFePO_4$ is of particular interest because the vector normal to the surface shows high Li-ion conductivity [103-105]. Wang and Fischer *et al*. revealed that the $LiFePO_4$(010) surface was highly stable via theoretical calculations [101, 102]. Wang *et al*. used first-principles calculations to study the surface energy and structure, while Fisher *et al*. used a classical force field (or empirical potential model) to describe the interatomic forces active in much

larger systems. In the second model, each of the ions was assigned a formal charge that remained fixed throughout the relaxation process; in reality, the electronic structure near a surface is altered or relaxed slightly, causing slight differences in the net effective charges on surface atoms relative to those in the crystal bulk. This means that the surface relaxation forces calculated by Fisher *et al*. tended to be stronger than those calculated by Wang *et al*. This effect is the most noticeable for the higher-energy surfaces where greater structural relaxation occurs because they are lower in stability. Although the two calculations used different approaches, the predictions of $LiFePO_4$(010) as the most stable surface structure were almost identical. The termination of the bulk structure at the position of Li ions achieves the most stability (Fig. 18). With this termination, the coordination numbers of Li–O and Fe–O are decreased, the bond distances of Li–O and Fe–O decrease slightly, and the surface shows Li vacancies. The calculated structure of $LiFePO_4$(010) reported by Fisher *et al*. is shown in Fig. 19.

Recently, the structure of $LiFePO_4$(010) was experimentally observed using cross-sectional TEM by Kobayashi *et al* [23]. They reported the surface reconstructions after the cleavage of this surface (Fig.20). The observed structure well matched with the structure predicted by the first principles calculations. It also clarified the changes in the surface structure induced by Li extraction from the surface.

Other surfaces of $LiFePO_4$, (100), (101), (201), and (301) were also determined to be stable by

first-principles calculations [101]. A calculation based on classical force fields also showed that (011), (201), and (221) surfaces are stable (Table 1) [102]. In fact, some of these surfaces have lower surface energies than (010), although Li diffusion is less efficient and the redox potential is more positive than those in (010) [101].

4.1.3. $LiMn_2O_4$

Spinel-type $LiMn_2O_4$ [106] has a cubic crystal structure in the $Fd\bar{3}m$ space group (Fig. 21) and the advantages of low cost, high voltage, and fast Li diffusion from the three-dimensional network of channels. Theoretical analyses of the surface structures have been reported [107, 108]. Benedek and Thackeray reported that Li-terminated (001) has the lowest surface energy [107]. However, an experiment showed that $LiMn_2O_4$ particles are predominantly terminated by (111) surfaces [109-114]. Karim *et al*. applied antiferromagnetic ordering along the [110] directions and found that $LiMn_2O_4$(111) with the inverse spinel structure was the most stable surface (Fig. 22) [108].

By using first principles calculations and a grand canonical thermodynamic formalism, Warburton *et al*. investigated the stability of the surface structures to compare the non-stoichiometric surfaces with previously reported stoichiometric surface terminations in variously oxidative and reductive environments [115]. Fig. 23 shows the surface energy of each surface for several chemical potentials of Li ($\Delta\mu_{Li}$) and O ($\Delta\mu_O$) [115]. In general, (111) is the most stable for a wide range of $\Delta\mu_{Li}$

and $\Delta\mu_O$ values. This is consistent with the results previously reported by Karim. However, the observed surface structure was not inverse spinel; they suggested that the Li-terminated structure (Fig. 24) was the most stable. This structure reduced the dipole moment of the Mn_xO_{4x} layers with an additional Li layer at the interface. Experimentally, the stability of $LiMn_2O_4(111)$ against dissolution, which causes the capacity to decrease, has been observed [116].

4.2. Negative electrode materials

4.2.1. Carbon

Carbon materials are currently the most popular materials for negative electrodes in Li-ion batteries. Both graphitic and non-graphitic carbon materials are used in Li-ion batteries. In this review, only graphitic carbon is discussed because its crystalline nature is needed for analysis of the surface structure. The crystal structure of graphitic carbon, based on sp^2-hybridized carbon atoms forming a planar honeycomb structure known as graphene, is well known. Each graphene layer interacts with others by van der Waals forces; layered lattice structures of graphene form with the layer distance of 0.33 nm [2]. The perfect stacking of graphene layers via one of two stacking patterns produces graphite. The stacking pattern sequence of ABABAB forms hexagonal graphite, while that of ABCABC sequences forms a rhombohedral structure. In this work, we discuss research on hexagonal graphite because HOPG, a typical single-crystal graphite form, has a hexagonal

structure in the $P6_3/mmc$ space group (Fig.25).

Graphite can have two surface structures (Fig. 25). One is the basal plane (Fig. 25), observation of which can be achieved by ultra-high-vacuum (UHV)-STM or AFM [47, 48, 66]. In aqueous solutions, the honeycomb basal plane surface structure can be observed by STM or AFM and is identical to the structure observed in UHV (Fig. 26) [117]. However, in the electrolyte of Li-ion batteries, the surface structures were not be directly observed by microscopic techniques.

The other possible graphite surface is the edge plane (Fig. 25), which can be zigzag or armchair in structure (Fig. 27). These surfaces are more active for Li insertion and extraction than the basal plane [1-3]. However, defects on the edge plane such as dangling bonds, C–H, C–OH, and C–OOH can influence Li insertion and extraction [2]. Investigation of the edge plane of HOPG has been reported [118, 119], but the surface structure has not yet been atomically analyzed because of the difficulty in preparing clean and flat edge-plane graphite surfaces.

4.2.2. $Li_4Ti_5O_{12}$ and $LiTi_2O_4$

$Li_4Ti_5O_{12}$ (Fig. 28) and $LiTi_2O_4$ (Fig. 29) are two Li–Ti oxide compounds that show good performance as negative electrodes in Li-ion batteries. Both compounds have spinel crystal-based structures in the $Fd\bar{3}m$ space group, although $LiTi_2O_4$ has a relatively distorted structure. The materials, particularly $Li_4Ti_5O_{12}$, offer the advantage of stable cyclic performance because the

volumetric changes accompanying Li insertion and extraction are almost negligible [120, 121]. In addition, the materials provide constant electrode potentials and sufficient electron conductivities [120, 121]. Calculations of $Li_4Ti_5O_{12}$ surfaces have not yet been reported. Experimentally, single-crystal layers of $Li_4Ti_5O_{12}$ can be prepared by the solid-state reaction of single-crystalline TiO_2 with $LiOH{\cdot}H_2O$ powder [28]. The surface structure of $Li_4Ti_5O_{12}(111)$ can be imaged by UHV-STM (Fig. 30) [122] and by FM-AFM in aqueous solutions (Fig. 31) [123]. The $Li_4Ti_5O_{12}(111)$ surface is comprised of Li and O atoms (Fig. 32) [123], with bright spots in the STM image assigned to surface Li ions. In liquid-FM-AFM image, it is suggested that the origin of the bright spots may be influenced by water molecules [123]. The surface structure of $Li_4Ti_5O_{12}$ can also be observed by TEM [124, 125]. The change of the surface structure to a rock-salt structure by immersion into an electrolyte (1 M $LiPF_6$ in PC) [124], as well as Li insertion to the surface caused by irradiation by an electron beam [125] are observed. The structures of other surfaces of $Li_4Ti_5O_{12}$ have not been observed experimentally.

For $LiTi_2O_4$, the thermodynamic stabilities of the surface structures have been calculated by first-principles calculations [126]. The stabilities of the five terminations of (100)-Ti_2O_4, (110)-Ti_2O_4, (210)-Ti_2O_4, (111)-$LiTiO_4$, and (310)-Ti_2O_8 were reported to depend on the chemical potentials of Ti and O [126]. In recent experiments, Okada *et al.* observed the surface structure of $LiTi_2O_4(111)$ by STM after preparing thin-film $LiTi_2O_4$ on a flat STO substrate by PLD [17]. Using

first principles calcualtions, they clarified that the prepared $LiTi_2O_4$(111) surface was terminated by Ti.

5. Electronic structures of electrode materials

The electronic structures of electrode surfaces strongly influence interfacial phenomena in battery systems. The current status of investigations regarding the electronic structures of the surfaces of Li-ion battery electrode materials is described in this section.

5.1. Positive electrode materials

5.1.1. $LiCoO_2$

The electronic structures of $LiCoO_2$ surfaces have been theoretically calculated and reported by several groups. Hu *et al*. used first-principles calculations to investigate the electronic structure of $LiCoO_2$(003) [127] with both Li–O and Co–O terminations as well as the non-polar surface of $LiCoO_2$(003). The highest occupied state had mostly Co 3*d* with a small amount of O 2*p* character. In their reports, the (003) surfaces with Li–O and Co–O terminations showed metallic characteristics, despite the insulating nature of the bulk $LiCoO_2$. The contribution of Co 3*d*, Li 1*s*/2*p*, and O 2*p* and the expansion of the bandwidth of O 2*p* each cause the narrowing of the electronic bandgap, suggesting that the surface electronic structure is closely related to the surface termination.

The surface electronic structure is also strongly affected by the spin state of surface Co atoms. Qian *et al*. reported that the spin transition of Co from low to intermediate spin narrowed the bandgaps of both $LiCoO_2$(104) and (110) surfaces [128]. In addition, Huang *et al*. reported that the exchange of surface Li to H narrowed the bandgap of the $LiCoO_2$(001) surface [129]. These reports support the significant influence of small structural variations, such as defects, on the surface electronic structure.

Experimentally, the electronic structure of the $Li_{0.67}CoO_2$(001) surface prepared by the cleavage of a bulk single crystal was investigated [21]. On the Li-terminated $Li_{0.67}CoO_2$(001) surface, *n*-type semiconductive behavior was observed by STS (Fig. 33); the half-monolayer of Li ions should be present on the Li-terminated surface to satisfy the charge compensation needed to retain the Co^{3+} oxidation state. For areas with higher Li ion coverage, the excess Li ions induce the reduction of subsurface Co ions to the Co^{2+} oxidation state, causing the *n*-type semiconductive behavior of the surface.

When Li ions are removed from the surface, the CoO_2 layer can be observed by STM [21]. Two distinct areas of ordered (Fig 34) and disordered (Fig. 35) structure were observed. In the ordered area, protrusions form a 3 × 3 hexagonal lattice, attributed by first principles calculations to O ions coordinated with three Co^{3+} and Co^{4+} ions each for the occupied and unoccupied state images, respectively. Co^{4+} is formed by the removal of Li ions. STS measurements in this region reveal

metallic features (Fig. 34d), which is different from the Li-terminated surface. Meanwhile, the disordered area shows further differences; Fig. 35d shows the STS from the disordered area, clearly depicting semiconductive behavior and a clear bandgap. These observations demonstrate the effects of Li ionic ordering on the electronic structure and local electron conductivity of the electrode surface. These effects arise from the scattering of conductive electrons by the random distribution of the electronic structure. During the charging and discharging processes of a Li-ion battery, Li ions diffuse between the positive and negative electrodes; generally, high Li-ion conductivity in the electrodes promotes better battery performance. In addition, electrons are transferred between the two electrodes during the charge and discharge processes to maintain electrode charge neutrality. Thus, both electronic and ionic conductivity are required for electrodes. These clearly confirm that electrodes with ordered structures provide better battery performance than those with disordered structures.

5.1.2. $LiFePO_4$

Based on optical measurements, the bandgap of $LiFePO_4$ is estimated to be ~3.8–4.0 eV [130]; this is confirmed by first-principles calculations, indicating that $LiFePO_4$ is electronically insulating in nature [130]. A smaller bandgap of ~2.0 eV on the $LiFePO_4$(010) surface was obtained by first-principles calculations [131, 132]. However, additional first-principles analyses predicted metallic

electronic structures for $LiFePO_4$(100) and $LiFePO_4$(001) [132]. It was also reported that the oxidation of the $LiFePO_4$(010) surface (Fig. 36 and 37) or the formation of an Li_2S/oxidized $LiFePO_4$(010) interface can change the surface electronic properties from insulating to metallic in nature because of the formation of hybrid states [131]. These characteristic properties predicted theoretically have not yet been experimentally studied.

5.1.3. $LiMn_2O_4$

The electronic structure of the most stable $LiMn_2O_4$(111) surface has not been yet reported, but that of $LiMn_2O_4$(001) has been studied via calculation methods. Bulk $LiMn_2O_4$ contains Mn ions with the oxidation state of +3.5 [133]. On the Li-terminated $LiMn_2O_4$(001) surface, the decreasing of Mn coordination with O induces a decrease in the oxidation state of Mn to +3 [133]. The Mn 3*d* projected DOS in Fig. 38e shows that t_{2g} and d_{z2} (a component of e_g) are fully occupied. The electron from the ionized Li fills the $3d_{z2}$ state. This agrees with X-ray photoelectron spectroscopy (XPS) observations of Mn^{3+} in $LiMn_2O_4$ [134] and matches the features of MnO-terminated $LiMn_2O_4$(001), which are almost the same as those of (010) and (100) [133].

Using first principles calculations, Warburton *et al*. reported that the charge of Mn ions on the (001) surface is reduced from ~3+ to ~2+ with the removal of O [135]. The disproportion of Mn ions may enhance the dissolution of Mn in the electrolyte [134, 135]. The formation of Mn^{2+} is consistent

with the experimentally determined susceptibility of the (001) surface to corrosion and dissolution [136, 137].

5.2. Negative electrode materials

5.2.1. Carbon

The electronic structure of the basal plane of graphite can be experimentally observed by photoelectron and inverse photoelectron spectroscopy, as well as STS [138-141]. Fig. 39 shows the STS spectra obtained from the HOPG basal plane surface [139]. The DOS increases linearly depending on the energy. The bonding π and anti-bonding π* states cross approximately at the Fermi energy level E_F, characteristic of a zero-gap semiconductor. Between the saddle points of the bonding and anti-bonding π and π* states, an energy difference of ~4 eV is observed, matching previous theoretical results (Fig. 40) [142]. In the STS, a surface state at approximately +3.0 V is observed. The electronic structure of the basal plane of graphite is affected by surface modification. For example, it is reported that the adsorption of metal on the graphite causes the formation of a charge transfer state below E_F [143].

The electronic structures of both armchair- and zigzag-conformation graphite edge sites have been widely investigated. As shown in the STS obtained from an armchair-conformation HOPG edge sites, the electronic structure is similar to that of the HOPG basal plane (Fig. 41a) [144]. This

matches both experimental and theoretical results showing the energetic stability of the armchair-structured edge [145-157]. Meanwhile, the electronic structure of the zigzag edge is distinct, as shown by STS in Fig. 41b [144]. A clear peak spanning −100 to −20 mV is observed, arising from the non-bonding π electronic structures localized at the carbon atoms comprising the zigzag edge. This state is half-filled, forming a localized spin that contrasts with the diamagnetic properties of bulk graphite.

All these reports concern the electronic structure of the edge "sites." Still, no experimental investigations on the electronic structure of the edge "plane" of graphite have been reported owing to the difficulty in preparation.

5.2.2. $Li_4Ti_5O_{12}$ and $LiTi_2O_4$

Neither theoretical nor experimental investigations of the electronic structure of $Li_4Ti_5O_{12}$ surfaces have been reported, although the electronic structure of the interface between $Li_4Ti_5O_{12}$ and $Li_7Ti_5O_{12}$ formed during charging and discharging has been investigated by first-principles calculations [158, 159]. The insertion of Li ions into $Li_4Ti_5O_{12}$ causes two phase separations between $Li_4Ti_5O_{12}$ and $Li_7Ti_5O_{12}$ [160]. Bulk $Li_4Ti_5O_{12}$ and $Li_7Ti_5O_{12}$ are both insulators; however, the interface at the phase boundary between $Li_4Ti_5O_{12}$ and $Li_7Ti_5O_{12}$ for [111] is metallic. At this interface, one Li atom is extracted from a 16c site in $Li_7Ti_5O_{12}$, causing the DOS around E_F to ensure

the metallic nature of the interface. The electronic structures of the (100), (110), (111), (210), and (310) surfaces for different configurations of $LiTi_2O_4$ were calculated by first-principles calculations (Fig. 42) [126]. Non-zero DOS in the bandgap was observed by the contribution from Ti in many of the termination cases. Some of these states are partially occupied, and high electron conductivities are predicted at the surfaces. For $LiTi_2O_4$(111), Okada *et al.* observed that the pseudogap opening at E_F modified the surface to show superconductivity, unlike the bulk [17].

6. Chemical reactions at the interface

As described in the introduction, the chemical reactions at the electrode–electrolyte interface strongly affect the performance of the Li-ion battery. In this section, current knowledge relating to the interface layer formed by electrolyte decomposition, the formation of the space charge layer, and the desolvation processes is described.

6.1. Interface layer formation

One major topic in studying interface reactions is the formation of interface layers by electrolyte decomposition. Many experimental results have shown that the formation of the interface layer affects the battery performance [14, 75]. For graphite electrodes, the interface layer or SEI [5] has been particularly widely investigated [14]. PES, SEM, TEM, energy-dispersive X-ray (EDX)

spectroscopy, and EELS have been used to analyze the composition, thickness, and structure of the SEI, mainly based on *ex-situ* analysis performed by opening batteries at different states of charge (SOC) [14]. *Ex-situ* analysis is helpful, but the opening of the battery can affect the state of the interface layer and dynamic processes such as non-equilibrium states cannot be detected by *ex-situ* analysis. To solve these problems, *in-situ* analysis of the interface layer has been reported recently [14]. Because the interface is located between the organic electrolyte and solid electrolyte, the analysis method must be able to approach the buried interface; in addition, the interface layer is mainly composed of light elements such as C, O, and H, so the analytical method must be sensitive to light elements.

NR measurements fulfill these analytical requirements. NR measurements were performed to analyze the composition, thickness, and roughness of an $LiCoO_2$–electrolyte interface [16]. For NR analysis, a flat sample is necessary; an epitaxial film of $LiCoO_2$(104) on $SrRuO_3$(100)/Nb–$SrTiO_3$(100) was prepared (Fig. 4). Fig 43 shows the results of NR and analyzed scattering length density for the pristine, electrolyte-immersed (1 M $LiClO_4$ in deuterated EC:DMC vol. 1:2), fully charged (+4.2 V vs. Li/Li^+), and fully discharged (3.3 V vs. Li/Li^+) $LiCoO_2$(104)/$SrRuO_3$(100)/Nb-$SrTiO_3$ (100). After the immersion of $LiCoO_2$(104) in the electrolyte, an interface layer forms ((ii) in Fig. 43a and 43b). From the analysis of scattering length density (SLD), it is determined that the interface layer mainly comprises polyethylene oxide (PEO). In electrolytes using mixed EC/DMC

solvents, the accumulation of EC on $LiCoO_2$ electrodes because of the high polarization of EC has been observed [90]. At the interface of $LiCoO_2$(104) and the electrolyte, EC molecules should contact with the $LiCoO_2$(104) surface. With this contact with $LiCoO_2$(104), Co ions are reduced, as observed in polycrystalline $LiCoO_2$ [13]. PEO formation is caused by the oxidative polymerization of the EC molecules. According to previous first principles calculations [161], the EC molecular oxidation produces the unstable radical species **1** as follows:

$$[EC\text{-}ClO_4^-] - e^- \rightarrow O{=}CH\text{-}\dot{C}H_2 + CO_2 + HClO_4$$

1

Based on the reactions, the reaction of species **1** with additional EC molecules forms the radical species **2** and **3**.

$$O{=}CH\text{-}\dot{C}H_2 + EC \rightarrow CO_2 + O{=}CH\text{-}CH_2\text{-}O\text{-}\dot{C}H_2\text{-}CH_2$$

1 **2**

$$O{=}CH\text{-}CH_2\text{-}O\text{-}CH_2\text{-}\dot{C}H_2 + EC \rightarrow CO_2 + O{=}CH\text{-}CH_2\text{-}O\text{-}C_2H_4\text{-}O\text{-}CH_2\text{-}\dot{C}H_2$$

2 **3**

From the reactions, a general expression of the product of the polymerization is given as **4**.

$$O{=}CH\text{-}CH_2\text{-}[\text{-}O\text{-}CH_2\text{-}CH_2\text{-}]_n\text{-}O\text{-}CH_2\text{-}\dot{C}H_2$$

4

Product **4** mainly comprises the PEO group ([-O-CH_2CH_2-]$_n$-); thus, a PEO layer is formed at the electrolyte–$LiCoO_2$(104) interface. During charging ((iii) in Fig. 43a and 43b), the thickness of the interface layer is increased from 30.6 nm to 48.8 nm and insertion of Li into the layer is observed. These changes are caused by the additional decomposition of the electrolyte via oxidative reaction and the trapping of Li ions extracted from $LiCoO_2$(104). For the composition of the interface layer, the addition of inorganic species such as Li_2CO_3, LiCl, $LiOCO_2CD_3$, and $(LiCO_2CD_2)_2$ is suggested. In the discharge process, the thickness of the interface is decreased from 48.8 nm to 35.6 nm, although the composition remains mostly unchanged ((vi) in Fig. 43a and 43b). These changes are attributed to the simple stripping of the interface layer by the insertion and diffusion of Li in the discharge process. This suggests that interactions in the interface layer are not strong. These NR analyses clearly show the dynamic changes in the interface layer during the charge and discharge processes.

On graphite electrodes, SEI formation has been detected by FT-IR [162-171], XPS [172-175], gas chromatography (GC) [176], and TEM [177-179] and directly observed by *in-situ* AFM [20]. Fig. 44 shows the *in-situ* AFM of basal HOPG in 1 M $LiClO_4$ in EC-DMC (vol. 1:1) during potential scan between 2.9 and 0.05 V (vs. Li/Li^+). The insertion of solvated Li into the basal plane of HOPG is observed from the step below 1.0 V (vs. Li/Li^+) in EC-based electrolytes at room temperature. At ~0.95–0.80 V (vs. Li/Li^+), the terrace structure is changed (Fig. 44c) by the intercalation of the

solvated Li from the step. In addition, the formation of a blister with a height of ~15–20 nm (white circle in Fig. 44c) from the accumulation of decomposition products of the solvated Li in the graphite layers is observed (Fig. 44d). At potentials more negative than 0.65 V (vs. Li/Li^+), particle-like precipitates are observed on HOPG. From pyrolysis/GC/mass spectroscopy (MS) analysis, the precipitates contain longer polymerized compounds with repeated oxyethylene units similar to PEO. The number of the precipitates increases as the potential decreases to 0.05 V (vs. Li/Li^+), as shown in Fig. 44e, but they disappear at 2.9 V (vs. Li/Li^+) after the reverse sweep as shown in Fig. 44f, probably because of scratching by the AFM tip. The surface morphology changes and the number of precipitates observed in the second cycle of Li intercalation are very small. This is an important finding because it suggests that effective SEI exists even after the removal of the surface by the AFM tip. The SEI formation is affected by impurities in the electrolyte. The formation of pits and the interface layer triggered by the electrochemical decomposition of POF_2OH in the electrolyte are observed on the basal plane of HOPG [180, 181].

For SEI formation on the edge plane of a graphite electrode, Domi *et al*. used a polished edge plane-oriented HOPG sample to observe the surface morphology changes by *in-situ* AFM [118, 119]. The formation of fine particles smaller than 0.1 μm was observed in the range of 1.0–0.6 V (vs. Li/Li^+). These are remnants of the blisters observed on the basal plane. With further sweeping of the potential into the negative region, the formation of precipitates by electrolyte decomposition was

observed, similar to that on the basal plane. The thickness of the layer formed on the edge plane was ~55 nm, slightly thicker than that on the basal plane (~44 nm). The formation of the thicker layer was caused by the higher activity of the edge plane compared to that of the basal plane. After the second cycle, the layer thickness was estimated as 66 and 77 nm on the edge and basal planes, respectively; indicating a suppressed increase in thickness on the edge plane. This implies that the layer formed on the edge plane in the first cycle works as an effective passivation layer, and suppresses the decomposition of the electrolyte than that on the basal plane.

6.2. Space charge layer

On the electrode surfaces of a working battery, space charge layers with properties differing from those of the bulk are formed by the electric field [12]. The effects of space charge layer formation on the battery performance have been suggested by studies on Li-ion batteries using solid electrolytes [12]. The electrochemical performance of the electrode and the interfacial resistance are both affected by electrode coatings; the effects are interpreted to arise from the space charge layer. The space charge layer formation on an Li_xCoO_2 electrode in organic electrolyte was observed by TRF-XAS [13, 79-82]. On the $LiCoO_2$ surface, differences in the electronic structural behavior were observed relative to that of the bulk [13, 79]. When the electrode was in contact with the electrolyte, the reduction of Co ions on the electrode surface was observed (Fig. 45a). This reduction was caused

by the compensation of the electrochemical potential between the positive and negative electrodes. On the $LiCoO_2$ surface, the compensation of the electrochemical potential is achieved by the formation of the space charge layer because the electronic structure features a conduction band minimum at a relatively low energy [182]. The crystal structure of the $LiCoO_2$ surface is distorted by the formation of the space charge layer, causing the irreversible deterioration of the surface of the electrode during the first charging process (Fig. 46a, 46b) and the subsequent capacity fading in later charge–discharge cycling (Fig.47).

On the surface of $LiFePO_4$, another typical material for positive electrode in Li-ion batteries, different surface electronic structure features were observed [77]. The electronic structure of Fe at the surface of the $LiFePO_4$ electrode does not change upon contact with the electrolyte (Fig. 45b). In addition, during charging process, the irreversible change of the surface structure observed in $LiCoO_2$ is absent in $LiFePO_4$ (Figs. 46c, 46d). Because of the reversible surface changes, the charge and discharge capacity of $LiFePO_4$ remains stable during cycling. The observed stability of the $LiFePO_4$ surface arises from the suppression of the formation of the space charge layer. Because the conduction band minimum of $LiFePO_4$ is relatively higher in energy [128], compensation for the electrochemical potential difference between the working and counter electrodes is less easily achieved by the formation of a space charge layer on the $LiFePO_4$ surface (Fig. 47). Instead of a space charge layer, an electric double layer formed on the electrolyte side compensates for the

difference in electrochemical potential. Thus, the $LiFePO_4$ electrode shows reversible surface changes during the charge process and improved cyclic performance during charge–discharge cycling.

The effects of surface coatings on the space charge layer formed on electrodes can be analyzed by TRF–XAS and depth-resolved XAS (DR-XAS) spectroscopy [81]. MgO coatings on $LiCoO_2$ can improve the Coulombic efficiency of the charge and discharge capacity at high potentials of ~4.3–4.4 V (vs. Li/Li^+). TRF-XAS shows that the reduction of Co ions during the soaking of the electrolyte and the structural deterioration of the $LiCoO_2$ surface are suppressed by the MgO coating. This is explained by the formation of a solid solution of Mg on the $LiCoO_2$ surface (Fig. 48); the solution phase stabilizes the layered structure of $LiCoO_2$ and thus prevents structural deterioration caused by the space charge layer.

By adding VC to the electrolyte, space charge layer formation at the $LiCoO_2$ surface is suppressed [82]. Battery performance improvements by the addition of VC are well known for negative electrode reactions, particularly with carbon negative electrodes. Similar to the negative electrode coating, the VC improves the cyclic charge–discharge capacity of $LiCoO_2$. TRF-XAS analysis revealed that VC in the electrolyte suppressed the reduction of Co ions and the structural deterioration of the $LiCoO_2$ surface. These demonstrate the suppression of space charge layer formation, similar to the effects of an MgO coating on $LiCoO_2$. However, the VC additive does not

form solid solutions as the MgO coating does. A different mechanism suppresses the formation of the space charge layer. Because of the high dielectric constant of VC of 127 [14], many VC molecules are expected to accumulate at the $LiCoO_2$ surface. VC is more easily oxidized than EC, and the oxidized VC molecules initiate polymerization on the $LiCoO_2$ surface. Thus, the surface of $LiCoO_2$ becomes covered by an interface layer formed by the oxidative decomposition of VC. This layer physically separates the $LiCoO_2$ from the electrolyte, thereby suppressing further oxidation of the solvent molecules, and reduction of the Co ions. The formation of an irreversible structural change at the $LiCoO_2$ surface due to the formation of the space charge layer was not observed (Fig. 49). These improve the cyclic performance of $LiCoO_2$.

So far, analysis of the space charge layer has been performed by spectroscopic measurements. In future, the changes described above should be directly observed by microscopic techniques. The most suitable equipment to analyze the surface structure changes are STM and AFM because they can operate during the charge and discharge processes.

6.3. Desolvation process

Li ions in the electrolytes of Li-ion battery systems are coordinated with organic solvents [10, 11]. When the Li ions are transferred from the electrolyte to the electrode, the ions must release the coordinated solvent molecules via desolvation processes. Electrochemical analysis has concluded

that the desolvation process has a high energy barrier and is necessary in understanding the interfacial processes.

We begin the discussion with Li transfer between a solid and liquid electrolyte because the chemical reactions at the solid–liquid interface do not include electrolyte decomposition, a redox reaction that affects the resistance. In the experiments, the main contribution of the interfacial resistance is assigned to Li transfer between the solid and liquid electrolytes. Electrochemical impedance spectroscopy (EIS) can be used to estimate the resistance to ion transfer between the electrode and electrolyte. Fig. 50 shows an example of the Nyquist plot for a four-probe system used in the experiments consisting of Li/electrolyte/$La_{0.55}Li_{0.35}TiO_3$ (LLT)/electrolyte/Li [10]. The electrolyte is 1 M $LiCF_3SO_3$ in PC. The low-frequency semicircle is assigned to the LLT–electrolyte Li-transfer resistance. From the temperature dependence of the resistance and Arrhenius plotting, the activation barrier energy was estimated; the activation barrier clearly depended on the solvents used in the electrolyte. The activation barrier for the system using dimethyl sulfoxide (DMSO) as the solvent is 69.9 kJ/mol, higher than that using PC (57.3 kJ/mol) or fluoroethylene carbonate (FEC, 31.5 kJ/mol) (Fig. 51). First principles calculations show similar tendencies: the desorption energy of a solvent molecule from a single Li ion decreases in the order of DMSO, PC, and FEC [10]. The activation barriers for interfacial Li transfer in EC-DMC and DMC solvents were also estimated; those in DMC-only electrolytes were ~16–21 kJ/mol smaller than those in EC-DMC. As explained

previously, the interfacial resistance mainly arises from Li ion transfer in these experiments. Thus, it is shown that Li ion transfer at the interface is influenced by the desorption of solvents coordinated with Li ions.

The activation barrier to Li transfer between an $LiCoO_2$ thin-film electrode and a liquid electrolyte (1 M $LiClO_4$ in PC) was also estimated by EIS measurements to be 61.0 kJ/mol (Fig. 52) [183]. This value is similar to that obtained at the LLT/electrolyte interface in PC solvent (57.3 kJ/mol). This similarity supports the strong correlation of the interfacial resistance with the desolvation process, even at the electrode–electrolyte interface in Li-ion batteries.

The influence of the desolvation process is also observed with graphite electrodes [184]. From EIS measurements, the activation barriers to Li ion transfer in dimethoxyethane (DME) and EC-DEC electrolytes with HOPG electrodes are estimated as 25 and ~53–60 kJ/mol (Fig. 53), respectively. From X-ray diffraction (XRD) measurements of the HOPG electrode after lithiation, the Li ions in graphite in the EC- DEC-based electrolyte are desolvated; however, those in the DME-based electrolyte remain coordinated with solvent molecules in graphite. This originates from differences of the interactions between Li and the different solvents. In the EC-DMC-based electrolyte, EC molecules are coordinated with Li ions. The interaction strength of DME and Li ions is higher than that of EC and Li ions. Thus, the DME molecules cannot desorb at the interface. In the EC-DEC-based electrolyte, EC decomposes and forms an efficient SEI on the graphite electrode

because the Li ions are efficiently desorbed from EC solvent molecules at the interface.

The above results demonstrate that the desolvation process strongly affects Li ion transfer at the electrode–electrolyte interface. Desolvation (and solvation) occur in the electric double layer formed on the interface. To understand the molecular actions during the desolvation process, the electric double layer must be carefully investigated using advanced spectroscopic or microscopic analyses. Methods to observe the desolvation and solvation processes and thereby clarify the mechanism of the electronic double layer include interface-sensitive vibrational spectroscopic techniques, such as SEIRA [84, 85] and SFG [89-91]. With analysis of the coordination structures of Li ions at the interface by vibrational spectroscopy, the desolvation and solvation steps can be clarified. Recently, several studies analyzing the interface have been reported [89-91]. Microscopic techniques such as STM [185] and AFM [69, 70, 186, 187] can directly visualize the desolvation and solvation processes. We recently used FM-AFM in liquid to analyze the interface structures formed by tetraglyme, a organic solvent investigated for use in Li-ion batteries, and graphite [188]. The adsorbed tetraglyme molecules are clearly observed to form a linear superstructure with a molecular distance of ~0.65 nm on HOPG (Fig. 54). From vertical scanning, the formation of a layered structure of the exiting probability of tetraglyme at the interface with the distance of 0.60 nm is observed (Fig. 55). This demonstrated that the liquid-phase molecular distribution at the electrode–electrolyte interface can be directly visualized by FM-AFM. This technique can therefore be applied

to interfacial analysis in working batteries. Observations of electrode–electrolyte interface structures in electrochemical conditions were reported [187]; the application of these techniques to Li-ion batteries can be expected to provide new insights on the interface reactions.

7. Concluding remarks

In this review, current knowledge regarding the geometric and electronic structures at the surfaces of various electrode materials, as well as that regarding the chemical processes at the electrode–electrolyte interfaces, are summarized for Li-ion batteries. The break in crystalline periodicity at the interface strongly influences the interfacial physical properties. The stability of the surface structure of the electrode material strongly depends on the plane orientation and the atmosphere. In addition, the electronic structure is significantly influenced by the termination structure. These induce complexities in the investigation of the physical properties of the electrode surfaces in Li-ion batteries. So far, experimental investigations have been limited to the surface structures of $LiCoO_2$(001), $LiFePO_4$(010), $Li_4Ti_5O_{12}$(111), $LiTi_2O_4$(111), and the basal plane of graphite and the electronic structures of $LiCoO_2$(001), graphite (basal planes and edge sites but not on the plane), and $LiTi_2O_4$(111). Other systems have only been investigated by theoretical calculations. Obviously, more surfaces should be widely investigated, in addition to these reported

systems. The physical properties of the surfaces of electrode materials with high activity for Li insertion and extraction, such as $LiCoO_2$(104) and the edge plane of graphite, remain uncharacterized at present. As described above, this is because of the difficulty in preparing high-quality samples having atomically flat surfaces. Breakthroughs to prepare such surfaces are necessary for progress in the experimental investigation of the surface and electronic structures of these materials.

Regarding the chemical processes at the electrode–electrolyte interface, the thickness, composition, and roughness of interface layers have been analyzed by NR and AFM, allowing clarification of the dynamical changes and real SEI formation at the electrode–electrolyte interfaces. Also, the effects of space charge layers on battery performance have been investigated by TRF-XAS. It is clarified that the control of the space charge layer is important in improving battery performance. In addition, EIS analysis provided the desolvation processes have a strong influence on the interface reactions that gives new information to improve the battery performance by controlling the interface. For further improvements in battery performance, the atomic and molecular natures of the materials should be carefully studied. Much work remains regarding the electrode–electrolyte interface in Li-ion batteries that can be accomplished using surface science techniques; both advanced and traditional techniques can be applied. We believe that both surface and interfacial characterization can elucidate new aspects of the electrode–electrolyte interface in Li-ion batteries,

thus driving innovative improvements in battery performance to contribute to future energy and environmental solutions.

Acknowledgements

A part of research described in this review was supported by the Research and Development Initiative for Scientific Innovation of New Generation Batteries (RISING) and Research and Development Initiative for Scientific Innovation of New Generation Batteries 2 (RISING2) projects of the New Energy and Industrial Technology Development Organization (NEDO), Japan.

References

[1] G.-A. Nazari and G. Pistoia, Lithium Batteries, Springer (2003).

[2] M. Yoshio, R. J. Brodd, A. Kozawa, Lithium –Ion Battery, Springer (2009).

[3] K. Ozawa, Lithiun Ion Rechargeable Batteries, Wiley-VCH (2009).

[4] B. Scrosati, K. M. Abram, W. Schalkwijk and J. Hassoum, Lithium Batteries, Wiley-VCH (2013).

[5] E. Peled, The electrochemical behavior of alkali and alkaline earth metals in nonaqueous battery systems—the solid electrolyte interphase model, J. Electrochem. Soc. 126 (1979) 2047 - 2051.

[6] K. Mizushima, P. Jones, P. Wiseman, J. B. Goodenough, Li_xCoO_2 ($0 < x < 1$): A new cathode material for batteries of high energy density, Mater. Res. Bull. 15 (1980) 783 - 789.

[7] B. Diouf and R. Pode, Potential of lithium-ion batteries in renewable energy, Renew. Energy, 76 (2015) 375 - 380.

[8] D. E. Stephenson, B. C. Walker, C. B. Skelton, E. P. Gorzkowski, D. J. Rowenhorst, and D. R. Wheeler, Modeling 3D Microstructure and Ion Transport in Porous Li-Ion Battery Electrodes, J. Electrochem. Soc. 158 (2011) A781 - A789.

[9] J. M. Tarascon and M. Armand, Issues and Challenges Facing Rechargeable Lithium Batteries, Nature, 414 (2001) 359 - 367.

[10] T. Abe, F. Sagane, M. Ohtsuka, Y. Iriyama, and Z. Ogumi, Lithium-Ion Transfer at the Interface

Between Lithium-Ion Conductive Ceramic Electrolyte and Liquid Electrolyte-A Key to Enhancing the Rate Capability of Lithium-Ion Batteries, J. Electrochem. Soc. 152 (2005) A2151 – A2154.

[11] Y. Yamada, F. Sagane, Y. Iriyama, T. Abe, and Z. Ogumi, Kinetics of Lithium-Ion Transfer at the Interface between $Li_{0.35}La_{0.55}TiO_3$ and Binary Electrolytes, J. Phys. Chem. C 113 (2009) 14528 – 14532.

[12] N. Ohta, K. Takada, L. Zhang, R. Ma, M. Osada, and T. Sasaki, Enhancement of the High-Rate Capability of Solid-State Lithium Batteries by Nanoscale Interfacial Modification, Adv. Mater. 18 (2006) 2226–2229.

[13] K. Yamamoto, T. Minato, S. Mori, D. Takamatsu, Y. Orikasa, H. Tanida, K. Nakanishi, H. Murayama, T. Masese, T. Mori, H. Arai, Y. Koyama, Z. Ogumi, and Y. Uchimoto, Improved Cyclic Performance of Lithium-Ion Batteries: An Investigation of Cathode/Electrolyte Interface via In Situ Total-Reflection Fluorescence X‑ray Absorption Spectroscopy, J. Phys. Chem. C 118 (2014) 9538−9543.

[14] K. Xu, Electrolytes and Interphases in Li-ion Batteries and Beyond, Chem. Rev. 114 (2014) 11503 – 11618.

[15] A. Patil, V. Patil, D. W. Shin, J.-W. Choi, D.-S. Oaik, S.-J. Yoon, Issue and challenges facing rechargeable thin film lithium batteries, Mater. Res. Bull. 43 (2008) 1913 – 1942.

[16] T. Minato, H. Kawaura, M. Hirayama, S. Taminato, K. Suzuki, N. L. Yamada, H. Sugaya, K.

Yamamoto, K. Nakanishi, Y. Orikasa, H. Tanida, R. Kanno, H. Arai, Y. Uchimoto, and Z. Ogumi, Dynamic Behavior at the Interface between Lithium Cobalt Oxide and an Organic Electrolyte Monitored by Neutron Reflectivity Measurements, J. Phys. Chem. C 120 (2016) 20082−20088.

[17] Y. Okada, Y. Ando, R. Shimizu, E. Minamitani, S. Shiraki, S. Watanabe, and T. Hitosugi, Scanning tunneling spectroscopy of superconductivity on surfaces of $LiTi_2O_4$(111) thin films, Nat. Comm. 8 (2017) 15975.

[18] G. A. Somorjai and Y. Li, Introduction to Surface Chemistry and Catalysis (Wiley-VCH) 2010.

[19] G. Ertl, Reactions at Solid Surfaces 2nd Edition (Wiley-VCH) 2009.

[20] S.-K. Jeong, M. Inaba, T. Abe, and Z. Ogumi, Surface Film Formation on Graphite Negative Electrode in Lithium-Ion Batteries, J. Electrochem. Soc. 148 (2001) A989 - A993.

[21] K. Iwaya, T. Ogawa, T. Minato, K. Miyoshi, J. Takeuchi, A. Kuwabara, H. Moriwake, Y. Kim, and T. Hitosugi, Impact of Lithium-Ion Ordering on Surface Electronic States of Li_xCoO_2, Phys. Rev. Lett. 111 (2013) 126104.

[22] K. Weichert, W. Sigle, P. A. van Aken, J. Jamnik, C. Zhu, R. Amin, T. Acartürk, U. Starke, and J. Maier, Phase Boundary Propagation in Large $LiFePO_4$ Single Crystals on Delithiation, J. Am. Chem. Soc. 134 (2012) 2988 – 2992.

[23] S. Kobayashi, C. A. J. Fisher, T. Kato, Y. Ukyo, T. Hirayama, and Y. Ikuhara, Atomic-Scale Observations of (010) $LiFePO_4$ Surfaces Before and After Chemical Delithiation, Nano Lett. 16

(2016) 5409 – 5414.

[24] K. Dokko, M. Nishizawa, M. Mohamedi, M. Umeda, I. Uchida, J. Akimoto, Y. Takahashi, Y. Gotoh, and S. Mizuta, Electrochemical Studies of Li-Ion Extraction and Insertion of $LiMn_2O_4$ Single Crystal, Electrochem. Solid-State Lett., 4(9) (2001) A151-A153.

[25] W. Tang, X. Yang, H. Kanoh, and K. Ooi, Formation and Growth of Spinel-type $LiMn_2O_4$ Single Crystals by LiCl–$MnCl_2$ Flux Evaporation, Chem. Lett. 524 (2001).

[26] Y. Takahashi, N. Kijima, J. Akimoto, Crystal Growth and Structural Properties of the Spinel-type $Li_{1+x}Mn_{2-x}O_4$ (x = 0.10, 0.14), Solid State Ionics 177 (2006) 691 – 695.

[27] P. Strobel and B. L.-Andron, Crystallographic and Magnetic Structure of Li_2MnO_3, J. Solid State Chem. 75 (1998) 90 – 98.

[28] M. Kitta, T. Akita, Y. Maeda, M. Kohyama, Preparation of a Spinel $Li_4Ti_5O_{12}$ (1 1 1) Surface from a Rutile TiO_2 Single Crystal, Appl. Surf. Sci. 258 (2012) 3147 – 3151.

[29] K. Sakamoto, M. Hirayama, N. Sonoyama, D. Mori, A. Yamada, K. Tamura, J. Mizuki, and R. Kanno, Surface Structure of $LiNi_{0.8}Co_{0.2}O_2$: a New Experimental Technique Using in Situ X-ray Diffraction and Two-Dimensional Epitaxial Film Electrodes, Chem. Mater. 21 (2009) 2632-2640.

[30] P. Wobrauschek, X-ray Spectrom. 36 (2007) 289 – 300.

[31] M. Hirayama, N. Sonoyama, T. Abe, M. Minoura, M. Ito, D. Mori, A. Yamada, R. Kanno, T. Terashima, M. Takano, K. Tamura, J. Mizuki, Characterization of electrode/electrolyte interface for

lithium batteries using in situ synchrotron X-ray reflectometry—A new experimental technique for $LiCoO_2$ model electrode, J. Power Sources 168 (2007) 493 – 500.

[32] P. Fenter, N. C. Sturchio, Mineral–water interfacial structures revealed by synchrotron X-ray scattering, Prog. Surf. Sci. 77 (2004) 171 – 258.

[33] M. Mezger, H. Schröder, H. Reichert, S. Schramm, J. S. Okasinski, S. Schöder, V. Honkimäki, M. Deutsch, B. M. Ocko, J. Ralston, M. Rohwerder, M. Stratmann, H. Dosch, Molecular Layering of Fluorinated Ionic Liquids at a Charged Sapphire (0001) Surface, Science 322 (2008) 424 – 428.

[34] J. E. Owejan, J. P. Owejan, S. C. DeCaluwe, J. A. Dura, Solid Electrolyte Interphase in Li-Ion Batteries: Evolving Structures Measured In situ by Neutron Reflectometry, Chem. Mater. 24 (2012), 2133 − 2140.

[35] G. M. Veith,L. Baggetto, R. L. Sacci, R. R. Unocic, W. E. Tenhaeff, J. F. Browning, Direct measurement of the chemical reactivity of silicon electrodes with LiPF6-based battery electrolytes, Chem. Commun. 50 (2014) 3081 − 3084.

[36] T. Minato, H. Kawaura, M. Hirayama, S. Taminato, K. Suzuki, N. L. Yamada, H. Sugaya, K. Yamamoto, K. Nakanishi, Y. Orikasa, H. Tanida, R. Kanno, H. Arai, Y. Uchimoto, and Z. Ogumi, Dynamic Behavior at the Interface between Lithium Cobalt Oxide and an Organic Electrolyte Monitored by Neutron Reflectivity Measurements, J. Phys. Chem. C 120 (2016) 20082 – 20088.

[37] D.P. Abraham, R.D. Twesten, M. Balasubramanian, I. Petrov, J. McBreen, K. Amine, Surface

Changes on $LiNi_{0.8}Co_{0.2}O_2$ Particles during Testing of High-power Lithium-ion Cells, Electrochem. Comm. 4 (2002) 620 – 625.

[38] S. J. Pennycook and P. D. Nellist, Scanning Transmission Electron Microscopy, Springer (2011).

[39] M. Haider, H. Rose, S. Uhlemann, B. Kabius, K. Urban, Towards 0.1 nm Resolution with the First Spherically Corrected Transmission Electron Microscope, J. Electro. Microscopy, 47 (1998) 395 – 405.

[40] M. Linck, P. Hartel, S. Uhlemann, F. Kahl, H. Müller, J. Zach, M. Haider, M. Niestadt, M. Bischoff, J. Biskupek, Z. Lee, T. Lehnert, F. Börrnert, H. Rose, and U. Kaiser, Chromatic Aberration Correction for Atomic Resolution TEM Imaging from 20 to 80 kV, Phys. Rev. Lett. 117, (2016) 076101.

[41] C. Kisielowski, B. Freitag, M. Bischoff, H. van Lin, S. Lazar, G. Knippels, P. Tiemeijer, M. van der Stam, S. von Harrach, M. Stekelenburg, M. Haider, S. Uhlemann, H. Muller, P. Hartel, B. Kabius, D. Miller, I. Petrov, E. A. Olson, T. Donchev, E. A. Kenik, A. R. Lupini, J. Bentley, S. J. Pennycook, I. M. Anderson, A. M. Minor, A. K. Schmid, T. Duden, V. Radmilovic, Q. M. Ramasse, M. Watanabe, R. Erni, E. A. Stach, P. Denes, U. Dahmen, Detection of Single Atoms and Buried Defects in Three Dimensions by Aberration-corrected Electron Microscope with 0.5-Angstrom Information Limit, Microsc. Microanal. 14 (2008) 469 – 477.

[42] R. Huang and Y. Ikuhara, STEM Characterization for Lithium-ion Battery Cathode Materials, Current Opinion in Solid State and Mater. Sci. 16 (2012) 31 – 38.

[43] S. D. Findlay, N. Shibata, H. Sawada, E. Okunishi, Y. Kondo, T. Yamamoto, Y. Ikuhara, Robust Atomic Resolution Imaging of Light Elements Using Scanning Transmission Electron Microscopy, Appl. Phys. Lett. 95 (2009) 191913.

[44] S. D. Findlay, N. Shibata, H. Sawada, E. Okunishi, Y. Kondo, Y. Ikuhara, Dynamics of Annular Bright Field Imaging in Scanning Transmission Electron Microscopy, Ultramiscroscopy, 110 (2010) 903 – 923.

[45] G. Binning, H. Rohrer, Ch. Gerber, and E. Weibel, Surface Studies by Scanning Tunneling Microscopy, Phys. Rev. Lett. 49 (1982) 57 - 61.

[46] G. Binnig, H. Rohrer, Ch. Gerber, and E. Weibel. 7 x 7 Reconstruction on Si(111)Resolved in Real Space, Phys. Rev. Lett. 50 (1983) 120.

[47] R. Wiesendanger, Scanning Probe Microscopy and Spectroscopy, Cambridge University Press (1994).

[48] D. Bonnell, Scanning Probe Microscopy and Spectroscopy, Wiley-VCH (2001).

[49] M. Feng, J. Zhao, H. Petek, Atomlike, Hollow-Core–Bound Molecular Orbitals of C_{60}, Science 320 (2008) 359 – 362.

[50] T. Minato, T. Susaki, S. Shiraki, H. S Kato, M. Kawai, K.-i. Aika, Investigation of the electronic

interaction between TiO_2(110) surfaces and Au clusters by PES and STM, Surf. Sci. 566 (2004) 1012 – 1017.

[51] T. Minato, Y. Sainoo, Y. Kim, H. S Kato, K.-i. Aika, M. Kawai, J. Zhao, H. Petek, T. Huang, W. He, B. Wang, Z. Wang, Y. Zhao, J. Yang, J. G. Hou, The electronic structure of oxygen atom vacancy and hydroxyl impurity defects on titanium dioxide (110) surface, J. Chem. Phys. 130 (2009) 124502.

[52] T. Minato, Atomic Defects in Titanium Dioxide, Chem. Rec. 14 (2014) 923 – 934.

[53] B. C. Stipe, M. A. Rezaei, W. Ho, Single-molecule vibrational spectroscopy and microscopy, Science 280 (1998) 1732 – 1735.

[54] Y. Kim, T. Komeda, M. Kawai, Single-molecule reaction and characterization by vibrational excitation, Phys. Rev. Lett. 89 (2002) 126104.

[55] P. Hapala, R. Temirov, F. S. Tautz, P. Jelinek, Origin of High-Resolution IETS-STM Images of Organic Molecules with Functionalized Tips, Phys. Rev. Lett. 113 (2014) 226101.

[56] V. Madhavan, W. Chen, T. Jamneala, M. F. Crommie, N. S. Wingreen, Tunneling into a single magnetic atom: Spectroscopic evidence of the Kondo resonance, Science 280 (1998) 567 – 569.

[57] R. Wiesendanger, Spin Mapping at the Nanoscale and Atomic Scale, Rev. Mod. Phys. 81 (2009) 1495 – 1550.

[58] H. Gonzalez-Herrero, J. M. Gomez-Rodriguez, P. Mallet, M. Moaied, J. J. Palacios, C. Salgado,

M. M. Ugeda, J. Y. Veuillen, F. Yndurain, I. Brihuega, Atomic-Scale Control of Graphene Magnetism by Using Hydrogen Atoms, Science 352 (2016) 437 – 441.

[59] D. M. Eigler, C. P. Lutz, W. E. Rudge, An Atomic Switch Realized with the Scanning Tunneling Microscope, Nature 352 (1991) 600 – 603.

[60] B. C. Stipe, M. A. Rezaei, W. Ho, Inducing and Viewing the Rotational Motion of a Single Molecule, Science 279 (1998) 1907 - 1909.

[61] Y. Kim, K. Motobayashi, T. Frederiksen, H. Ueba, and M. Kawai, Action Spectroscopy for Single-molecule Reactions -Experiments and Theory-, Prog. Surf. Sci., 90 (2015) 85 - 143.

[62] H. Petek, Single-Molecule Femtochemistry: Molecular Imaging at the Space-Time Limit, ACS Nano 8 (2014) 5 – 13.

[63] T. Minato, M. Kawai, Y. Kim, Creation of Single Oxygen Vacancy on Titanium Dioxide Surface, J. Mater. Res. 27 (2012) 2237 – 2240.

[64] T. Minato, N. Asao, Y. Yamamoto, M. Kawai, Y. Kim, Photoresponse on the Desorption of an Atomic Hydrogen on Titanium Dioxide Surface Induced by a Tip of Scanning Tunneling Microscope, Chem. Lett. 42 (2013) 942 – 943.

[65] T. Minato, S. Kajita, C.-L. Pang, N. Asao, Y. Yamamoto, T. Nakayama, M. Kawai, Y. Kim, ACS Nano 9 (2015) 6837 – 6842.

[66] S. Morita, F. J. Giessibl, R. Wiesendanger, Noncontact Atomic Force Microscopy, Springer

(2009).

[67] T. R. Albrecht, P. Grutter, D. Horne, D. Rugar, Frequency-modulation Detection using High-Q Cantilevers for Enhanced Force Microscope Sensitivity, J. Appl. Phys. 69 (1991) 668 - 673.

[68] F. J. Giessibl, Atomic-resolution of the Silicon (111)-(7X7) Surface by Atomic-Force Microscopy, Science 267 (1995) 68 – 71.

[69] T. Fukuma, T. Ichii, K. Kobayashi, H. Yamada, K. Matsushige, True Atomic Resolution in Liquid by Frequency-Modulation Atomic Force Microscopy, Appl. Phys. Lett. 87 (2005) 034101.

[70] T. Fukuma, Y. Ueda, S. Yoshioka, H. Asakawa, Atomic-Scale Distribution of Water Molecules at the Mica-Water Interface Visualized by Three-Dimensional Scanning Force Microscopy, Phys. Rev. Lett. 104 (2010) 016101.

[71] K. Kimura, S. Ido, N. Oyabu, K. Kobayashi, Y. Hirata, T. Imai, H. Yamada, Visualizing water molecule distribution by atomic force microscopy, J. Chem. Phys. 132 (2009) 194705.

[72] K. Edström, T. Gustafsson, J. O. Thomas, The Cathode−Electrolyte Interface in the Li-Ion Battery. Electrochim. Acta 50 (2004) 397 − 403.

[73] R. Dedryvere, M. Maccario, L. Croguennec, F. Le Cras, C. Delmas, D. Gonbeau, X-Ray Photoelectron Spectroscopy Investigations of Carbon-Coated LixFePO4 Materials, Chem. Mater. 20 (2008) 7164 − 7170.

[74] K. Shimoda, T. Minato, K. Nakanishi, H. Komatsu, T. Matsunaga, H. Tanida, H. Arai, Y. Ukyo,

Y. Uchimoto, Z. Ogumi, Oxidation behaviour of lattice oxygen in Li-rich manganese-based layered oxide studied by hard X-ray photoelectron spectroscopy, J. Mater. Chem. A 4 (2016) 5909 – 5916.

[75] D. Aurbach, B. Markovsky, G. Salitra, E. Markevich, Y. Talyossef, M. Koltypin, L. Nazar, B. Ellis, D. Kovacheva, Review on Electrode-Electrolyte Solution Interactions, Related to Cathode Materials for Li-Ion Batteries. J. Power Sources 165 (2007) 491 – 499.

[76] M. Salmeron and R. Schlogl, Ambient Pressure Photoelectron Spectroscopy: A New Tool for Surface Science and Nanotechnology, Surf. Sci. Rep. 63 (2008) 169 – 199.

[77] S Yamamoto, H Bluhm, K Andersson, G Ketteler, H Ogasawara, M Salmeron, A Nilsson, In Situ X-ray Photoelectron Spectroscopy Studies of Water on Metals and Oxides at Ambient Conditions, J. Phys.: Cond. Mater. 20 (2008) 18402.

[78] R. Toyoshima, M. Yoshida, Y. Monya, Y. Kousa, K. Suzuki, H. Abe, B. S. Mun, K. Mase, K. Amemiya, H. Kondoh, In Situ Ambient Pressure XPS Study of CO Oxidation Reaction on Pd(111) Surfaces, J. Phys. Chem. C 116 (2012) 18691 – 18697.

[79] D. Takamatsu, Y. Koyama, Y. Orikasa, S. Mori, T. Nakatsutsumi, T. Hirano, H. Tanida, H. Arai, Y. Uchimoto, Z. Ogumi, First In Situ Observation of the $LiCoO_2$ Electrode/Electrolyte Interface by Total-Reflection X-ray Absorption Spectroscopy, Angewandte Chemie. 51 (2012) 11597 – 11601.

[80] K. Yamamoto, Y. Orikasa, D. Takamatsu, Y. Koyama, S. Mori, T. Masese, T. Mori, T. Minato, H. Tanida, T. Uruga, Z. Ogumi and Y. Uchimoto, Stabilization of the Electronic Structure at the

Cathode/Electrolyte Interface via MgO Ultra-thin Layer during Lithium-ions Insertion/Extraction, Electrochemistry 82 (2014) 891 – 896.

[81] Y. Orikasa, D. Takamatsu, K. Yamamoto, Y. Koyama, S. Mori, T. Masese, T. Mori, T. Minato, H. Tanida, T. Uruga, Z. Ogumi and Y. Uchimoto, Origin of Surface Coating Effect for MgO on $LiCoO_2$ to Improve the Interfacial Reaction between Electrode and Electrolyte, Adv. Mater. Interf., 1 (2014) 1400195.

[82] D. Takamatsu, Y. Orikasa, S. Mori, T. Nakatsutsumi, K. Yamamoto, Y. Koyama, T. Minato, T. Hirano, H. Tanida, H. Arai, Y. Uchimoto and Z. Ogumi, Effect of an Electrolyte Additive of Vinylene Carbonate on the Electronic Structure at the Surface of a Lithium Cobalt Oxide Electrode under Battery Operating Conditions, J. Phys. Chem. C 119 (2015) 9791 – 9797.

[83] K. Matsui, K. Dokko, K. Kanamura, Dynamic behavior of surface film on $LiCoO_2$ thin film electrode. J. Power Sources 177 (2008) 184 − 193.

[84] K. Motobayashi, K. Minami, N. Nishi, T. Sakka, M. Osawa, Hysteresis of Potential-Dependent Changes in Ion Density and Structure of an Ionic Liquid on a Gold Electrode: In Situ Observation by Surface-Enhanced Infrared Absorption Spectroscopy, Phys. Chem. Chem. Phys. 4 (2013) 3110 – 3114.

[85] J. P. Vivek, N. Berry, G. Papageorgiou, R. J. Nichols, L. J. Hardwick, Mechanistic Insight into the Superoxide Induced Ring Opening in Propylene Carbonate Based Electrolytes using in Situ

Surface-Enhanced Infrared Spectroscopy, J. Am. Chem. Soc. 138 (2016) 3745 – 3751.

[86] Y. Matsuo, R. Kostecki, F. McLarnon, Surface Layer Formation on Thin-film $LiMn_2O_4$ Electrodes at Elevated Temperatures, J. Electrochem. Soc. 148 (2001) A687 – A692.

[87] R. Baddour-Hadjean and J.-P. Pereira-Ramos, Raman Microspectrometry Applied to the Study of Electrode Materials for Lithium Batteries, Chem. Rev. 110 (2010) 1278 – 1319.

[88] Z. C. Zeng, S. C. Huang, D. Y. Wu, L. Y. Meng, M. H. Li, T. X. Huang, J. H. Zhong, X. Wang, Z. L. Yang, B. Ren, Electrochemical Tip-Enhanced Raman Spectroscopy, J. Am. Chem. Soc. 137 (2015) 11928 – 11931.

[89] H. Liu, Y. Tong, N. Kuwata, M. Osawa, J. Kawamura, and Shen Ye, Adsorption of Propylene Carbonate (PC) on the $LiCoO_2$ Surface Investigated by Nonlinear Vibrational Spectroscopy, J. Phys. Chem. Lett. 113 (2009) 20531 – 20534.

[90] L. Yu, H. Liu, Y. Wang, N. Kuwata, M. Osawa, J. Kawamura, and Shen Ye, Preferential Adsorption of Solvents on the Cathode Surface of Lithium Ion Batteries, Angew. Chem. Int. Ed. 52 (2013) 5753 – 5756.

[91] P. Mukherjee, A. Lagutchev and D. D. Dlott, In Situ Probing of Solid-Electrolyte Interfaces with Nonlinear Coherent Vibrational Spectroscopy, J. Electrochem. Soc. 159 (2012) A244 - A252.

[92] G. Ceder, Y. M. Chiang, D. R. Sadoway, M. K. Aydinol, Y. I. Jang, B. Huang, Identification of Cathode Materials for Lithium Batteries Guided by First-principles Calculations, Nature 392 (1998)

694 – 696.

[93] Y. S. Li, K. Leung, Y. Qi, Computational Exploration of the Li-Electrode Electrolyte Interface in the Presence of a Nanometer Thick Solid-Electrolyte Interphase Layer, Acc. Chem. Res. 49 (2016) 2363 – 2370.

[94] K. Sodeyama, Y. Yamada, K. Aikawa, A. Yamada, Y. Tateyama, Sacrificial Anion Reduction Mechanism for Electrochemical Stability Improvement in Highly Concentrated Li-Salt Electrolyte, J. Phys. Chem. C 118 (2014) 14091 – 14097.

[95] M. A. Van Hove, W.H. Weinberg, C. M. Chan, Low-Energy Electron Diffraction. Springer (1986).

[96] R. Brydson, Electron Energy Loss Spectroscopy, Garland Science (2001).

[97] C. V. Cushman, P. Brüner, J. Zakel, G. H. Major, B. M. Lunt, N. J. Smith, T. Grehl and M. R. Linford, Low energy ion scattering (LEIS). A practical introduction to its theory, instrumentation, and applications, Analytical Methods 8 (2016) 3419 – 3439.

[98] T. Kondo, S. Mae, H. S.Kato, M. Kawai, Morphological change of D_2O layers on Ru(0001) probed with He atom scattering, Surf. Sci. 600 (2006) 3570 – 3574.

[99] D. Kramer and G. Ceder, Tailoring the Morphology of $LiCoO_2$: A First Principles Study, Chem. Mater. 21 (2009) 3799 – 3809.

[100] A. K. Padhi, K. S. Nanjundaswamy, J. B. Goodenough, Phospho-Olivines as Positive-

Electrode Materials for Rechargeable Lithium Batteries, J. Electrochem. Soc. 144 (1997) 1188 − 1194.

[101] L. Wang, F. Zhou, Y. S. Meng, and G. Ceder, First-principles Study of Surface Properties of $LiFePO_4$: Surface Energy, Structure, Wulff Shape, and Surface Redox Potential, Phys. Rev. B 76, (2007) 165435.

[102] C. A. J. Fisher and M. S. Islam, Surface Structures and Crystal Morphologies of $LiFePO_4$: Relevance to Electrochemical Behavior, J. Mater. Chem. 18 (2008) 1209 – 1215.

[103] M. S. Islam, D. J. Driscoll, C. A. J. Fisher, P. R. Slater, Atomic-scale Investigation of Defects, Dopants, and Lithium Transport in the $LiFePO_4$ Olivine-type Battery Material, Chem. Mater. 17 (2005) 5085 – 5092.

[104] D. Morgan, A. Van der Ven, and G. Ceder, Li Conductivity in Li_xMPO_4 (M = Mn, Fe, Co, Ni) Olivine Materials, Electrochem. Solid-State Lett. 7 (2004) A30 - A32.

[105] C. Y. Ouyang, S. Q. Shi, Z. X. Wang, X. J. Huang, L. Q. Chen, First-principles Study of Li Ion Diffusion in $LiFePO_4$, Phys. Rev. B 69 (2004) 104303.

[106] M. M. Thackeray, W. I. F. David, P. G. Bruce and J. B. Goodenough, Lithium Insertion into Manganese Spinels, Mater. Res. Bull. 18 (1983) 461 - 472.

[107] R. Benedek and M. M. Thackeray, Simulation of the Surface Structure of Lithium Manganese Oxide Spinel, Phys. Rev. B 83 (2011) 195439.

[108] A. Karim, S. Fosse and K. A. Persson, Surface Structure and Equilibrium Particle Shape of the $LiMn_2O_4$ Spinel from First-principles Calculations, Phys. Rev. B 87 (2013) 075322.

[109] T. Takada, H. Hayakawa, H. Enoki, E. Akiba, H. Slegr, I. Davidson, J. Murray, Structure and Electrochemical Characterization of $Li_{1+x}Mn_{2-x}O_4$ Spinels for Rechargeable Lithium Batteries, J. Power Sources 81−82 (1999) 505 − 509.

[110] W. Tang, X. Yang, Z. Liu, S. Kasaishi, K. Ooi, Preparation of Fine Single Crystals of Spinel-Type Lithium Manganese Oxide by LiCl Flux Method for Rechargeable Lithium Batteries. Part 1. $LiMn_2O_4$, J. Mater. Chem. 12 (2002) 2991 − 2997.

[111] I. Taniguchi, C. K. Lim, D. Song, M. Wakihara, Particle Morphology and Electrochemical Performances of Spinel $LiMn_2O_4$ Powders Synthesized Using Ultrasonic Spray Pyrolysis Method, Solid State Ionics 146 (2002) 239 − 247.

[112] K. Matsuda, I. Taniguchi, Relationship between the Electrochemical and Particle Properties of $LiMn_2O_4$ Prepared by Ultrasonic Spray Pyrolysis. J. Power Sources 132 (2004) 156 − 160.

[113] M.-R. Huang, C.-W. Lin, H.-Y. Lu, Crystallographic Facetting in Solid-State Reacted $LiMn_2O_4$ Spinel Powder. Appl. Surf. Sci. 177 (2001) 103 − 113.

[114] K. R. Chemelewski, E.-S. Lee, W. Li, A. Manthiram, Factors Influencing the Electrochemical Properties of High-Voltage Spinel Cathodes: Relative Impact of Morphology and Cation Ordering, Chem. Mater. 25 (2013) 2890 − 2897.

[115] R. E. Warburton, H. Iddir, L. A. Curtiss, and J. Greeley, Thermodynamic Stability of Low- and High-Index Spinel $LiMn_2O_4$ Surface Terminations, ACS Appl. Mater. Interf. 8 (2016) 11108 – 11121.

[116] J.-S. Kim, K. S. Kim, W. Cho, W. Ho Shin, R. Kanno and J. W. Choi, A Truncated Manganese Spinel Cathode for Excellent Power and Lifetime in Lithium-Ion Batteries, Nano Lett. 12 (2012) 6358 − 6365.

[117] K. Suzuki, N. Oyabu, K. Kobayashi, K. Matsushige, and H. Yamada, Atomic-Resolution Imaging of Graphite–Water Interface by Frequency Modulation Atomic Force Microscopy, Appl. Phys. Exp. 4 (2011) 125102.

[118] Y. Domi, M. Ochida, S. Tsubouchi, H. Nakagawa, T. Yamanaka, T. Doi, T. Abe and Z. Ogumi, In Situ AFM Study of Surface Film Formation on the Edge Plane of HOPG for Lithium-Ion Batteries, J. Phys. Chem. C 115 (2015) 25484 – 25489.

[119] Y. Domi, T. Doi, T. Yamanaka, T. Abe and Z. Ogumi, Electrochemical AFM Study of Surface Films Formed on the HOPG Edge Plane in Propylene Carbonate-Based Electrolytes, J. Electrochem. Soc. 160 (2013) A678 - A683.

[120] T. Ohzuku, A. Ueda, and N. Yamamoto, Zero‐Strain Insertion Material of $Li[Li_{1/3}Ti_{5/3}]O_4$ for Rechargeable Lithium Cells, J. Electrochem. Soc. 142 (1995) 1431 - 1435.

[121] K. Ariyoshi, R. Yamato, and T. Ohzuku, Zero-strain Insertion Mechanism of $Li[Li_{1/3}Ti_{5/3}]O_4$

for Advanced Lithium-ion (Shuttlecock) Batteries, Electrochim. Acta 51 (2005) 1125 - 1129.

[122] M. Kitta, T. Matsuda, Y. Maeda, T. Akita, S. Tanaka, Y. Kido, M. Kohyama, Atomistic Structure of a Spinel $Li_4Ti_5O_{12}$(111) Surface Elucidated by Scanning Tunneling Microscopy and Medium Energy Ion Scattering Spectrometry, Surf. Sci. 619 (2014) 5 – 9.

[123] M. Kitta, M. Kohyama and H. Onishi, True Atomic-scale Imaging of a Spinel $Li_4Ti_5O_{12}$(111) Surface in Aqueous Solution by Frequency-Modulation Atomic Force Microscopy, Appl. Phys. Lett. 105 (2014) 111606.

[124] M. Kitta, T. Akita and M. Kohyama, Spontaneous Li-Ion Transfer from Spinel $Li_4Ti_5O_{12}$ Surfaces: Deterioration at $Li_4Ti_5O_{12}$/Electrolyte Interfaces Stored at Room Temperature, J. Electrochem. Soc. 162 (2015) A1272 - A1275.

[125] M. Kitta and M. Kohyama, Nanoscale Controlled Li-insertion Reaction Induced by Scanning Electron-beam Irradiation in a $Li_4Ti_5O_{12}$ Electrode Material for Lithium-ion Batteries, Phys. Chem. Chem. Phys. 19 (2017) 11581 - 11587.

[126] Q. Wang, H.-T. Yu, Y. Xie, M.-X. Li, T.-F. Yi, C.-F. Guo, Q.-S. Song, M. Lou, S.-S. Fan, Structural Stabilities, Surface Morphologies and Electronic Properties of Spinel $LiTi_2O_4$ as Negative Electrode Materials for Lithium-ion Battery: A First Principles Investigation, J. Power Sources 319 (2016) 185 – 194.

[127] L. Hu, Z. Xiong, C. Ouyang, S. Shi, Y. Ji, M. Lei, Z. Wang, H. Li, X. Huang, and L. Chen, Ab

Initio Studies on the Stability and Electronic Structure of $LiCoO_2$(003) Surfaces, Phys. Rev. B 71 (2005) 125433.

[128] D. Qian, Y. Hinuma, H. Chen, L.-S. Du, K. J. Carroll, G. Ceder, C. P. Grey and Y. S. Meng, Electronic Spin Transition in Nanosize Stoichiometric Lithium Cobalt Oxide, J. Am. Chem. Soc. 134 (2012) 6096 – 6099.

[129] X. Huang, J. W. Bennett, M. N. Hang, E. D. Laudadio, R. J. Hamers, and S. E. Mason, Ab Initio Atomistic Thermodynamics Study of the (001) Surface of $LiCoO_2$ in a Water Environment and Implications for Reactivity under Ambient Conditions, J. Phys. Chem. C 121 (2017) 5069 – 5080.

[130] F. Zhou, K. Kang, T. Maxisch, G. Ceder, D. Morgan, The Electronic Structure and Band Gap of $LiFePO_4$ and $LiMnPO_4$, Solid State Communications 132 (2004) 181– 186.

[131] V. Timoshevskii, Z. Feng, K. H. Bevan, and K. Zaghib, Emergence of Metallic Properties at $LiFePO_4$ Surfaces and $LiFePO_4/Li_2S$ Interfaces: An Ab Initio Study, ACS Appl. Mater. Interfaces 7 (2015) 18362 − 18368.

[132] X. Ouyanga, M. Lei, S. Shi, C. Luo, D. Liu, D. Jiang, Z. Ye, M. Lei, First-principles Studies on Surface Electronic Structure and Stability of $LiFePO_4$, J. Alloy. Comp. 476 (2009) 462 – 465.

[133] C. Y. Ouyang, X. M. Zeng, Z. S. ljivancanin and A. Baldereschi, Oxidation States of Mn Atoms at Clean and Al_2O_3-Covered $LiMn_2O_4$(001) Surfaces, J. Phys. Chem. C 114 (2010) 4756 – 4759.

[134] T. Eriksson, T. Gustafsson, J. O. Thomas, Electrochem. Solid-State Lett. Surface Structure of $LiMn_2O_4$ Electrodes, 5 (2002) A35 – A38.

[135] R. E. Warburton, H. Iddir, L. A. Curtiss and J. Greeley, Thermodynamic Stability of Low- and High-Index Spinel $LiMn_2O_4$ Surface Terminations, ACS Appl. Mater. Interf. 8 (2016) 11108 – 11121.

[136] J.-S. Kim, K. S. Kim, W. Cho, W. Ho Shin, R. Kanno and J. W. Choi, A Truncated Manganese Spinel Cathode for Excellent Power and Lifetime in Lithium-Ion Batteries, Nano Lett. 12 (2012) 6358 − 6365.

[137] M. Hirayama, H. Ido, K. S. Kim, W. Cho, K. Tamura, J. Mizuki and R. Kanno, Dynamic Structural Changes at $LiMn_2O_4$/Electrolyte Interface during Lithium Battery Reaction, J. Am. Chem. Soc. 132 (2010) 15268 – 15276.

[138] Th. Fauster and F. J. Himpsel, J. E. Fischer and E. W. Plummer, Three-Dimensional Energy Band in Graphite and Lithium-Intercalated Graphite, Phys. Rev. Lett. 51 (1983) 430 – 433.

[139] A. Selloni, P. Carnevali, E. Tosatti and C. D. Chen, Voltage-dependent Scanning-tunneling Microscopy of a Crystal Surface: Graphite, Phys. Rev. B 31 (1985) 2602 – 2605.

[140] B.Reihl, J. K. Gilnzewski, J. M. Nicholls, and E. Tosatti, Unoccupied Electronic States of Graphite as Probed by Inverse-photoemission and Tunneling Spectroscopy, Phys. Rev. B 33 (1986) 5770 – 5773.

[141] H. Fuchs and E. Tosatti, Unoccupied Electronic States of a Graphite Surface as Observed by Local Tunnelling Spectroscopy, Europhys. Lett., 3(6) (1987) 745 – 749.

[142] R. C. Tatar and S. Rabii, Electronic Properties of Graphite: A Unified Theoretical Study, Phys. Rev. B 25 (1982) 4126 – 4141.

[143] S. Tan, L. Liu, Y. Dai, J. Ren, J. Zhao and H. Petek, Ultrafast Plasmon-Enhanced Hot Electron Generation at Ag Nanocluster/Graphite Heterojunctions, J. Am. Chem. Soc. 139 (2017) 6160 − 6168.

[144] Y. Niimi, T. Matsui, H. Kambara, K. Tagami, M. Tsukada, and H. Fukuyama, Scanning Tunneling Microscopy and Spectroscopy of the Electronic Local Density of States of Graphite Surfaces Near Monoatomic Step Edges, Phys. Rev. B 73 (2006) 085421.

[145] S. E. Stein and R.L. Brown, π-Electron Properties of Large Condensed Polyaromatic Hydrocarbons, J. Am. Chem. Soc. 109 (1987) 3721 - 3729.

[146] D. J. Klein, Graphitic Polymer Strips with Edge States, Chem. Phys. Lett. 217 (1994) 261 - 265.

[147] K. Nakada, M. Fujita, G. Dresselhaus and M. Dresselhaus, Edge State in Graphene Ribbons: Nanometer Size Effect and Edge Shape Dependence, Phys. Rev. B 54 (1996) 17954.

[148] K. Wakabayashi, M. Fujita, H. Ajiki and M. Sigrist, Electronic and Magnetic Properties of Nanographite Ribbons, Phys. Rev. B 59 (1999) 8271 - 8282.

[149] K. Kusakabe and M. Maruyama, Magnetic Nanographite, Phys. Rev. B 67 (2003) 092406.

[150] M. Kastler, J. Schmidt, W. Pisila, D. Sebastiani and K. Müllen, From Armchair to Zigzag Peripheries in Nanographenes, J. Am. Chem. Soc. 128 (2006) 9526 - 9534.

[151] D. Jiang and B.G. Sumpter, Unique Chemical Reactivity of a Graphene Nanoribbon's Zigzag Edge, J. Chem. Phys. 126 (2007) 134701.

[152] K. Wakabayashi, Y. Takane and M. Sigrist, Perfectly Conducting Channel and Universality Crossover in Disordered Graphene Nanoribbons, Phys. Rev. Lett. 99 (2007) 036601.

[153] L. Pisani, J.A. Chan, B. Montanari and N.M. Harrison, Electronic Structure and Magnetic Properties of Graphitic Ribbons, Phys. Rev. B 75 (2007) 064418.

[154] Y. Shibayama, H. Sato, T. Enoki and M. Endo, Disordered Magnetism at the Metal-Insulator Threshold in Nano-Graphite-Based Carbon Materials, Phys. Rev. Lett. 84 (2000) 1744.

[155] P. Esquinazi, A. Setzer, R. Höhne, C. Semmelhack, Y. Kopelevich, D. Spemann, T. Butz, B. Kohlstrunk and M. Lösche, Ferromagnetism in Oriented Graphite Samples, Phys. Rev. B 66 (2002) 024429.

[156] P. Esquinazi, D. Spemann, R. Höhne, A. Setzer, K. -H. Han and T. Butz, Induced Magnetic Ordering by Proton Irradiation in Graphite, Phys. Rev. Lett. 91 (2003) 227201.

[157] P. O. Lehtinen, A. S. Foster, Y. Ma, A. V. Krasheninnikov and R. M. Nieminen, Irradiation-Induced Magnetism in Graphite: A Density Functional Study, Phys. Rev. Lett. 93 (2004) 187202.

[158] S. Tanaka, M. Kitta, T. Tamura, Y. Maeda, T. Akita, M. Kohyama, Atomic and Electronic Structures of $Li_4Ti_5O_{12}/Li_7Ti_5O_{12}$(001) Interfaces by First-principles Calculations, J. Mater. Sci. 49 (2014) 4032 – 4037.

[159] Y. Tanaka, M. Ikeda, M. Sumita T. Ohno and K. Takada, First-principles Analysis on Role of Spinel (111) Phase Boundaries in $Li_{4+3x}Ti_5O_{12}$ Li-ion Battery Anodes, Phys. Chem. Chem. Phys. 18 (2016) 23383 - 23388.

[160] M. Kitta, T. Akita, S. Tanaka and M. Kohyama, Two-phase Separation in a Lithiated Spinel $Li_4Ti_5O_{12}$ Crystal as Confirmed by Electron Energy-loss Spectroscopy, J. Power Sources 257 (2014) 120 - 125.

[161] E. G. Leggesse, R. T. Lin, T.-F. Teng, C.-L. Chen, J.-C. Jiang, Oxidative Decomposition of Propylene Carbonate in Lithium Ion Batteries: A DFT Study. J. Phys. Chem. A 117 (2013) 7959 − 7969.

[162] D. Aurbach, Y. Ein-Eli, O. Chusid, C. Y. Youngman, M. Babai, H. J. Yamin, The Correlation Between the Surface-Chemistry and the Performance of Li-carbon Intercalation Anodes for Rechargeable Rocking-Chair Type Batteries, Electrochem. Soc. 141 (1994) 603 – 611.

[163] D. Aurbach, Y. Ein-Eli, B. Markovsky, A. Zaban, S. Luski, Y. Carmeli, H. J. Yamin, The Study of Electrolyte-Solutions Based on Ethylene and Diethyl Carbonates for Rechargeable Li Batteries 2. Graphite-electrodes, Electrochem. Soc. 142 (1995) 2882 – 2890.

[164] Y. Ein-Eli, S. R. Thomas, V. Koch, D. Aurbach, B. Markovsky, A. Schechter, Ethylmethylcarbonate, a Promising Solvent for Li-ion Rechargeable Batteries, J. Electrochem. Soc. 143 (1996) L273 – L277.

[165] D. Aurbach, B. Markovsky, A. Shechter, Y. Ein-Eli, H. Cohen, A Comparative Study of Synthetic Graphite and Li Electrodes in Electrolyte Solutions Based on Ethylene Carbonate Dimethyl Carbonate Mixtures, J. Electrochem. Soc. 143 (1996) 3809 – 3820.

[166] Y. Ein-Eli, S. F. McDevitt, D. Aurbach, B. Markovsky, A. Schechter, Methyl Propyl Carbonate: A Promising Single Solvent for Li-ion Battery Electrolytes, J. Electrochem. Soc. 144 (1997) L180 – L184.

[167] D. Aurbach, M. D. Levi, E. Levi, H. Telier, B. Markovsky, G. Salitra, U. Heider, L. Hekier, Common Electroanalytical Behavior of Li Intercalation Processes into Graphite and Transition Metal Oxides, J. Electrochem. Soc. 145 (1998) 3024 – 3034.

[168] D. Aurbach, A. Zaban, Y. Ein-Eli, I. Weissman, O. Chusid, B. Markovsky, M. Levi, E. Levi, A. Schechter, E. Granot, Recent Studies on the Correlation Between Surface Chemistry, Morphology, Three-dimensional Structures and Performance of Li and Li-C Intercalation Anodes in Several Important Electrolyte Systems, J. Power Sources 68 (1997) 91 – 98.

[169] D. Aurbach, M. D. Levi, E. Levi, A. Schechter, Failure and Stabilization Mechanisms of Graphite Electrodes, J. Phys. Chem. B 101 (1997) 2195 – 2206.

[170] D. Aurbach, B. Markovsky, I. Weissman, E. Levi, Y. Ein-Eli, On the Correlation Between Surface Chemistry and Performance of Graphite Negative Electrodes for Li Ion Batteries, Electrochim. Acta, 45 (1999) 67 – 86.

[171] Y.-G. Ryu, S.-I. Pyun, Passivation Kinetics of Surface Films formed on a Graphite Electrode in Organic Lithium Salt Solution as a Function of Salt Anion Type, J. Electroanal. Chem. 433 (1997) 97 – 105.

[172] Y. B. Roh, K. M. Jeong, H. G. Cho, H. Y. Kang, Y. S. Lee, S. K. Ryu, B. S. Lee, Unique Charge/discharge Properties of Carbon Materials with Different Structures, J. Power Sources 68 (1997) 271 – 276.

[173] E. Peled, D. Golodnitsky, C. Menachem, D. Bar-Tow, An Advanced Tool for the Selection of Electrolyte Components for Rechargeable Lithium Batteries, J. Electrochem. Soc. 145 (1998) 3482 – 3486.

[174] D. Bar-Tow, E. Peled, L. Burstein, A Study of Highly Oriented Pyrolytic Graphite as a Model for the Graphite Anode in Li-ion Batteries, J. Electrochem. Soc. 146 (1999) 824 – 832.

[175] K. Kanamura, S. Shiraishi, H. Takezawa, Z. Takehara, XPS Analysis of the Surface of a Carbon Electrode Intercalated by Lithium Ions, Chem. Mater. 9 (1997) 1797 – 1804.

[176] H. Yoshida, T. Fukunaga, T. Hazama, M. Terasaki, M. Mizutani, M. Yamachi, Degradation Mechanism of Alkyl Carbonate Solvents used in Lithium-ion Cells during Initial Charging, J. Power

Sources 68 (1997) 311 – 315.

[177] A. Naji, J. Ghanbaja, P. Willmann, B. Humbert, D. Billaud, First Characterization of the Surface Compounds formed during the Reduction of a Carbonaceous Electrode in $LiClO_4$-Ethylene Carbonate Electrolyte, J. Power Sources 62 (1996) 141 – 143.

[178] M. Dolle, S. Grugeon, B. Beaudoin, L. Dupont, J.-M. Transcon, In Situ TEM Study of the Interface Carbon/Electrolyte, J. Power Sources 97 - 98 (2001) 104 – 106.

[179] A. Naji, J. Ghanbaja, B. Humbert, P. Willmann, D. Billaud, Electroreduction of Graphite in $LiClO_4$-ethylene Carbonate Electrolyte. Characterization of the Passivating Layer by Transmission Electron Microscopy and Fourier-transform Infrared Spectroscopy, J. Power Sources 63 (1996) 33 – 39.

[180] Y. Domi, T. Doi, H. Nakagawa, T. Yamanaka, T. Abe, and Z. Ogumi, In Situ Raman Study on Reversible Structural Changes of Graphite Negative-Electrodes at High Potentials in $LiPF_6$-Based Electrolyte Solution, J. Electrochem. Soc. 163 (2016) A2435 - A2440.

[181] Y. Domi, T. Doi, S. Tsubouchi, T. Yamanaka, T. Abe and Z. Ogumi, Irreversible Morphological Changes of a Graphite Negative-electrode at High Potentials in $LiPF_6$-based Electrolyte Solution, Phys. Chem. Chem. Phys. 18, 2016, 22426 — 22433.

[182] J. Amelie, D. G. Frank, G. Vankó, M. Calandra and C. Brouder, Angular Dependence of Core Hole Screening in $LiCoO_2$: A DFT+U Calculation of the Oxygen and Cobalt *K*-edge X-ray

Absorption Spectra, Phys. Rev. B 81 (2010) 115115.

[183] Y. Iriyama, H. Kurita, I. Yamada, T. Abe, Z. Ogumi, Effects of Surface Modification by MgO on Interfacial Reactions of Lithium Cobalt Oxide Thin Film Electrode, J. Power Sources 137 (2004) 111 – 116.

[184] T. Abe, H. Fukuda, Y. Iriyama and Z. Ogumi, Solvated Li-Ion Transfer at Interface Between Graphite and Electrolyte, J. Electrochem. Soc. 151 (2004) A1120 - A1123.

[185] K. Itaya, In Situ Scanning Tunneling Microscopy in Electrolyte Solutions, Prog. in Surf. Sci. 58 (1998) 121 – 247.

[186] H. Imada, K. Kimura and H. Onishi, Water and 2‑Propanol Structured on Calcite(104) Probed by Frequency-Modulation Atomic Force Microscopy Langmuir, 29 (2013) 10744 – 10751.

[187] K. Fukui, Y. Yokota, A. Imanishi, Local Analyses of Ionic Liquid/Solid Interfaces by Frequency Modulation Atomic Force Microscopy and Photoemission Spectroscopy, Chem. Rec. 14 (2014) 964 - 973.

[188] T. Minato, Y. Araki, K. Umeda, T. Yamanaka, K.-i. Okazaki, H. Onishi, T. Abe, Z. Ogumi, Interface structure between tetraglyme and graphite, J. Chem. Phys. 147 (2017) 124701.

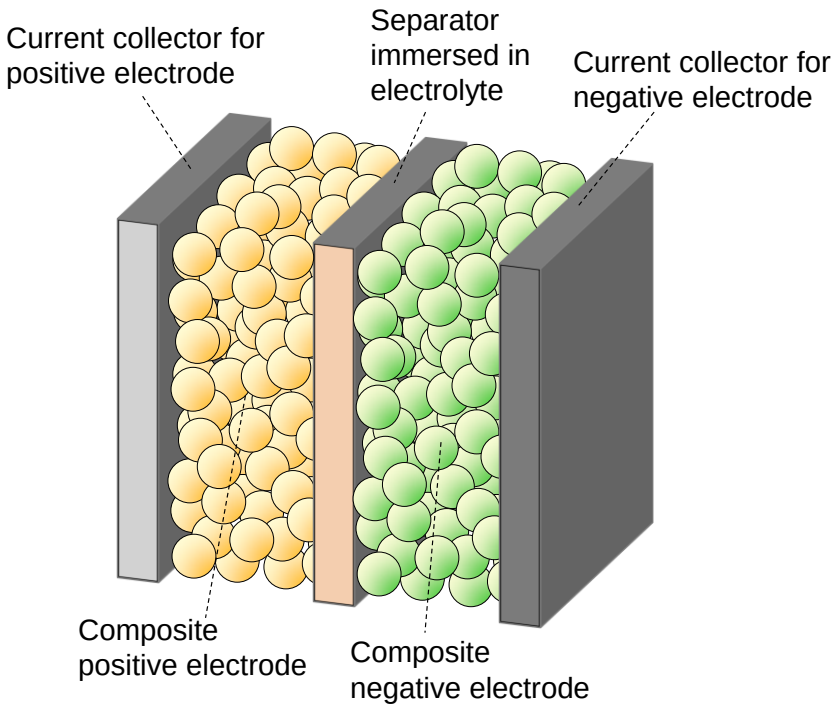

Figure 1. Schematic model of typical structure of an industrial Li-ion battery.

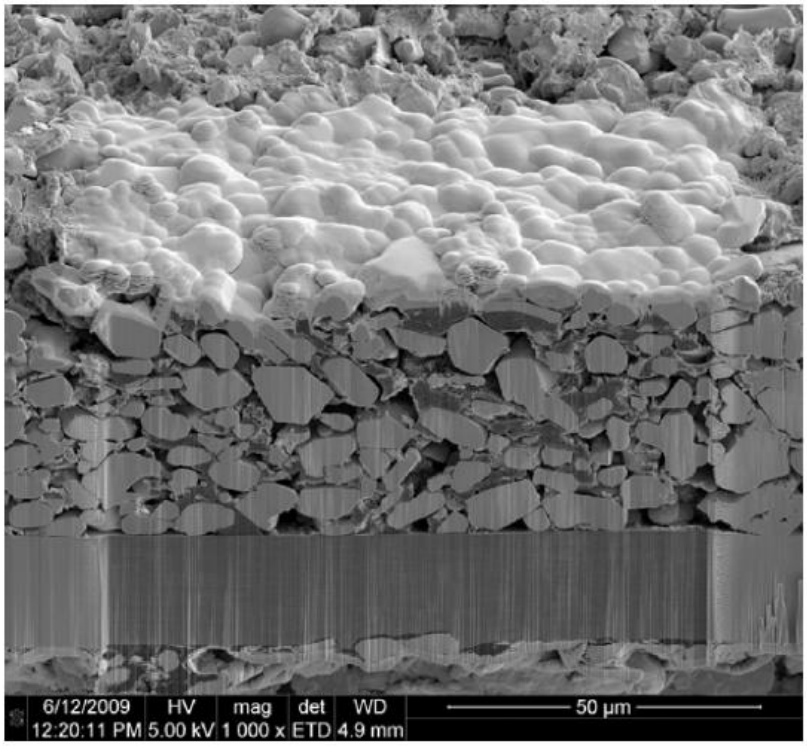

Figure 2. An example of cross-sectional SEM image of $LiCoO_2$ composite electrode prepared by 94.5% $LiCoO_2$, 2.0% carbon black, and 3.5% polyvinylidene fluoride (PVdF) by the weight. The horizontal dark band near bottom of image is aluminum current collector. The composite electrode is located on the aluminum current collector. In the composite electrode, bright, gray and dark regions are observed. The bright regions are the active material ($LiCoO_2$). The gray regions are mixtures of conductive material (carbon black) and binder (PVdF). The dark regions are pore domains. The pore domains are occupied by electrolyte in Li-ion battery. Reprinted with permission from Ref. 8. 2011, The Electrochemical Society.

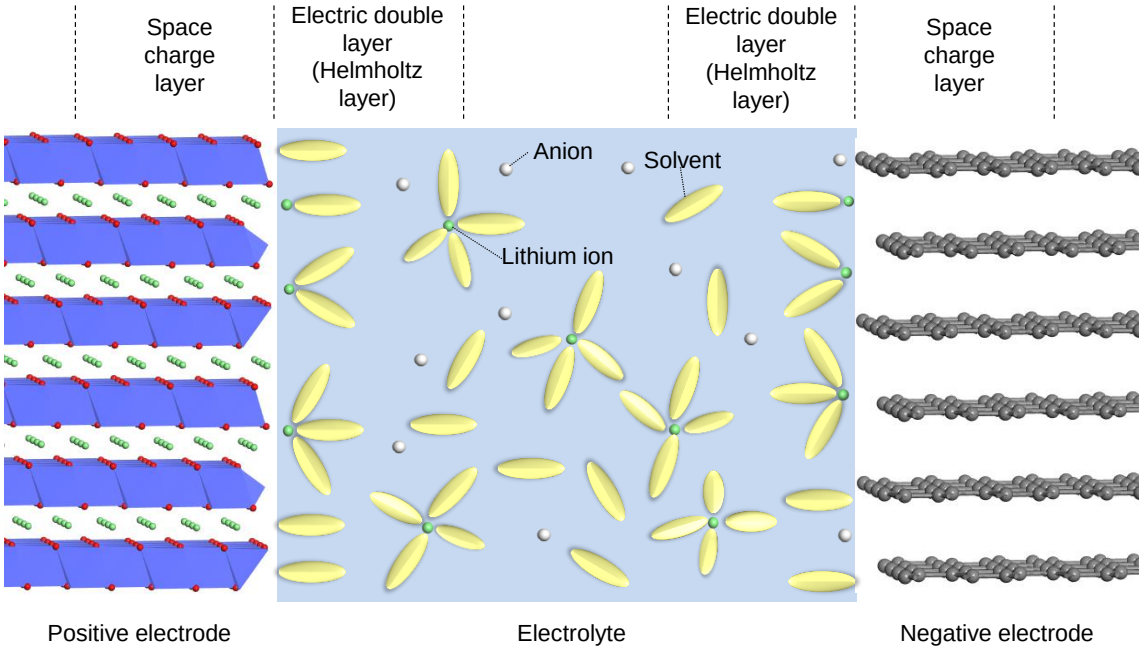

Figure 3. Schematic model of the structure of the interface between electrode and electrolyte. Green and white balls are Li ions and anions, respectively. Yellow ellipses are solvent molecules. Positive and negative electrodes having layered structures are shown as examples.

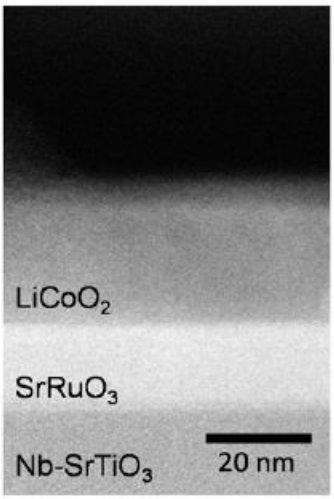

Figure 4. Cross sectional TEM image of an epitaxial $LiCoO_2$ thin film grown on $SrRuO_3$/Nb-$SrTiO_3$.

Reprinted with permission from Ref. 16. Copyright 2016 American Chemical Society.

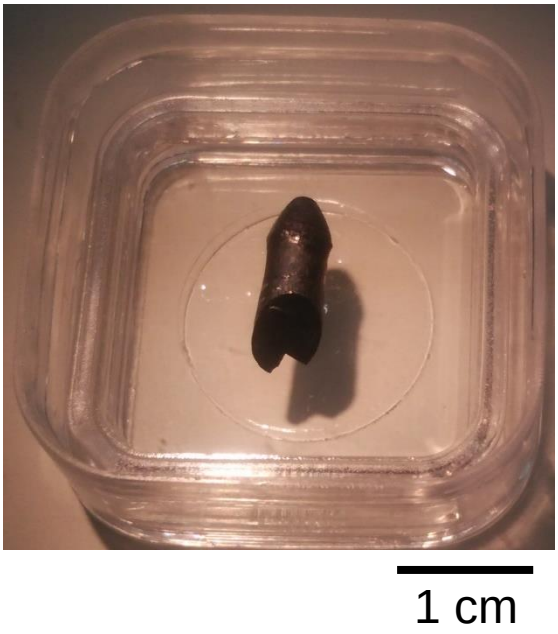

Figure 5. A photograph of the prepared single crystal of $LiCoO_2$.

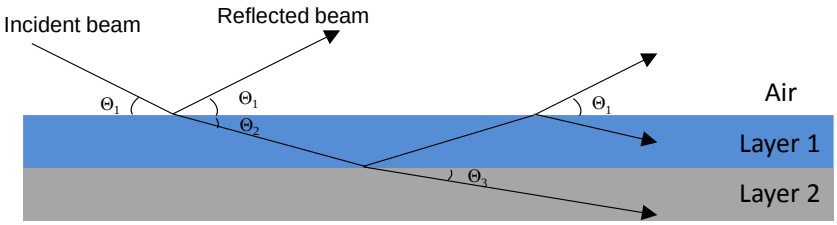

Figure 6. Schematic model of reflection of X-ray or neutron at interface between layers.

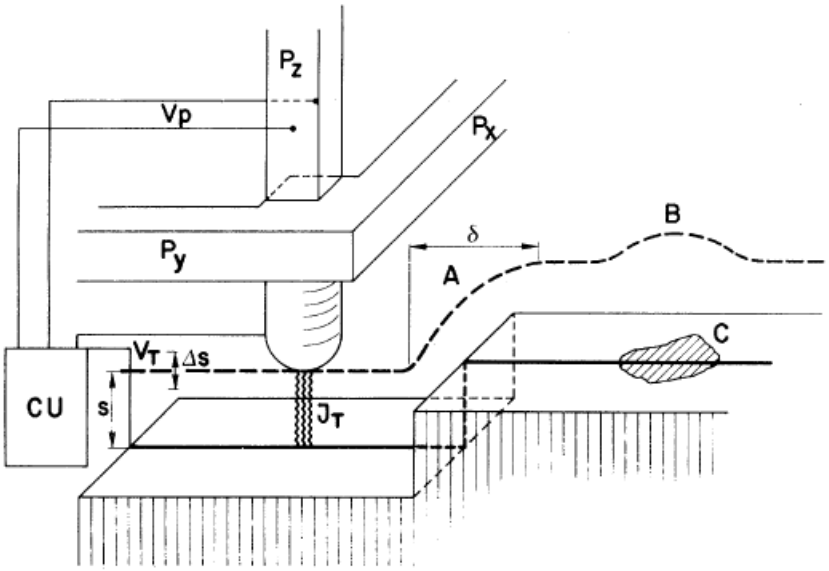

Figure 7. First schematic model of scanning tunneling microscope shown in Ref. 45. Reprinted figure with permission from Ref. 45. Copyright 1982 by the American Physical Society.

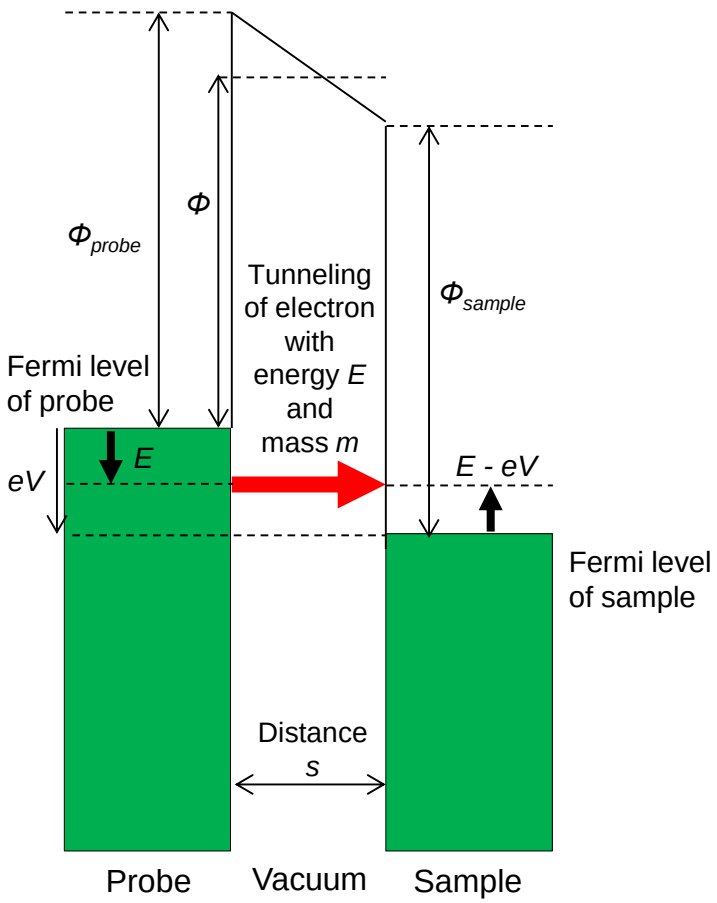

Figure 8. Potential model of tunneling junction in scanning tunneling microscopy.

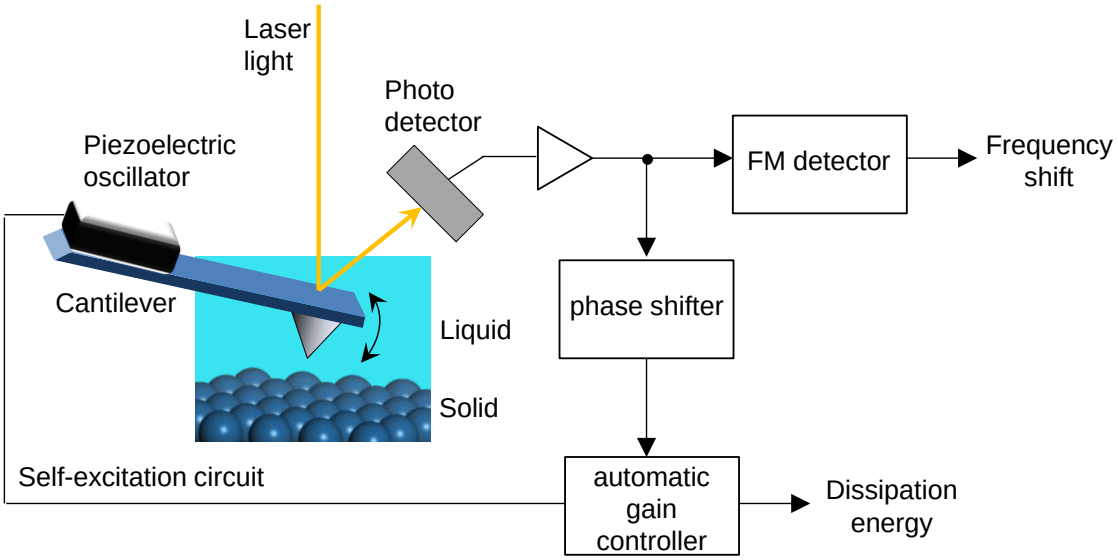

Figure 9. Schematic model of frequency-modulation atomic force microscopy in liquid.

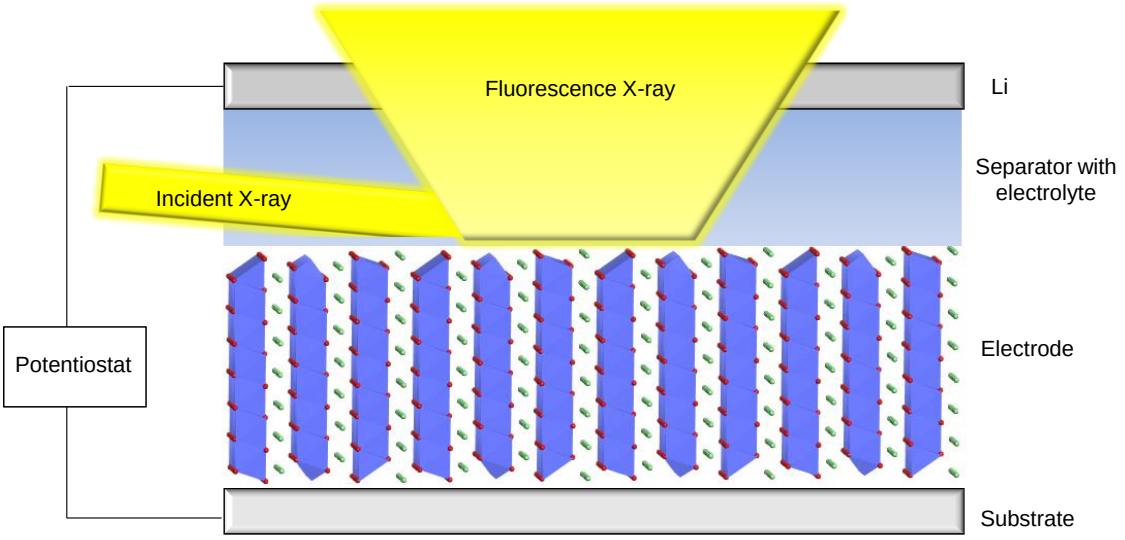

Figure 10. Schematic model of measurement system of total reflection fluorescence X-ray absorption spectroscopy in electrochemical condition.

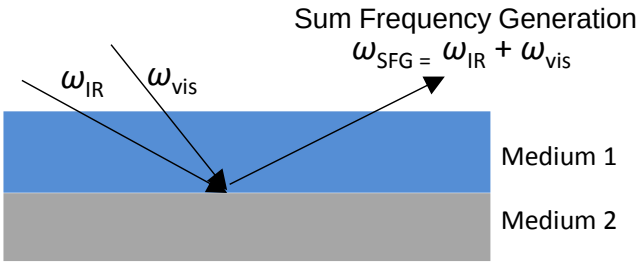

Figure 11. Schematic model of sum frequency generation due to irradiation of IR and visible (wavelength = ω_{IR} and ω_{vis}) light.

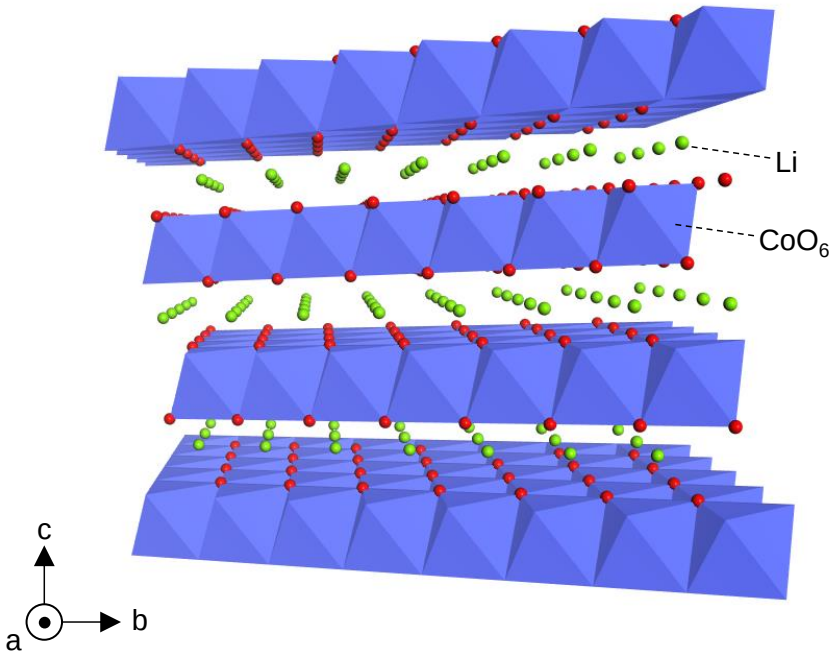

Figure 12. Crystal structure of $LiCoO_2$. Green and red balls show Li and O, respectively. Blue octahedrons show CoO_6 units.

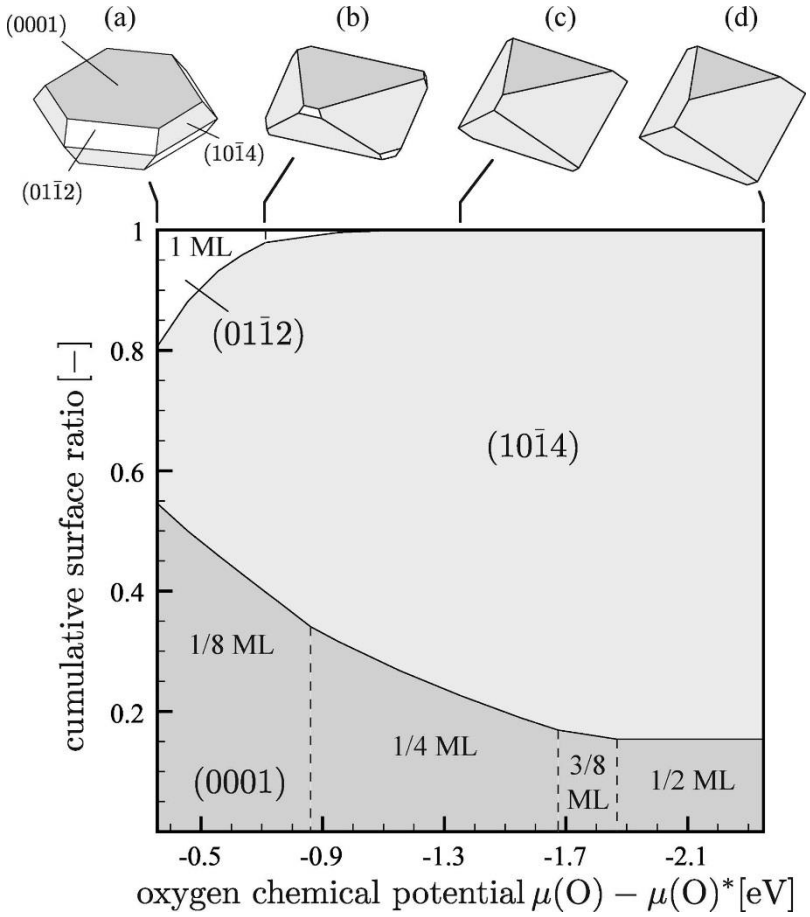

Figure 13. Selected equibrum shapes of $LiCoO_2$ and relative contribution of each surface as a function of the oxygen chemical potential in a Li deficient environment calculated by first principles calculation. Reprinted with permission from Ref. 99. Copyright 2016 American Chemical Society.

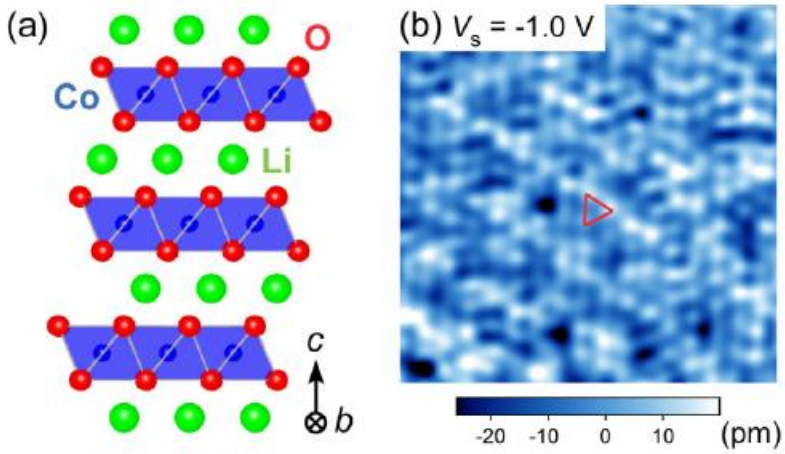

Figure 14. (a) Surface structure of $LiCoO_2$(001) and (b) corresponding constant current STM image of a $Li_{0.66}CoO_2$(001) surface measured at ~5 K, showing hexagonal lattice of Li ions at the surface 4.8 × 4.8 nm^2, sample bias voltage (V_s) = -1.0 V, and tunneling current (I_t) = 0.2 nA. Reprinted figure with permission from Ref. 21. Copyright 2013 by the American Physical Society.

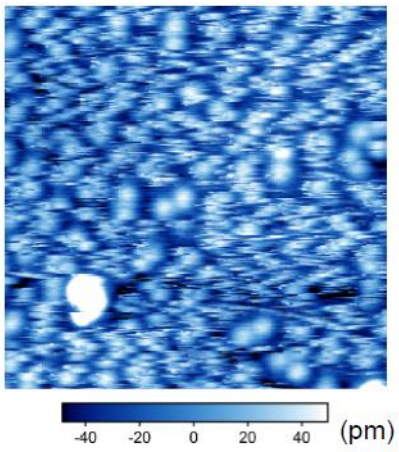

Figure 15. Noisy features observed in STM images of $Li_{0.66}CoO_2(001)$ surface obtained at ~5 K. The noisy features are probably due to unstable Li on the surface. Reprinted figure in the supplemental material with permission from Ref. 21. Copyright 2013 by the American Physical Society.

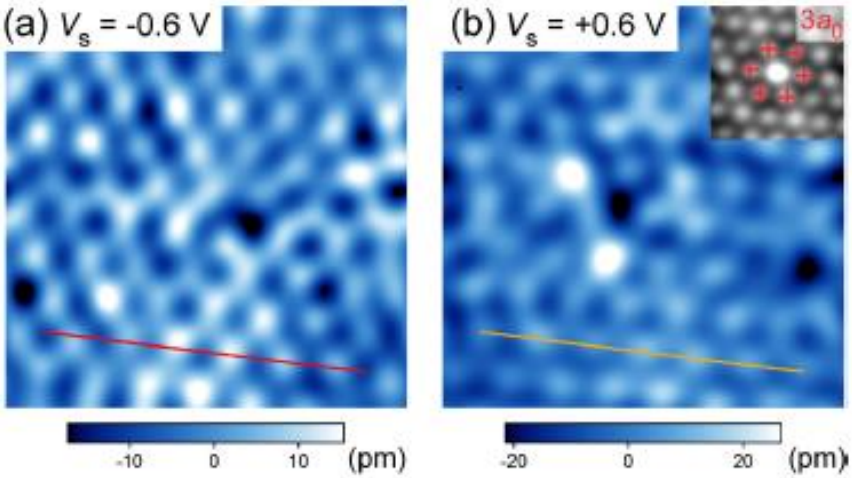

Figure 16. STM images of CoO_2 layer on $Li_{0.66}CoO_2(001)$ surface, (a) and (b) V_s = -0.6 and +0.6 V, respectively (6×6 nm^2, It= 0.3 nA). The autocorrelation image of (b) is shown in the inset. Reprinted figure with permission from Ref. 21. Copyright 2013 by the American Physical Society.

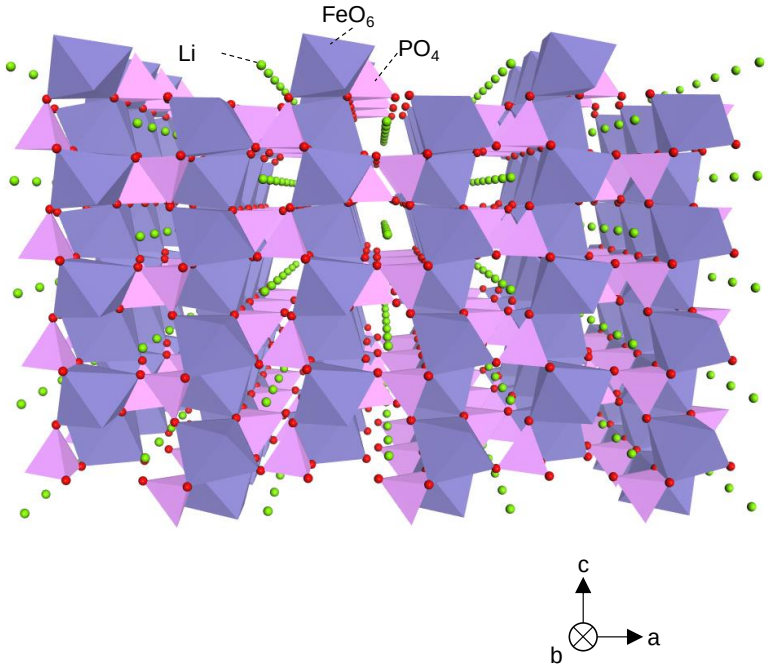

Figure 17. Crystal structure of olivine type $LiFePO_4$. Green and red balls show Li and O, respectively. Dark purple octahedrons and pink tetrahedrons show FeO_6 and PO_4 units, respectively.

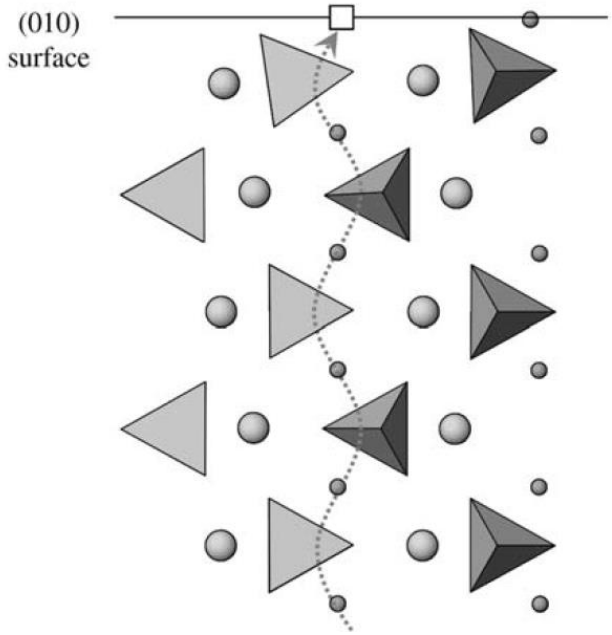

Figure 18. Li migration pathway directed to (010) in $LiFePO_4$ crystal. Small and large spheres show the Li and Fe ions. The tetrahedral structures show PO_4 units. Reproduced from Ref. 102 with permission of The Royal Society of Chemistry.

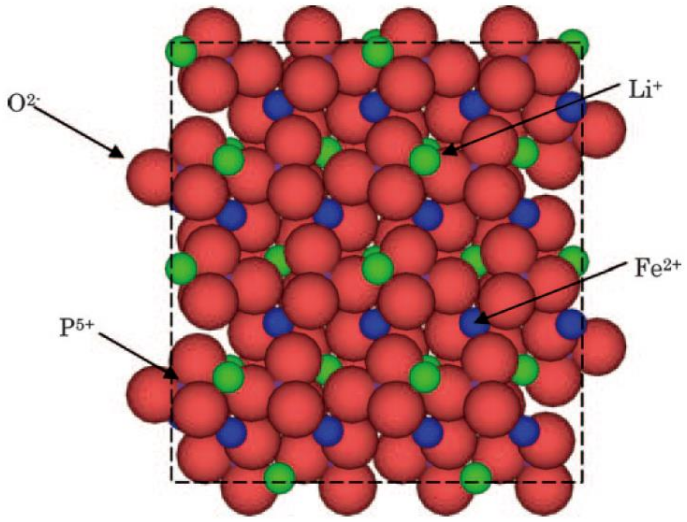

Figure 19. Surface structure of $LiFePO_4$(010) determined by calculation used a classical force field model (empirical potential model). Green, blue, purple and red balls show Li, Fe, P and O ions. Reproduced from Ref. 102 with permission of The Royal Society of Chemistry.

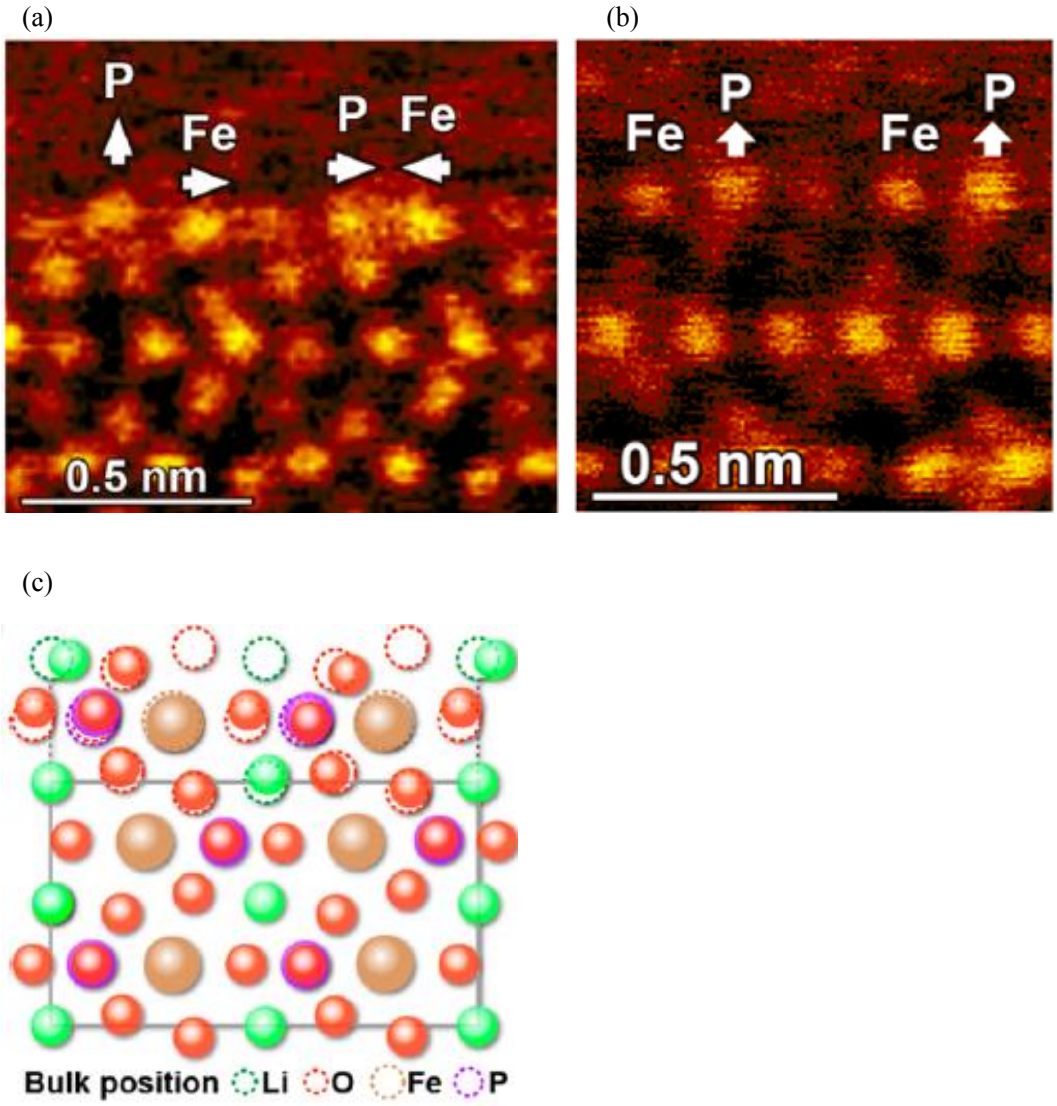

Figure 20. A image obtained by annular bright field (ABF) imaging in aberration-corrected scanning transmission electron microscopy (STEM) of the $LiFePO_4$(010) surface taken down the [001] zone axis, (a) cleavage surface and (b) the surface after 3000 h from chemical deithiation. The white arrows in (a) and (c) indicate the directions of shift of P and Fe atom columns from the bulk position. (b) Cross-section of the reconstructed (010) surface model of $LiFePO_4$ obtained from first-principles calculations. Reprinted with permission from Ref. 23. Copyright 2016 American Chemical Society.

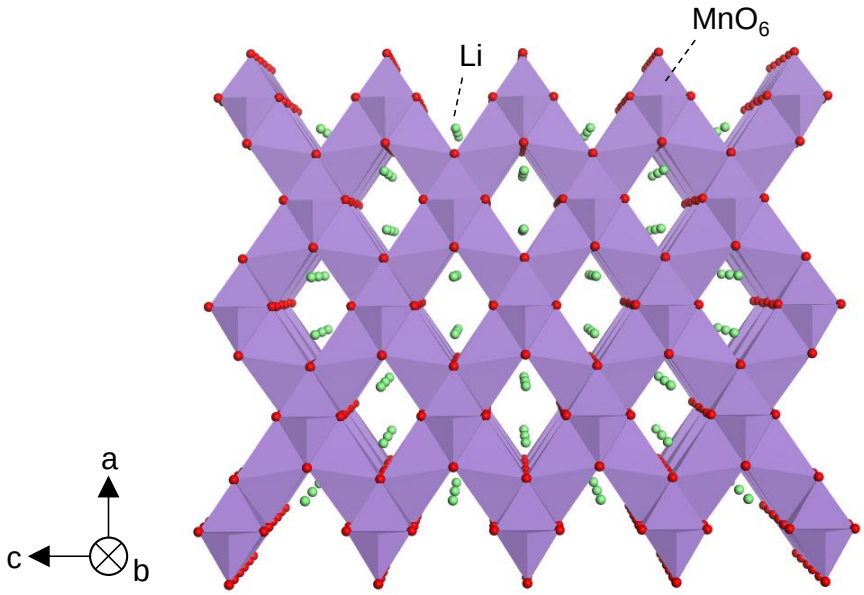

Figure 21. Crystal structure of spinel type $LiMn_2O_4$. Green and red balls show Li and O, respectively. Light purple octahedrons show MnO_6 units.

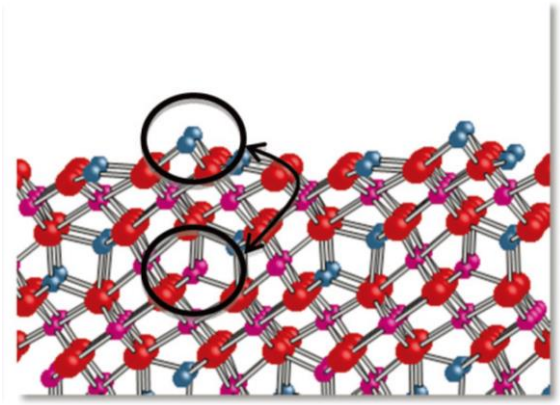

Figure 22. The surface structure of Li-terminated $LiMn_2O_4(111)$ with inverse spinel structure obtained by first principles calculations. Blue, magenta and red circles show Li, Mn and O atomic species, respectively. The reconstruction between the undercoordinated surface Mn and bulk fully tetrahedrally coordinated Li is indicated by the circles. Reprinted figure with permission from Ref. 108. Copyright 2013 by the American Physical Society.

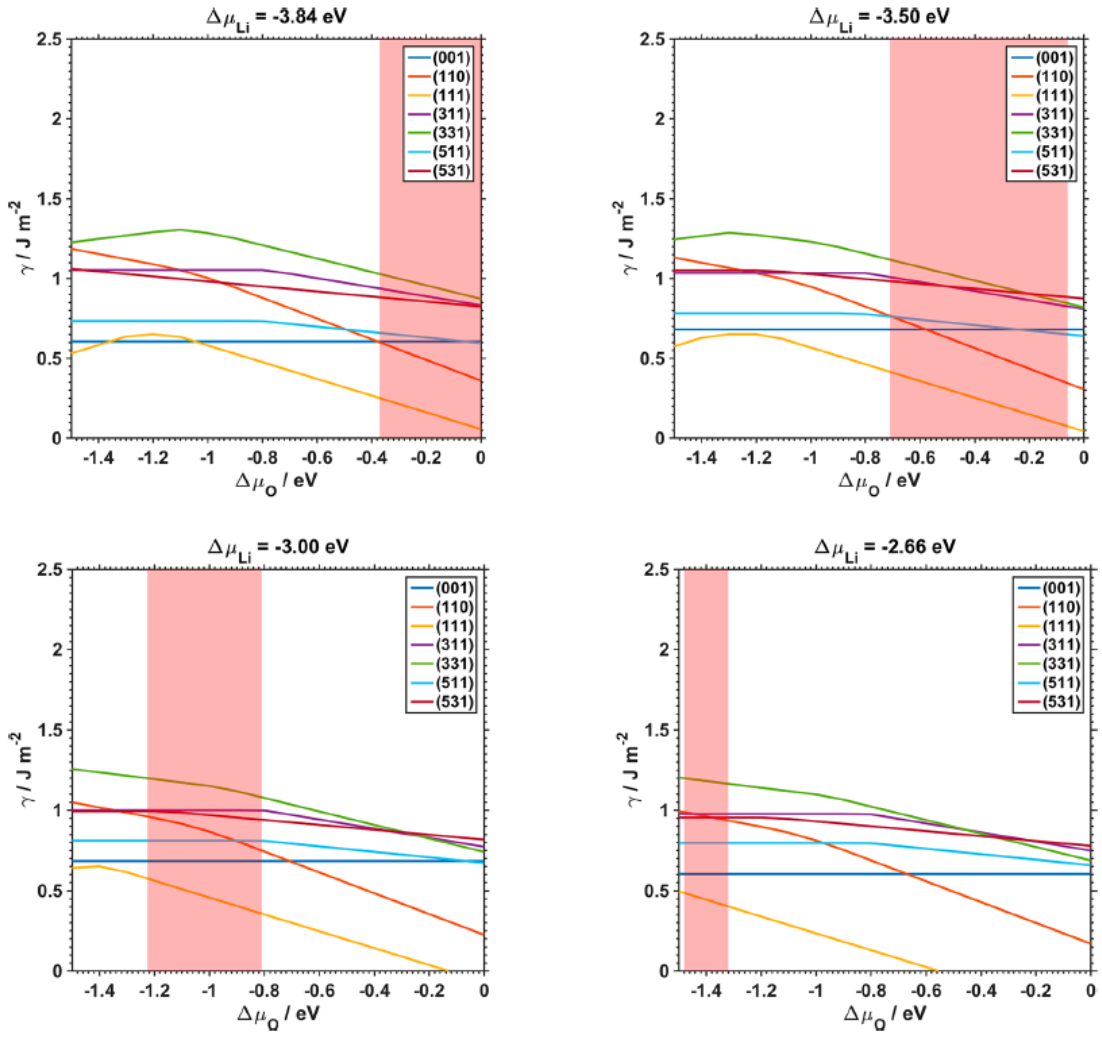

Figure 23. Surface energies of the most stable surface terminations for the low- and high-index surfaces of $LiMn_2O_4$. Each phase diagram is plotted for a fixed value of $\Delta\mu_{Li}$, whereas $\Delta\mu_O$ is considered as a variable parameter. Reprinted with permission from Ref. 115. Copyright 2016 American Chemical Society.

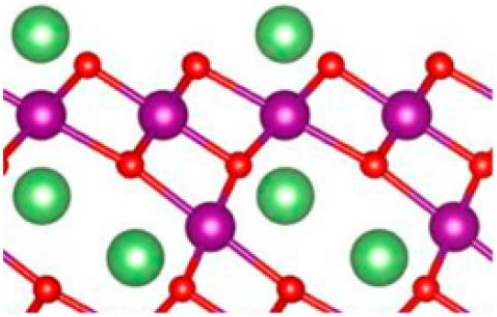

Figure 24. Li-terminated $LiMn_2O_4$(111) structure which is obtained by first principles calculation as the most stable structure. Reprinted with permission from Ref. 115. Copyright 2016 American Chemical Society.

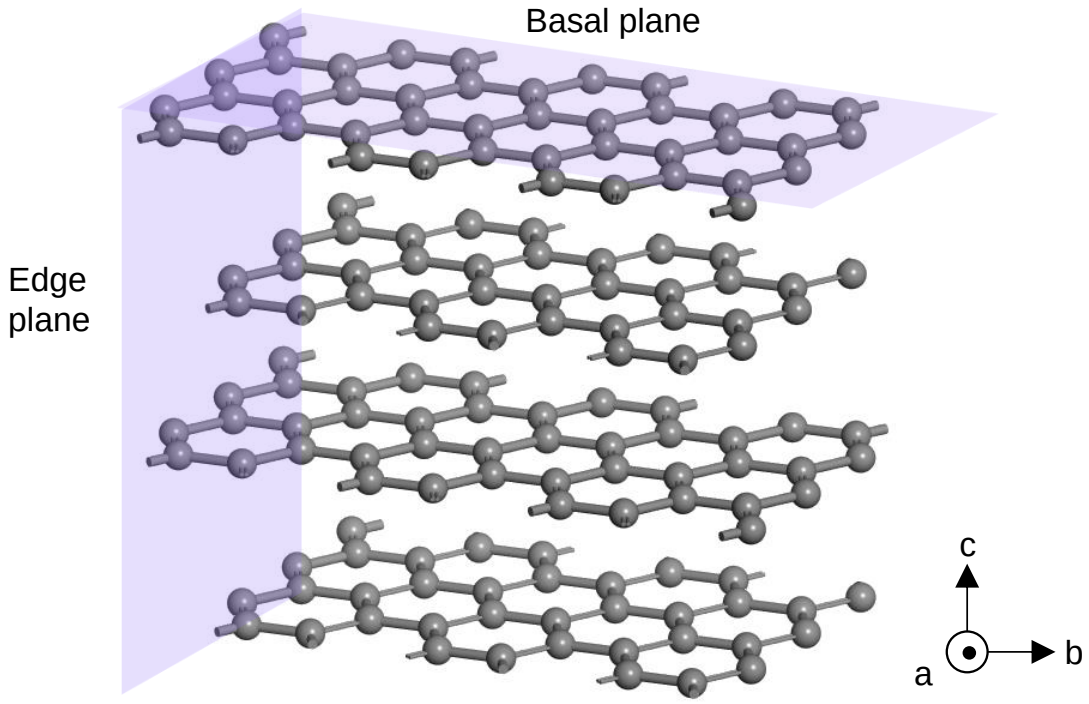

Figure 25. Crystal structure of graphite. Basal and edge planes are shown in the figure.

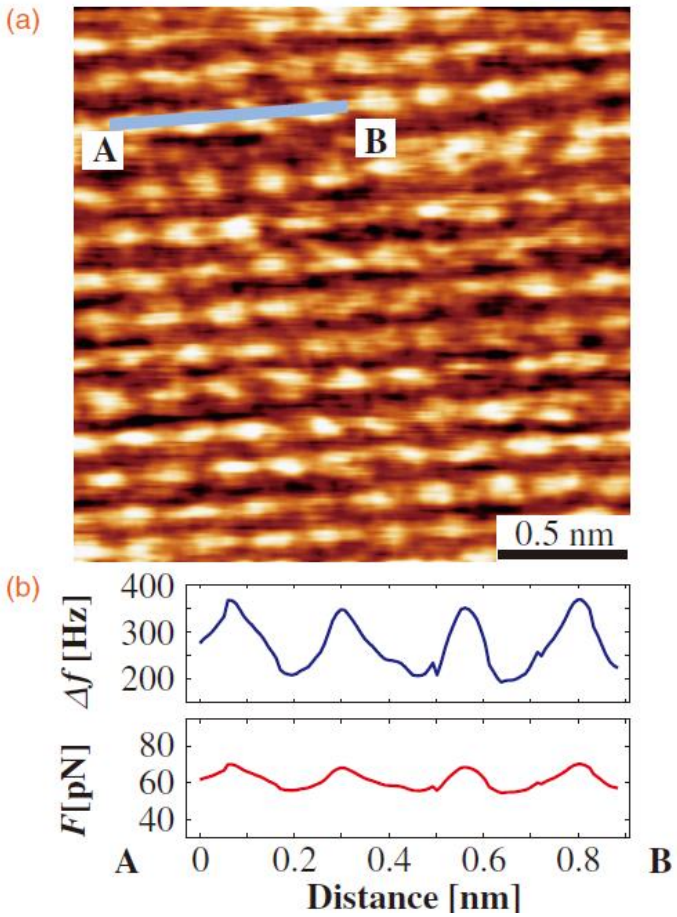

Figure 26. (a) Frequency modulation atomic force microscopic image of graphite(001) in water. The image was obtained in the constant height (variable frequency shift) mode. (b) Cross-sectional profile (upper curve) measured on A–B line in Fig. 26(a) and force profile (lower curve). Reprinted from Ref. 117 with permission. Copyright 2011 The Japan Society of Applied Physics

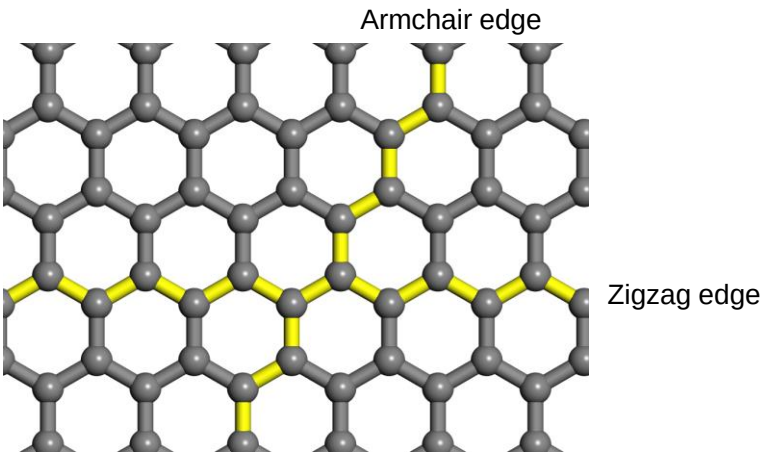

Figure 27. Structure of zigzag and armchair edges in a graphite layer (graphene).

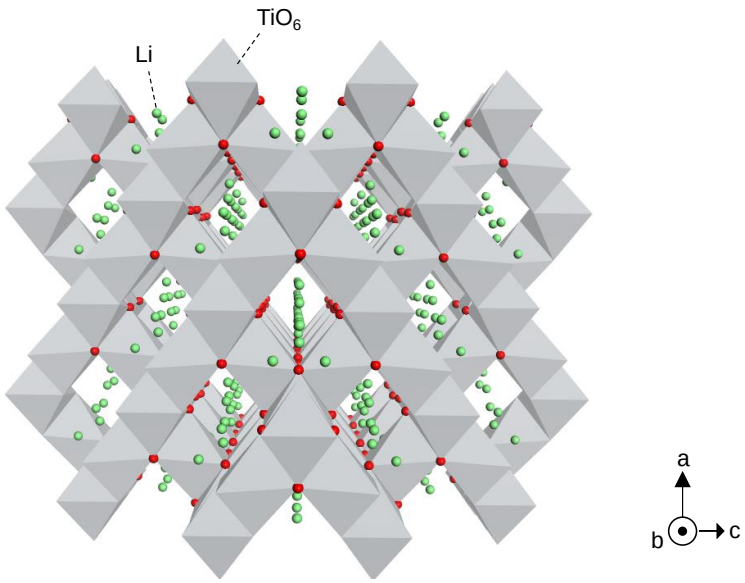

Figure 28. Crystal structure of $Li_4Ti_5O_{12}$. Green and red balls show Li and O, respectively. Gray octahedrons show TiO_6 units.

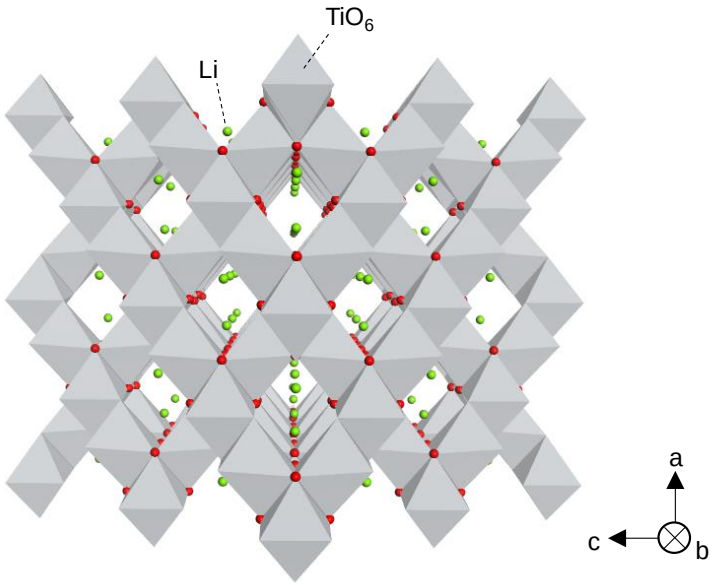

Figure 29. Crystal structure of $LiTi_2O_4$. Green and red balls show Li and O, respectively. Gray octahedrons show TiO_6 units.

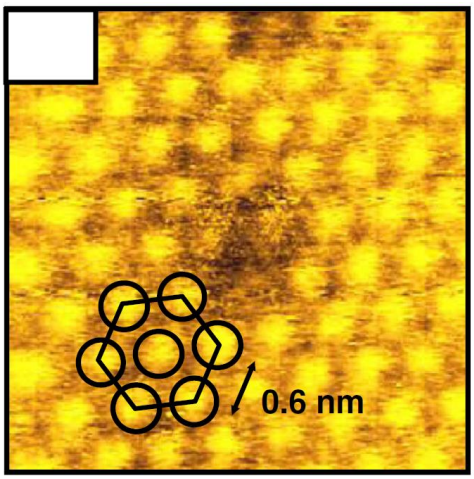

Figure 30. Atom resolved image of $Li_4Ti_5O_{12}(111)$ surface obtained by scanning tunneling microscopy in ultra-high vacuum. Reprinted from Ref. 122, Copyright 2014, with permission from Elsevier.

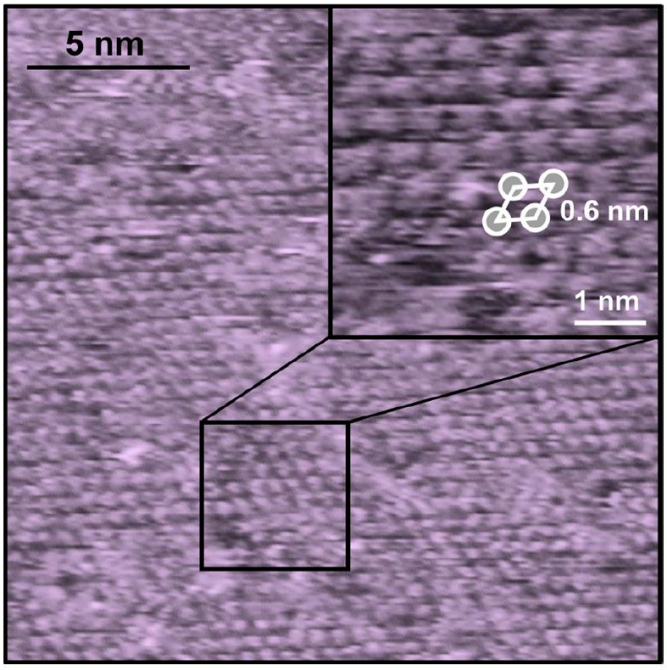

Figure 31. Atom resolved image of $Li_4Ti_5O_{12}$(111) surface obtained by frequency-modulation atomic force microscopy in aqueous solution. Reprinted from Ref. 123, with the permission of AIP Publishing.

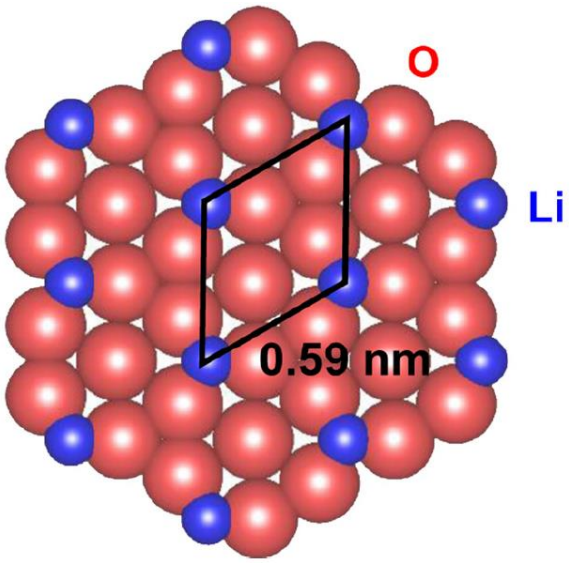

Figure 32. The proposed surface structure of $Li_4Ti_5O_{12}$(111) surface. Reprinted from Ref. 123, with the permission of AIP Publishing.

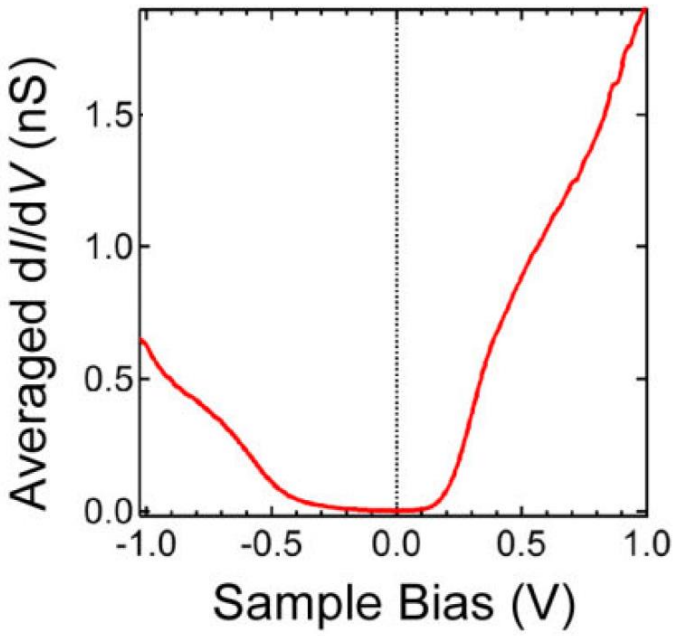

Figure 33. dI/dV spectrum of Li-$Li_{0.66}CoO_2$(001) obtained at ~5 K in ultra-high vacuum. The tip position was Vs = -0.8 V and I_t = 0.3 nA. Reprinted figure with permission from Ref. 21. Copyright 2013 by the American Physical Society.

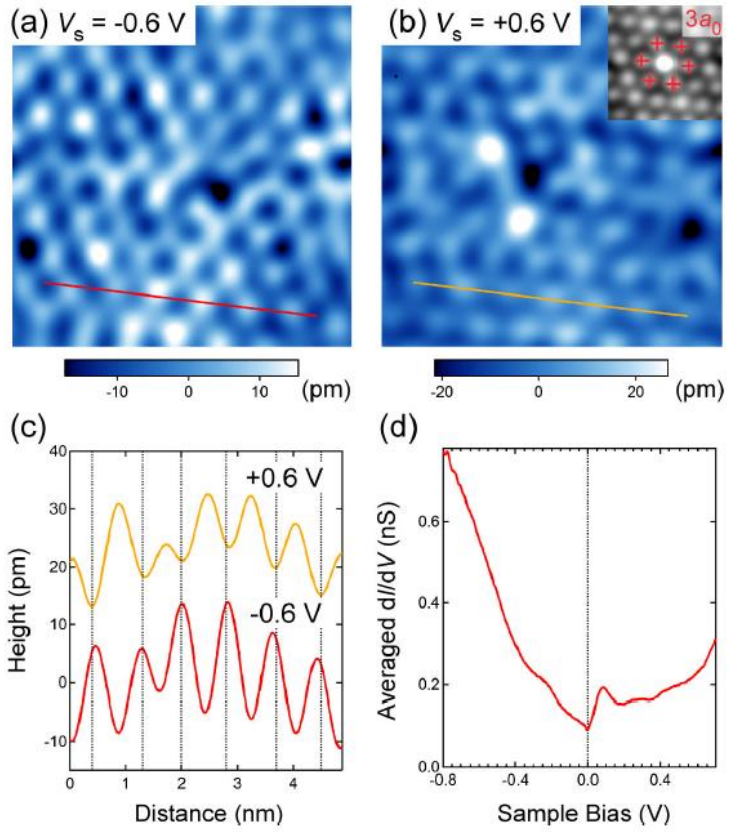

Figure 34. (a) and (b) ordering images obtained by scanning tunneling microscopy on CoO_2 layers on $Li_{0.66}CoO_2(001)$ at V_s = -0.6 and +0.6 V, respectively. 6×6 nm^2, It = 0.3 nA. The autocorrelation image of (b) is shown in the inset. (c) Comparison of line profile of the image at -0.6 and +0.6 V in (a) and (b). (d) Averaged d*I*/d*V* spectrum taken in (a). Set point: I_t = 0.3 nA, V_s = -0.8 V. Reprinted figure with permission from Ref. 21. Copyright 2013 by the American Physical Society.

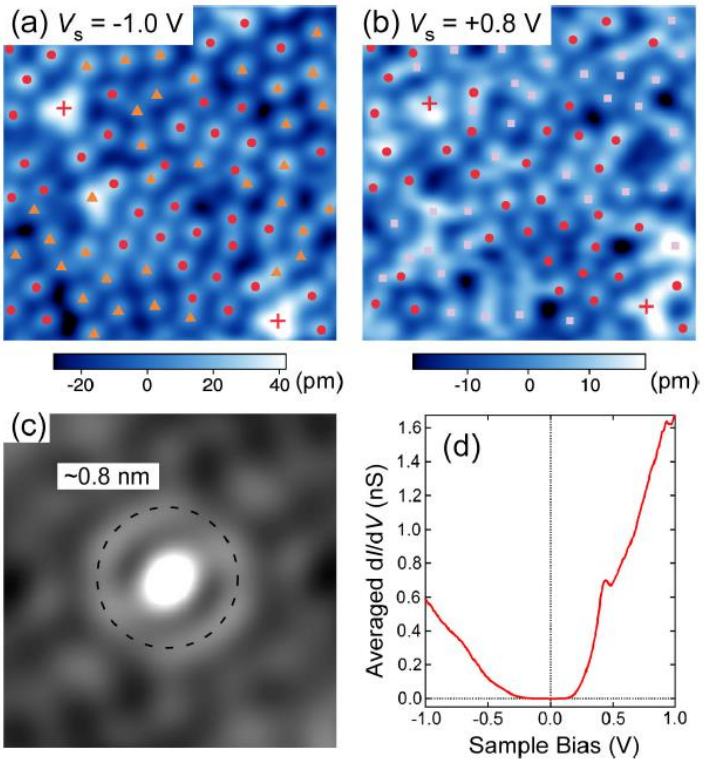

Figure 35. (a) and (b) disordering images obtained by scanning tunneling microscopy on CoO2 layers of $Li_{0.66}CoO_2(001)$ at V_s = -1.0 and +0.8 V, respectively. Both images were taken at the same position; 7×7 nm^2, I_t = 0.3 nA. (c) Autocorrelation image of (a). (d) Averaged dI/dV spectrum taken in (a). Set point: I_t = 0.2 nA, V_s = -1.0 V. Reprinted figure with permission from Ref. 21. Copyright 2013 by the American Physical Society.

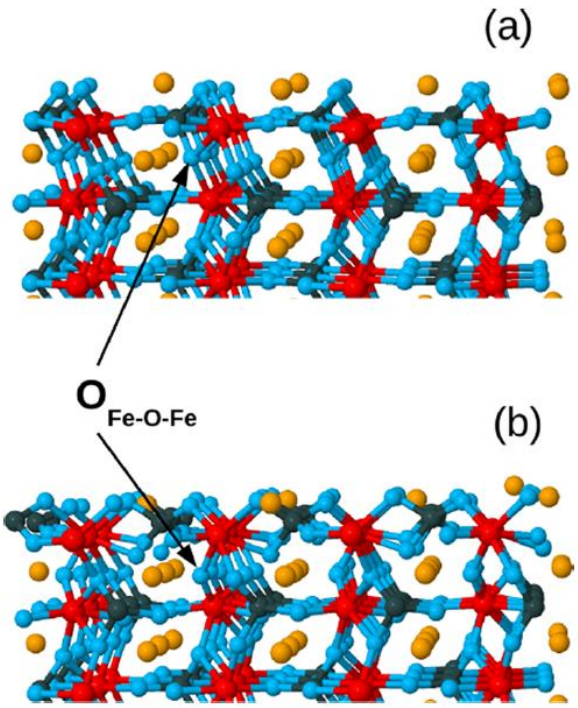

Figure 36. Surface structure of $LiFePO_4(010)$ and oxygenated $LiFePO_4(010)$ obtained by first principles calculation. Reprinted with permission from Ref. 131. Copyright 2015 American Chemical Society.

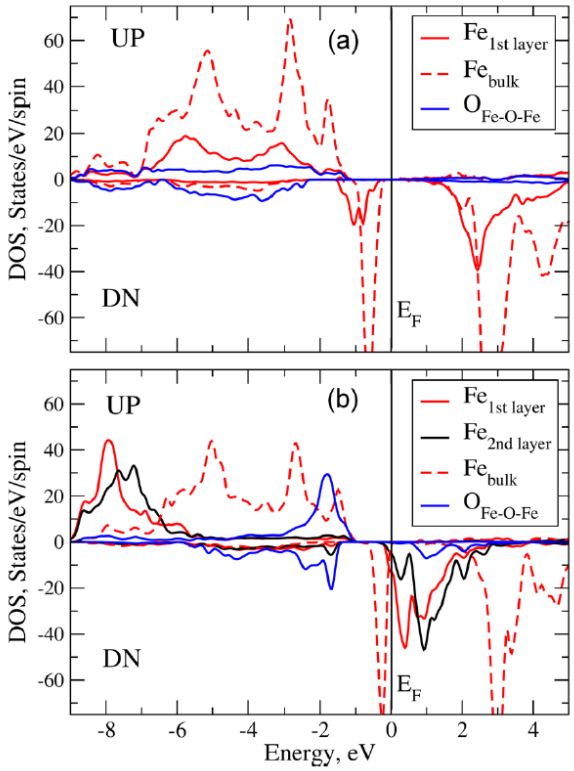

Figure 37. Projected density of electronic states of the clean (a) and oxygenated (b) $LiFePO_4$(010) surfaces. The contribution of top two Fe layers, as well as O atoms between them, is shown. Reprinted with permission from Ref. 131. Copyright 2015 American Chemical Society.

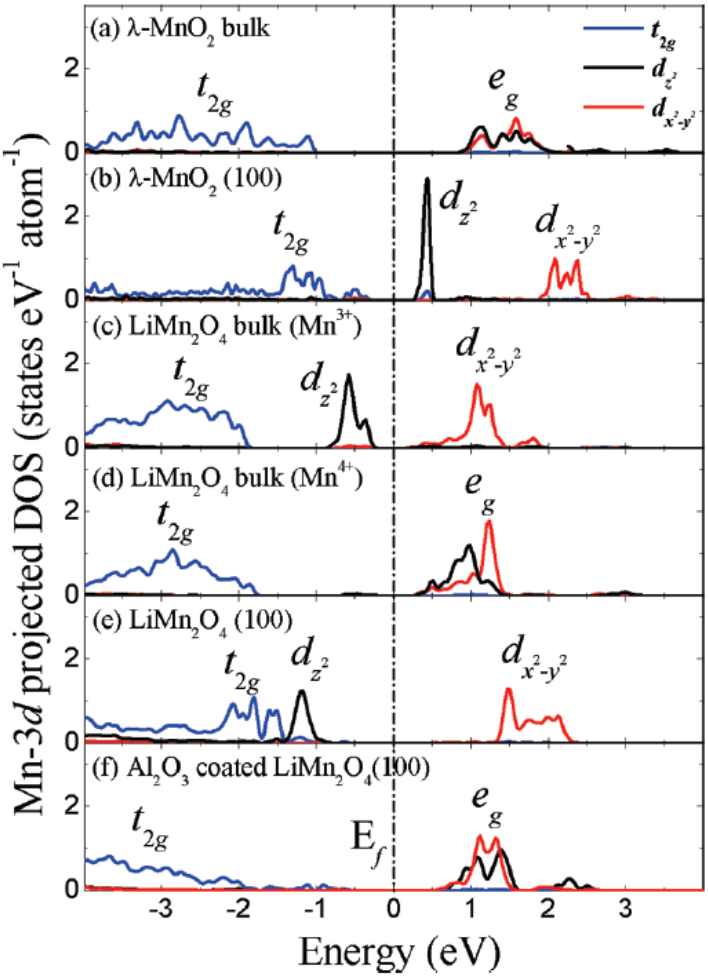

Figure 38. Mn-3d projected density of states of (a) bulk λ-MnO_2, (b) the λ-MnO_2(001) surface, (c) Mn^{3+} in bulk $LiMn_2O_4$, (d) Mn^{4+} in bulk $LiMn_2O_4$, (e) the Li-terminated $LiMn_2O_4$(001) surface, and (f) the Al_2O_3/$LiMn_2O_4$ (001) surface. Reprinted with permission from Ref. 133. Copyright 2010 American Chemical Society.

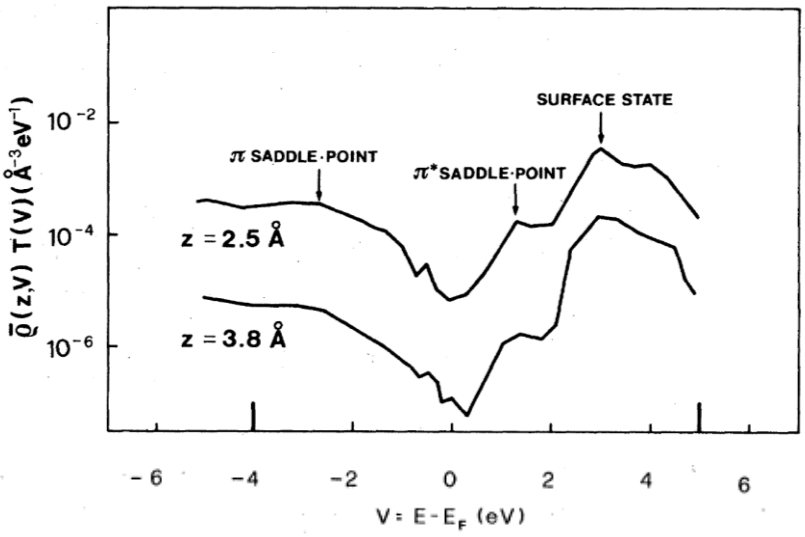

Figure 39. Scanning tunneling spectroscopy obtained on basal plane of graphite surface. Reprinted figure with permission from Ref. 139. Copyright 1985 by the American Physical Society.

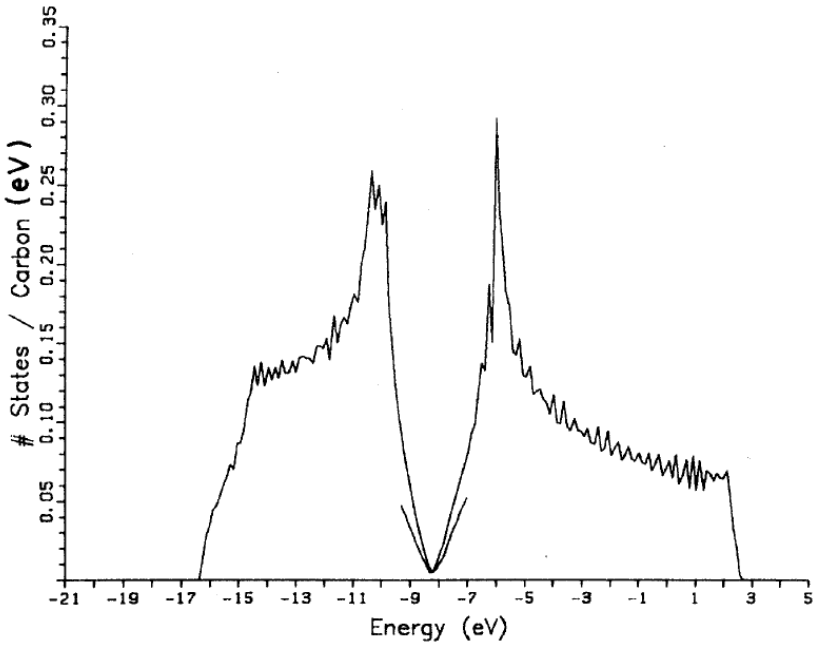

Figure 40. Density of state of graphite calculated by using the full zone π-band Johnson-Dresselhaus model. Reprinted figure with permission from Ref. 142. Copyright 1982 by the American Physical Society.

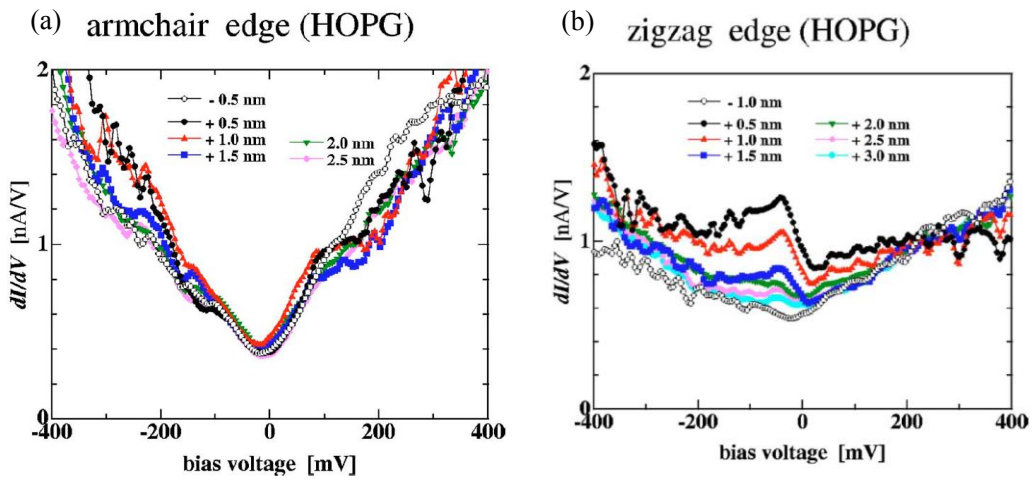

Figure 41. d*I*/d*V* curves obtained armchair (a) and zigzag (b) edges on HOPG. Reprinted figure with permission from Ref. 144. Copyright 2006 by the American Physical Society.

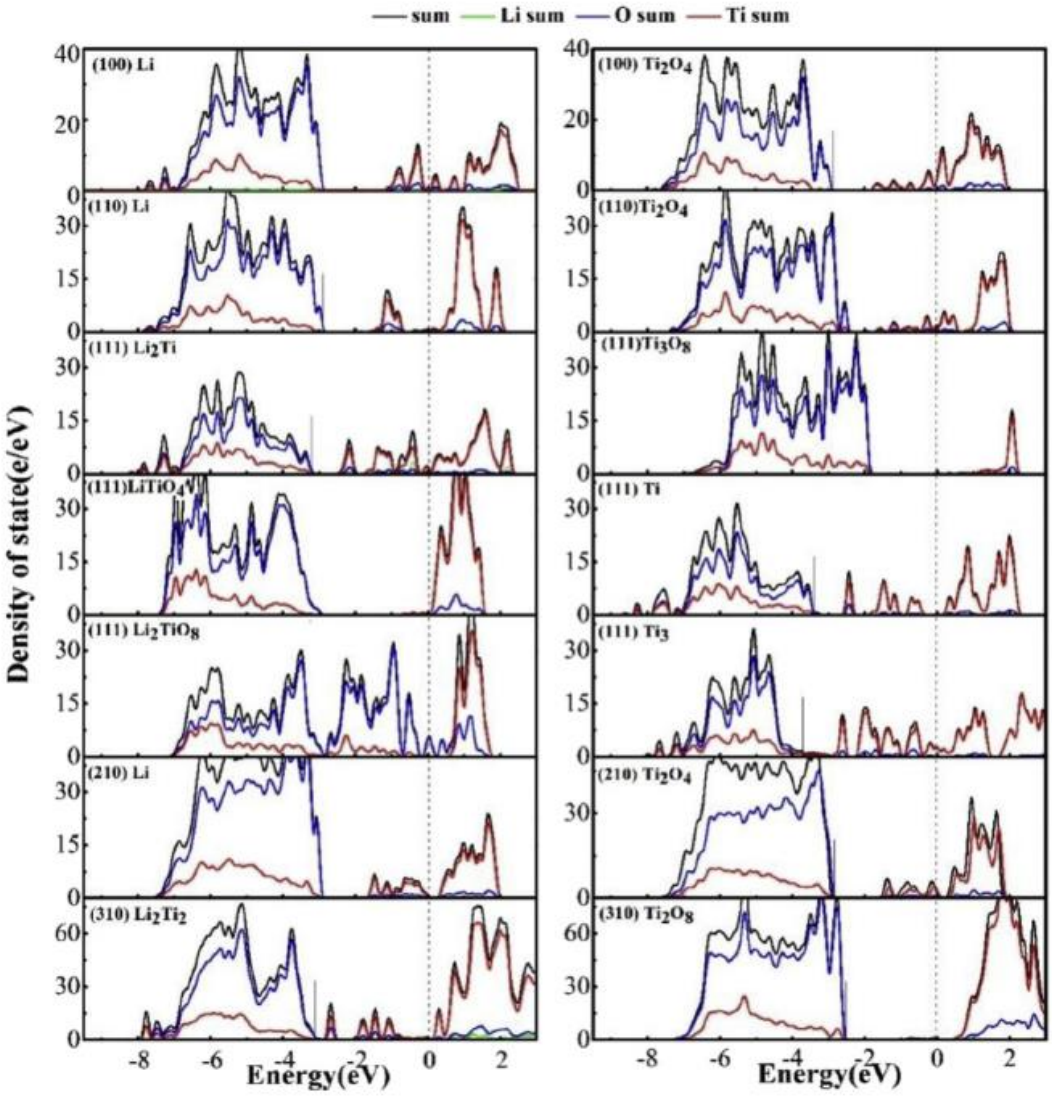

Figure 42. Density of states of surfaces of $Li_4Ti_5O_{12}$ calculated by first principles calculation. Reprinted from Ref. 126, 2016, with permission from Elsevier.

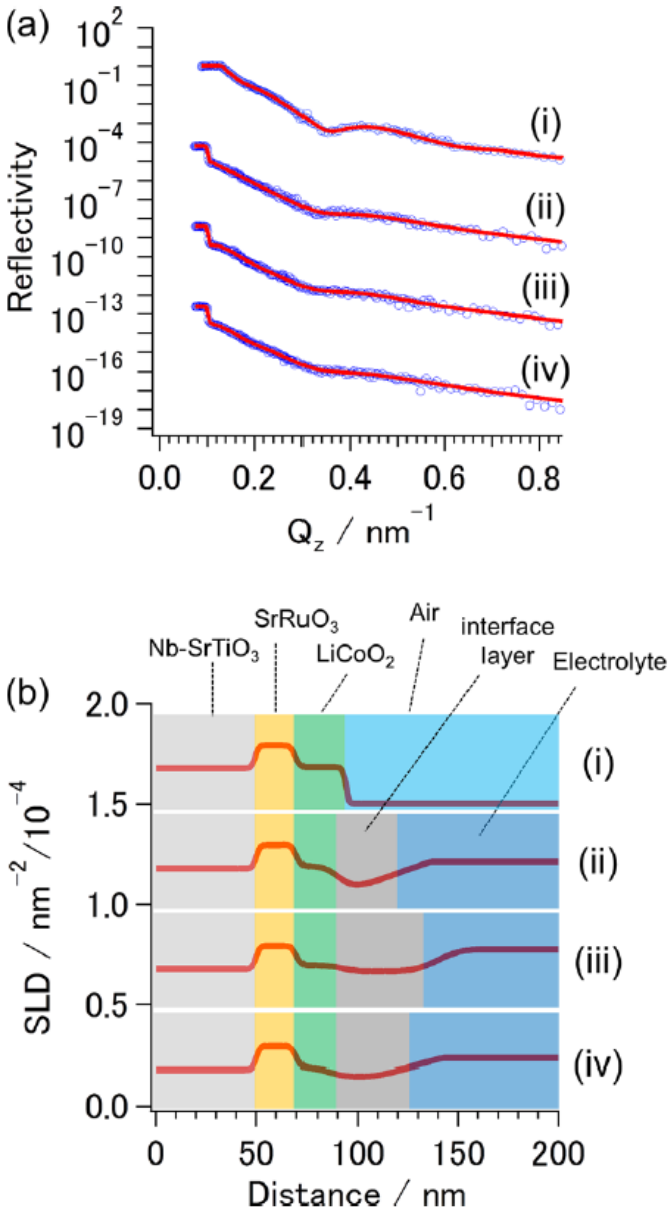

Figure 43. (a) Neutron reflectivity and (b) analyzed scattaring length density determined for (i) as-prepared sample, (ii) sample after immersion in electrolyte (1 M $LiClO_4$ in deuterated EC:DMC (vol. 1:2)), (iii) sample after Li extraction at 4.2 V (vs Li^+/Li), and (iv) sample after Li^+ insertion at 3.3 V (vs Li+/Li) of $LiCoO_2$(104) layer/$SrRuO_3$(100) layer/Nb−$SrTiO_3$(100) layer. The blue dots and red curves in (a) correspond to experimental and fitted data, respectively. The neutron reflectivity in (ii),

(iii), and (iv) and SLD values in (i), (ii), and (iii) are shifted for offsets. Reprinted with permission from Ref. 16. Copyright 2016 American Chemical Society.

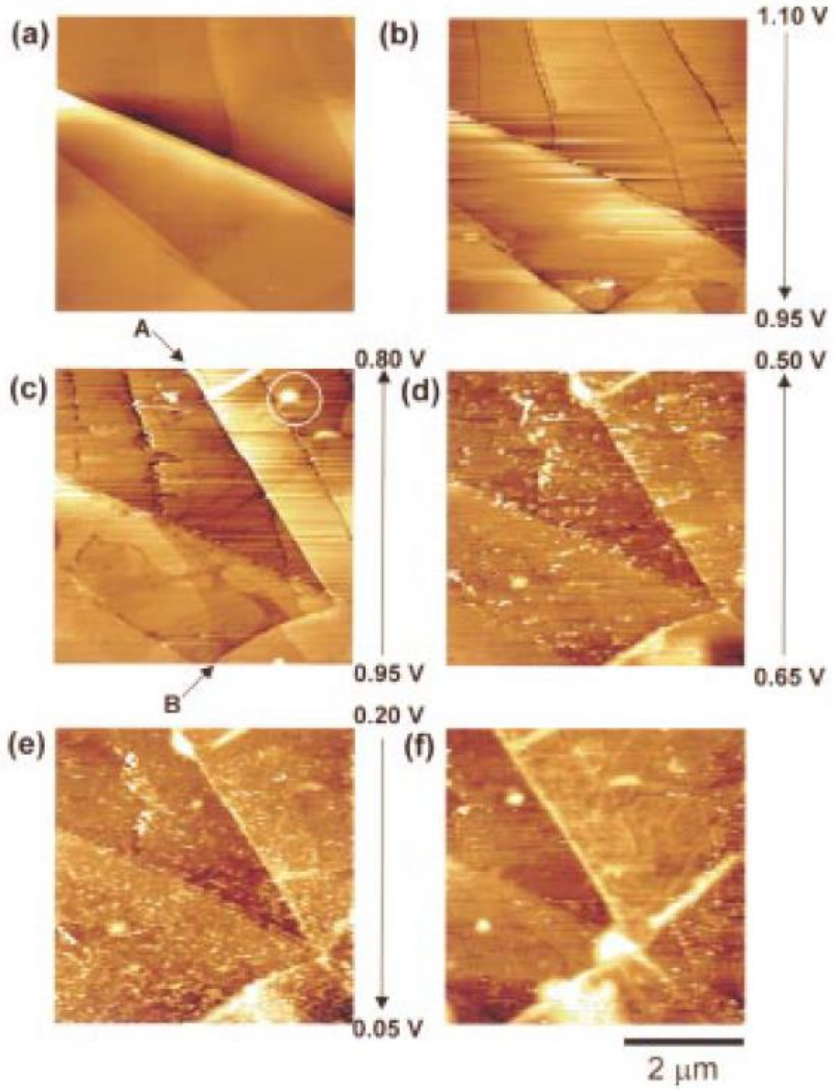

Figure 44. *in-situ* atomic force microscopy images obained on the basal plane of HOPG (a) 2.9 V (vs. Li/Li^+) before starting potential scan, (b) 1.10 - 0.95 V (vs. Li/Li^+), (c) 0.95 - 0.80 V (vs. Li/Li^+), (d) 0.65 - 0.50 V (vs. Li/Li^+), (e) 0.20 - 0.05 V (vs. Li/Li^+) during the first cycle at 0.5 mV s^{-1}, and (f) 2.9 after the first cycle in 1 M $LiClO_4$ /EC + DEC (vol. 1 : 1). Reprinted with permission from Ref. 20. 2001, The Electrochemical Society.

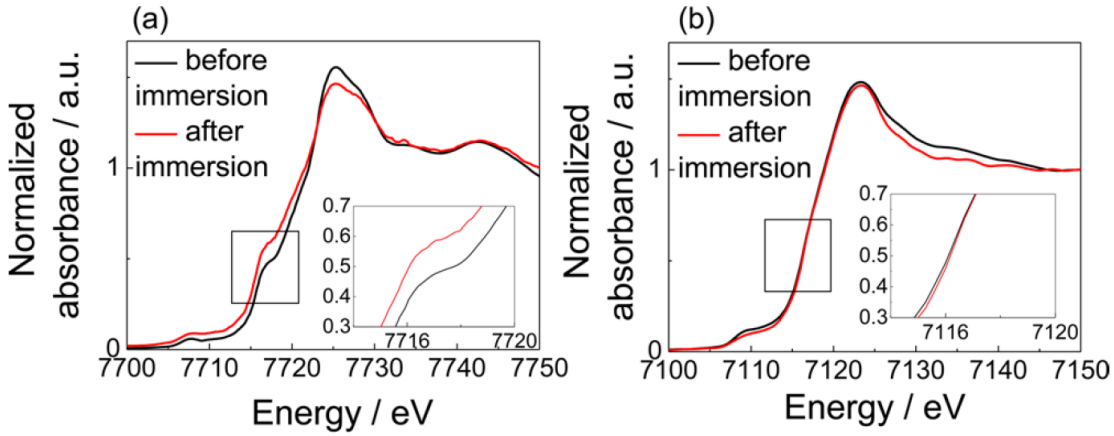

Figure 45. (a) Co *K*-edge XANES spectra on $LiCoO_2$ surface and (b) Fe *K*-edge XANES spectra on $LiFePO_4$ surface before (black line) and after (red line) electrolyte immersion, obtained via *in situ* total reflection fluorescence-X-ray absorption spectroscopy. Reprinted with permission from Ref. 13. Copyright 2014 American Chemical Society.

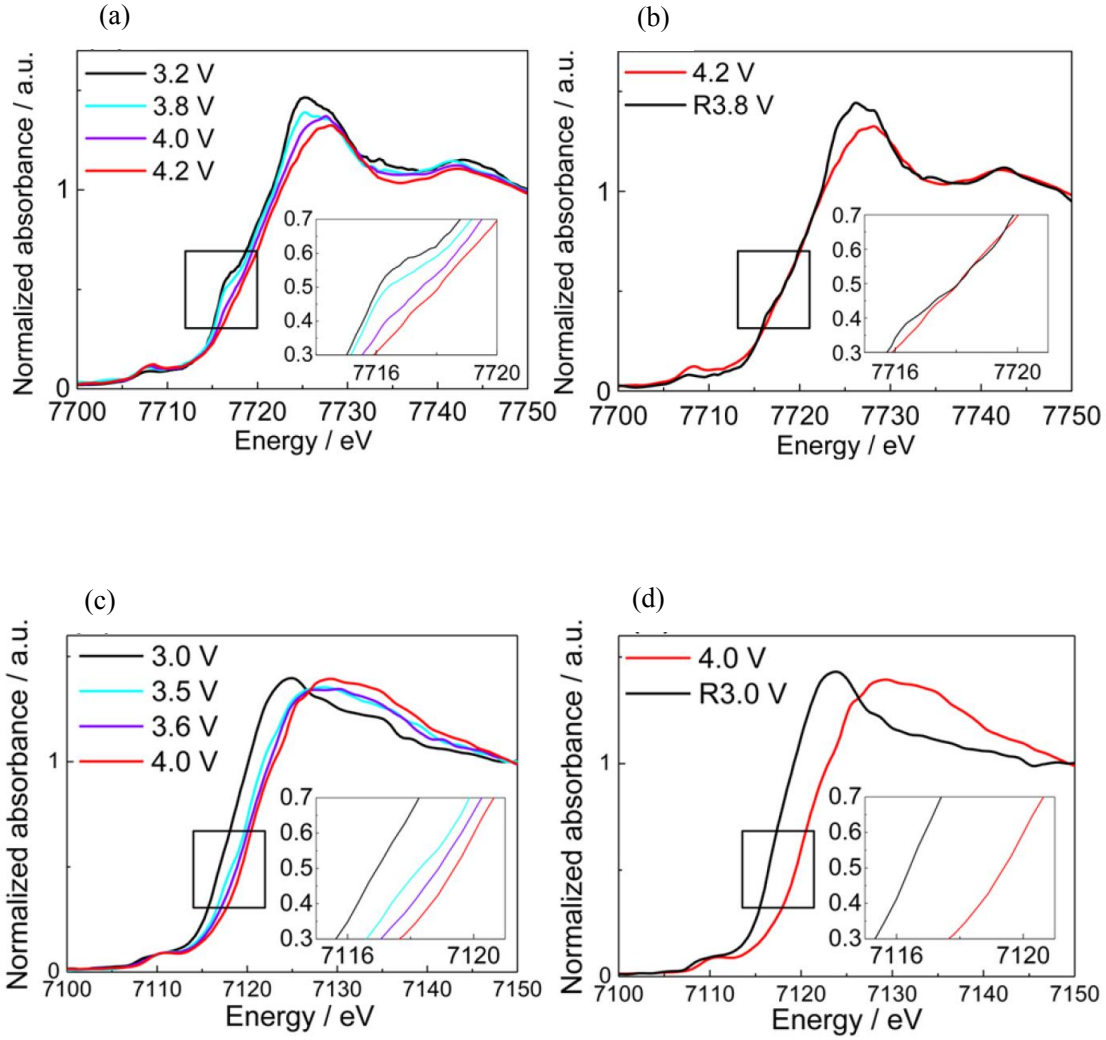

Figure 46. Co *K*-edge XANES spectra of the $LiCoO_2$ surface during (a) Li ion extraction and (b) insertion (R3.8 V is the voltage applied during Li-ion insertion). Fe *K*-edge XANES spectra on $LiFePO_4$ surface during (c) Li ion extraction and (d) insertion (R3.0 V is the voltage applied during Li-ion insertion). Reprinted with permission from Ref. 13. Copyright 2014 American Chemical Society.

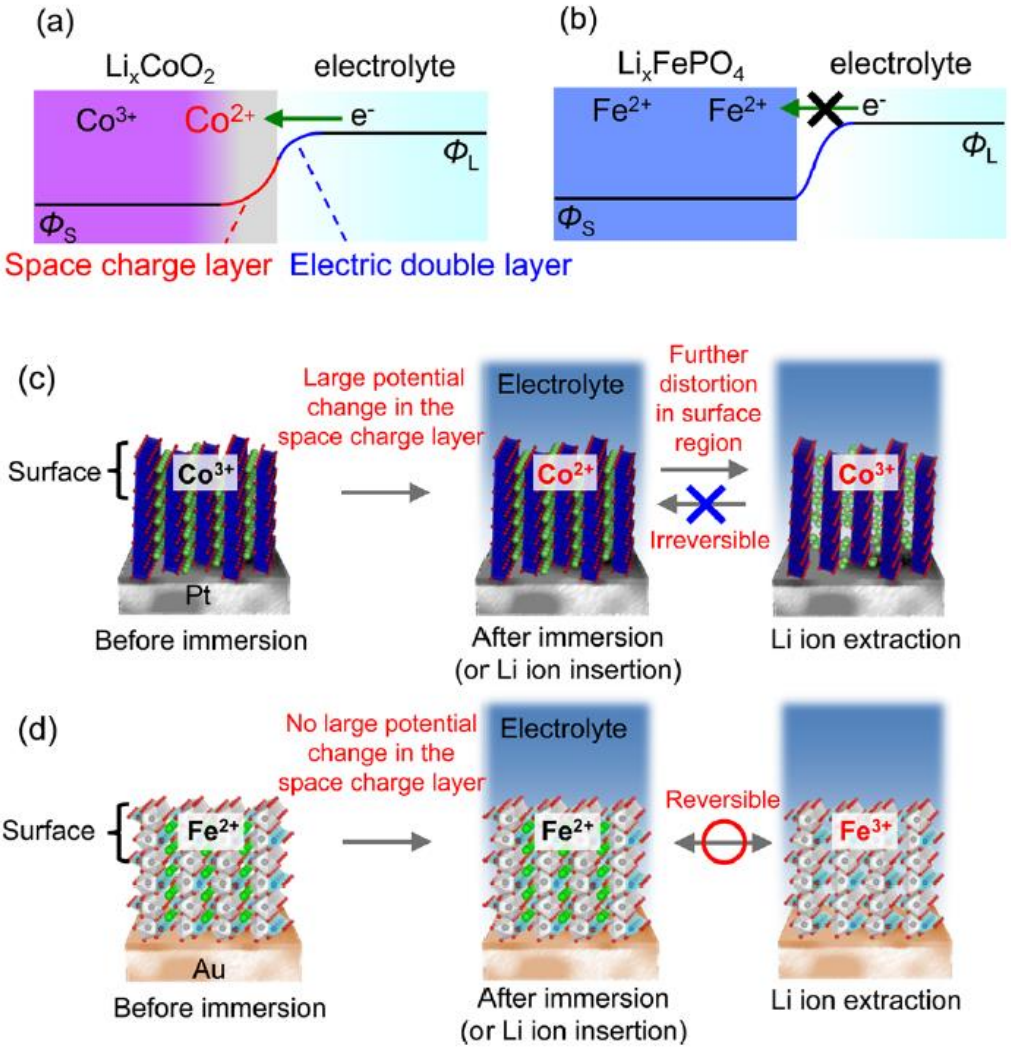

Figure 47. Schematic illustrations of the changes in the electronic structure at the (a,c) $LiCoO_2$/electrolyte and (b,d) $LiFePO_4$/electrolyte interfaces upon electrolyte immersion and during Li ion extraction/insertion. (Φ_S and Φ_L are the inner potentials of the electrode and electrolyte, respectively. Reprinted with permission from Ref. 13. Copyright 2014 American Chemical Society.

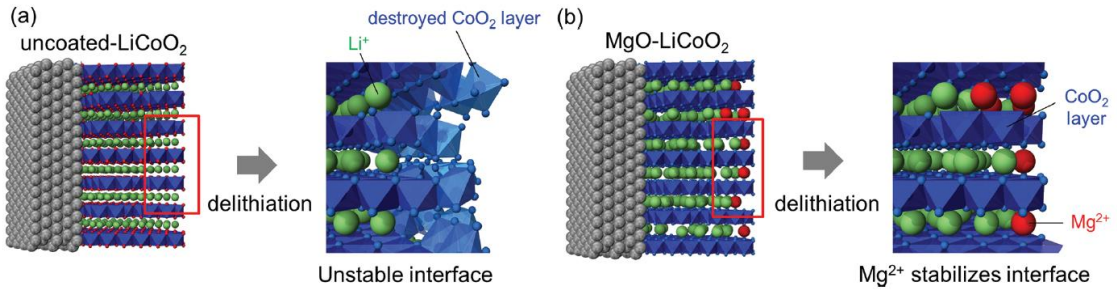

Figure 48. Schematic view of the surface structure of (a) $LiCoO_2$ and (b) MgO coated $LiCoO_2$ during lithium ion extraction. Reprinted from Ref. 81 with permission from the Wiley publication.

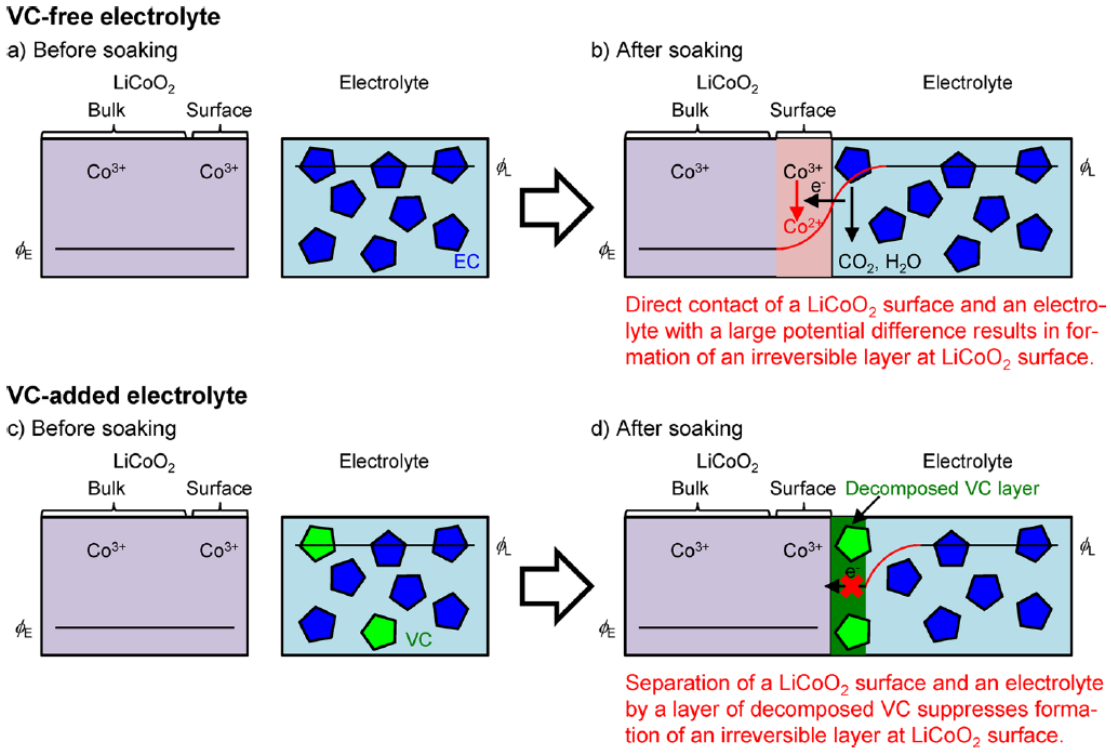

Figure 49. Schematic illustration of the electronic structure at the $LiCoO_2$/electrolyte interface for (a, b) the VC-free and (c, d) the VC-added electrolytes. ϕ_E and ϕ_L are electrochemical potentials of an electron in the electrode and the electrolyte, respectively. The blue and green pentagons represent EC and VC molecules, respectively. Reprinted with permission from Ref. 82. Copyright 2015 American Chemical Society.

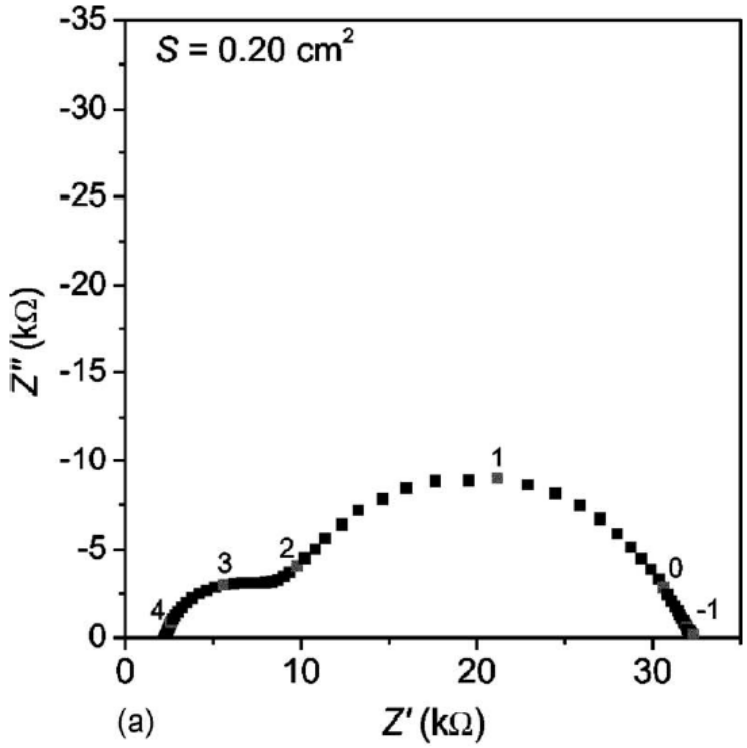

Figure 50. A example of Nyquist plot for a four-probe system consisting of Li/electrolyte/LLT/electrolyte/Li. The electrolyte was 1 M $LiCF_3SO_4$ in PC. Reprinted with permission from Ref. 10. 2005, The Electrochemical Society.

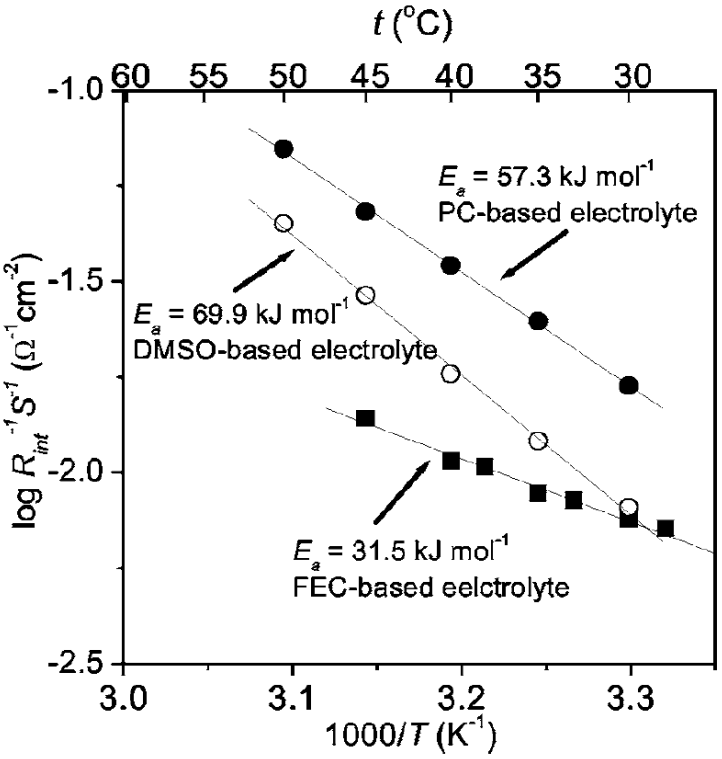

Figure 51. Temperature dependencies of Li ion transfer resistances at the interface between glass electrolyte and liquid electrolytes of PC, DMSO, and FEC containing 1 M $LiCF_3SO_3$. Reprinted with permission from Ref. 10. 2005, The Electrochemical Society.

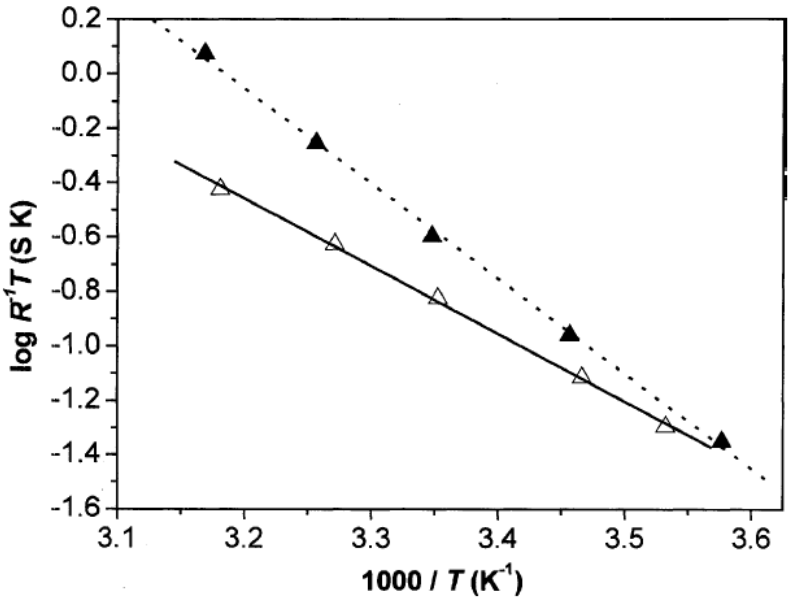

Figure 52. Temperature dependence of Li ion transfer through Li_xCoO_2/PC interface. Closed and open circles show the data obtained from bare and an MgO coated $LiCoO_2$ thin film electrodes at 4.0 V (vs. Li/Li^+). Reprinted from Ref. 183, 2004, with permission from Elsevier.

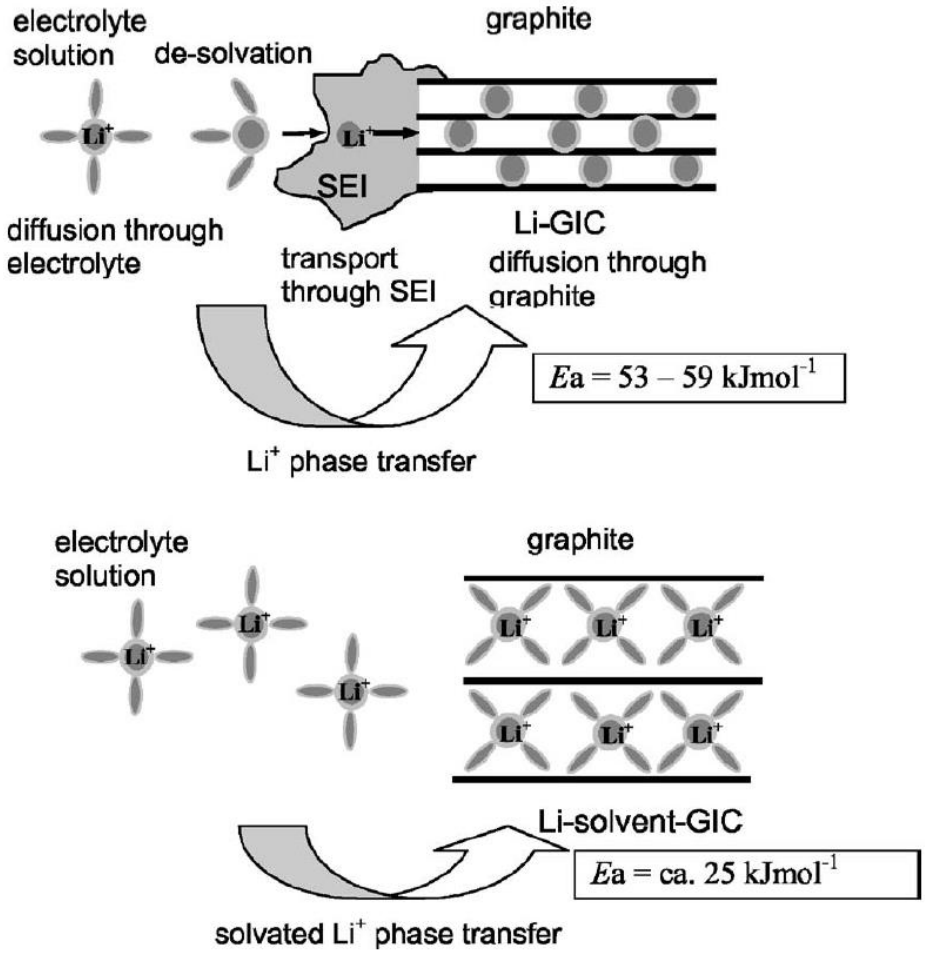

Figure 53. Schematic illustration of Li ion and solvated Li transfers at graphite electrodes. The activation energies for solvated Li ion transfer are much lower than those for Li ion transfer. Reprinted with permission from Ref. 10. 2005, The Electrochemical Society.

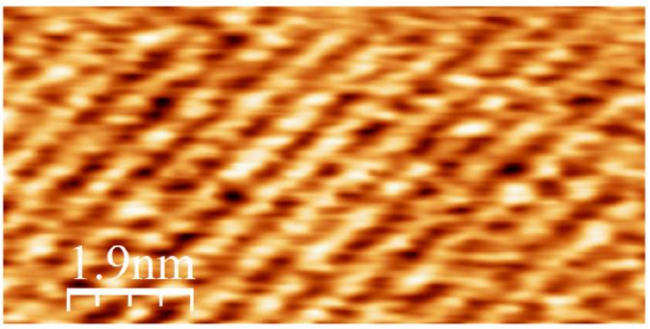

Figure 54. Observation of the first layer of adsorbed tetraglyme on HOPG obtained by frequency modulation atomic force microscopy in liquid. The frequency and amplitude of the cantilever oscillation are 92 kHz and 0.3 nm, respectively. Reprinted from Ref. 188, with the permission of AIP Publishing.

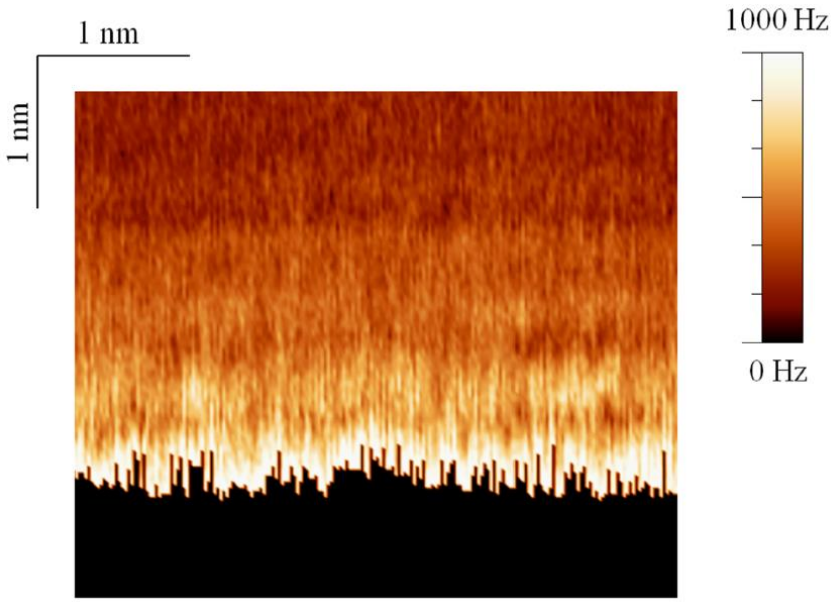

Figure 55. Cross-sectional distribution of frequency shift that reflect the molecular density in liquid phase at the tetraglyme/HOPG interface. The amplitude of the cantilever oscillation is 0.3 nm. The cantilever approached the surface until the frequency shift reached 1000 Hz. Reprinted from Ref. 188, with the permission of AIP Publishing.

Table 1. Physical parameters of $LiFePO_4$ surfaces calculated by classical force field model (empirical potential model). All data are from Ref. 102.

Plane	Tasker surface type	*d*-spacing, d_{nkl}/Å	Surface energy, $E_{surface}$/J m^{-2}		Attachment energy, E_{attach}/J m^{-2}
			Unrelaxed	Relaxed	
(001)	III	2.33	2.40	1.11	-11.18
(010)	III	3.01	1.64	0.72	-5.74
(100)	III	5.19	2.12	0.87	-3.39
(011)	III	3.69	2.55	0.75	-6.43
(012)	II	1.09	4.50	1.02	-27.31
(021)	II	1.27	2.41	0.82	-18.03
(101)	III	4.26	1.65	0.88	-3.42
(102)	II	2.28	3.29	1.15	-19.85
(110)	II	2.60	3.62	0.92	-16.25
(111)	III	3.48	2.94	0.89	-5.34
(112)	III	2.13	2.57	0.88	-16.81
(120)	III	1.45	3.53	0.86	-17.43
(121)	II	2.46	2.44	0.94	-11.27
(122)	III	1.82	2.65	0.80	-14.17
(201)	III	3.47	1.37	0.71	-4.27
(210)	III	3.93	2.61	0.90	-5.55
(211)	III	3.01	2.51	0.80	-8.60
(212)	III	2.01	2.26	0.86	-11.60
(221)	II	2.27	2.52	0.79	-10.69